University of Bialystok
Faculty of Physics

Ultrafast coherent photo-magnetic switching in ferrimagnetic garnets

Tomasz Zalewski

Supervisor:
Prof. dr hab. Andrzej Stupakiewicz

Bialystok 2023

ABSTRACT

Ultrafast magnetism is an intensively evolving and highly relevant field of physics that focuses on understanding the mechanisms of interaction between ultrashort laser pulses and matter. Ability to manipulate magnetization solely using laser pulses holds tremendous potential for future technologies, facilitating the fastest data recording with minimal heat dissipation. The main objective of this thesis is to understand the coherent dynamics of nonthermal photo-magnetic switching by controlling the magnetic anisotropy in cobalt-doped garnet films across a wide temperature range. These investigations were conducted using a newly designed, prepared, and optimized experimental setup that employs a unique single-shot time-resolved imaging method to capture magneto-optical dynamics during precession and magnetization switching.

Taking full advantage of this experimental setup, a comprehensive examination of various coherent photo-magnetic switching scenarios was performed, considering a single-domain or multi-domain and single bubble-domain switching. A detailed analysis of the switching trajectories between multiple magnetic states revealed non-reciprocity in the dynamics of nonthermal magnetization switching. This non-reciprocity arises from the magnetocrystalline symmetry of garnets and the torque induced by a femtosecond laser pulse with orthogonal linear polarization directions. To explain the multi-state magnetization dynamics, a theoretical model was developed within the framework of the Landau-Lifshitz-Gilbert formalism, incorporating a tensor of photo-magnetic susceptibility.

Furthermore, this thesis reports, for the first time, the nonthermal, toggle-switching of magnetization. This effect is induced solely by the sequence of femtosecond laser pulses without changing their polarization direction. Previously, only a thermal demagnetization-based mechanism for toggle-switching was known to exist, and it was limited to metals. The new 'cold' toggle-switching was observed in garnet films with pure magnetocrystalline cubic symmetry over an exceptionally broad temperature range $\pm$ 100°C. The energy of toggle-switching can be adjusted by tuning the intensity of the laser pulse and magnetic anisotropy of garnets. However, the switching time and energy of heat load are found to be competing parameters. We demonstrated that by using a series of identical laser pulses and employing this newly discovered switching mechanism, one can toggle the magnetization of garnets at a frequency reaching 50 GHz. Such a high-frequency, large-amplitude magnetization switching with minimal heat dissipation in garnets, resulting in an increase in temperature of material of only about 0.6 K, opens up new possibilities in the field of topological opto-spintronics and cold ultrafast magnetic recording.

STRESZCZENIE

Ultraszybki magnetyzm jest intensywnie rozwijającym się obszarem fizyki skoncentrowanym na zrozumieniu mechanizmów oddziaływania ultrakrótkich impulsów laserowych z materią. Sterowanie magnetyzacją wyłącznie za pomocą impulsów laserowych kryje w sobie ogromny potencjał aplikacyjny, umożliwiając najszybszy możliwy zapis danych przy minimalnej dyssypacji energii. Głównym celem niniejszej pracy jest zrozumienie koherentnej dynamiki nietermicznego przełączania magnetyzacji poprzez kontrolę anizotropii magnetycznej w warstwach granatów domieszkowanych jonami kobaltu w szerokim zakresie temperatur. Badania zostały przeprowadzone na nowym, specjalnie zaprojektowanym, przygotowanym i zoptymalizowanym układzie stosując i rozwijając unikatową metodę czasowo-przestrzennego obrazowania magnetooptycznego dynamiki precesji oraz przełączania magnetyzacji.

Wykorzystując możliwości eksperymentalne zbadano nowe scenariusze przełączania fotomagnetycznego zarówno w przypadku przełączenia stanu monodomenowego, wielodomenowego jak i w przypadku przełączenia pojedynczych domen cylindrycznych. Analiza trajektorii przełączeń między wieloma stanami magnetyzacji umożliwiła wykazanie braku wzajemności dynamiki przełączania, wynikającego z magnetokrystalicznej symetrii granatów oraz momentu skręcającego indukowanego liniowo spolaryzowanymi impulsami lasera o ortogonalnych kierunkach. Do wyjaśnienia dynamiki przełączenia magnetyzacji opracowano model teoretyczny w ramach formalizmu opartego o równanie Landaua-Lifshitza-Gilberta, zawierający tensor fotomagnetycznej podatności.

W pracy zaprezentowano po raz pierwszy efekt nietermicznego, zwrotnego przełączania magnetyzacji indukowanego wyłącznie kolejnością femtosekundowych impulsów lasera bez zmiany ich kierunku polaryzacji. Dotychczas efekt zwrotnego przełączania obserwowano wyłącznie w materiałach metalicznych, w których przełączenie magnetyzacji bazuje na mechanizmie termicznego rozmagnesowania. Nowy efekt 'zimnego' zwrotnego przełączania magnetyzacji zaobserwowano przy zastosowaniu warstw granatów wytworzonych bez zniekształceń symetrii magnetokrystalicznej w bardzo szerokim zakresie temperatur $\pm$ 100°C. Zaprezentowano również możliwość sterowania energią przełączania, związaną z dyssypacją ciepła, poprzez zmiany intensywności impulsu lasera oraz magnetycznej anizotropii granatów. Pokazano również że, czas przełączenia i jego efektywność są wzajemnie konkurencyjnymi parametrami. Wykorzystując nowy mechanizm zwrotnego przełączania w granatach możliwe jest uzyskanie zapisu magnetycznego z częstotliwością sięgającą 50 GHz. W trakcie takiego zapisu temperatura materiału zmieni się o około 0.6 K, co otwiera nowe możliwości w dziedzinie topologicznej opto-spintroniki i zimnego ultraszybkiego zapisu magnetycznego.

ACKNOWLEDGMENTS

The results presented in this doctoral dissertation are the culmination of over 4 years of research and measurements conducted at the Faculty of Physics, University of Białystok. This period marked a new chapter in my academic journey, and I would like to express my heartfelt gratitude to those who made this work possible.

First and foremost, I would like to extend my sincere appreciation to my supervisor, Prof. Andrzej Stupakiewicz. He provided me with the opportunity to join the research group and this project, offering invaluable guidance not only in scientific matters but also in various aspects of life. Throughout the entire duration of this work, Prof. Stupakiewicz acted as a mentor, and I owe much of the success of this dissertation, along with numerous publications, to his unwavering support, vast knowledge, experience and patience.

I am also deeply thankful to Prof. Andrzej Maziewski, a key figure at the Department of Magnetism, Faculty of Physics, for his continuous support, engaging discussions, and guidance in navigating the intricate realm of magnetism.

Furthermore, I wish to express my gratitude to Dr. Ilya Razdolski for his invaluable theoretical and simulation support, as well as for the many fruitful discussions. I would also like to extend my thanks to Professor Andrei Kirilyuk and Professor Alexey Kimel for their discussions and for facilitating international cooperation during my internship, which allowed me to gain valuable experience in the welcoming atmosphere of Radboud University in Nijmegen. I also appreciate their involvement in organizing the COST-MAGNETOFON event series.

My gratitude extends to the academic community, especially my fellow doctoral students. Antoni Frej, I thank you for inviting me to collaborate on this project and for the memorable times we spent in Bialystok and during our travels abroad. To Artsiom Kazlou, I am grateful for the numerous scientific and non-scientific discussions we have shared, and to Vladislav Ozerov, for his assistance with magnetic simulations. Special thanks go to Wojciech Dobrogowski for his technical support with software and his contributions to the development of measurement systems.

Last but not least, I want to convey my gratitude to everyone who, at various stages of my life and educational choices, nurtured my interest in physics and allowed me to delve deeper into the subject. I am particularly thankful to my Brother Maciej for activating my interest in science, mathematics, and physics. His readiness and ability to address complex issues in these fields were instrumental in my journey through education. To all who have supported and understood me, thank you.

The work described in this thesis was financially supported by the TEAM project POIR.04.04.00-00-413C/17 operated within the Foundation for Polish Science Program co-financed by the European Union under the European Regional Development Fund.

CONTENTS

ACRONYMS

AO-HDS All-Optical Helicity-Dependent

AO-HIS All-Optical Helicity Independent Switching

CCD Charge-Coupled Device

CW Continuous Wave

DG Delay Generator

EMA Easy Magnetization Axes

FMR Ferromagnetic Resonance

FWHM Full Width at Half Maximum

GGG Gadolinium Gallium Garnet

LLB Landau-Lifshitz Bloch

LLG Landau-Lifshitz Gilbert

LED Light-Emitting Diode

MCD Magnetic Circular Dichroism

MO Magneto-Optical

MOKE Magneto-Optical Kerr Effect

OPA Optical Parametric Amplifier

ROI Region Of Interest

YIG Yttrium Iron Garnet

YIG:Co Co-doped Yttrium Iron Garnet

1

INTRODUCTION

Modern technology is deeply intertwined with the explosion of information and the continual growth of data. Our society has transitioned into an information-centric era, driven by the digital age and the ubiquitous presence of data. Over the years, the sheer volume of data has experienced a dramatic increase. This growth shows no signs of slowing down, ushering in an era where data management, storage, and accessibility are paramount. In fact, our world entered the so-called era of zettabytes (10^{21}bytes), generating an enormous value of 1 zettabyte of information for the first time. It was estimated that in 2016, only Internet protocol traffic itself surpassed this value, and by 2023, the total volume of collected data had exceeded 100 zettabytes. This trend is constant, with the amount of information continuing to grow rapidly.

The majority of the world's stored data utilizes magnetic moments to record binary information. Magnetic anisotropy, which creates an energy barrier separating magnetic states, provides bistability and has been used with great success in the deterministic recording of binary information. In the conventional approach, all of today's commercially available technologies, such as hard disks, magnetic random access memories, or magnetic tapes, use an external magnetic field to manipulate the magnetization states. However, generating a strong and rapid magnetic field in practical devices is directly associated with energy dissipation and heating, which limits the capabilities of these devices.

Indeed, to reorient the magnetic state, one must overcome the potential energy barrier ΔU that separates two magnetic states, and this barrier is defined as $\Delta U = KV$, where K represents the anisotropy and V is the bit volume. The Landauer limit expanded to applicational devices, leads to the condition of $\Delta U \geq 60 k_B T$, where k_B is the Boltzmann constant and T is the temperature, restricting the size of minimum energy barrier ensuring the bit's stability and suitability for recording in practical devices [1]. Moreover, as a recording density increases, the size of the single-bit volume needs to be minimized. This reduction in bit size translates into an increase in magnetic anisotropy, which, in turn, requires greater coercivity to reverse magnetization. Ultimately, increased coercivity necessitates the use of stronger magnetic fields, which become increasingly difficult and energy-intensive to produce. This challenge of bit size, stability, and writability is often referred to as the trilemma of magnetic recording.

In the realm of modern data management, the demand for higher bit densities is coupled with the need for faster information processing, enabling greater switching speeds while simultaneously reducing energy dissipation. Consequently, significant efforts have been dedicated to the development and exploration of innovative methods for manipulating magnetization. This quest for novel mechanisms, materials, and solutions has given rise to concepts such as current-induced magnetization reversals, Spin-Transfer Torque [2], Spin-Orbit Torque [3], as well as the manipulation of magnetization through electric fields [4] or strain [5].

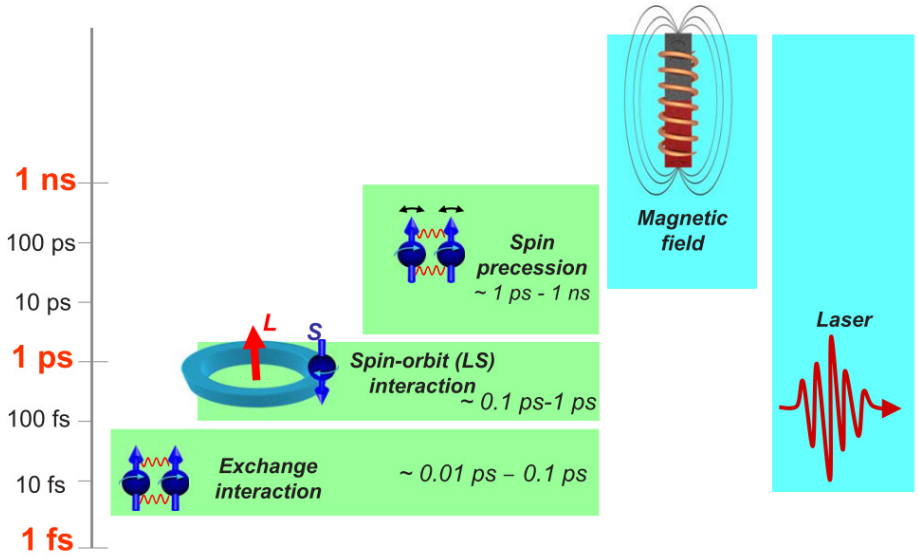

Figure 1.1: Timescales of magnetic interactions. Utilizing the ultrashort duration of the optical stimulus allows for widening the possibility of studying magnetization dynamics. Adapted from [11].

Concurrently, the field of light-matter interaction, driven by advancements in laser technology, has introduced a new paradigm. Ultrashort light pulses have been harnessed to manipulate and switch magnetization[6–9]. To date, ultrafast magnetization switching has been achieved in both metallic materials, where it relies on material heating, and in nonthermal ways in dielectrics through the photo-magnetic effect, wherein light-induced anisotropy drives magnetization movement. While the switching of metals can be achieved in increasingly newer materials, a more comprehensive examination of the possibilities for adjusting anisotropy and consequently modifying magnetization switching in dielectrics must be undertaken, as discussed in this work.

1.1 ULTRAFAST MAGNETISM WITH LIGHT

One of the fastest stimulus known to interact with the magnetic state of matter is a femtosecond laser pulse. The incomparable time resolution provided by this ultrashort light stimulus has offered insights into magnetization dynamics at scales that were previously unreachable. Its ultrashort duration provides timescales that go beyond the speeds of the fundamental interactions between electrons, lattices, and spins [10]. Such a rapid interaction disrupts the thermodynamic equilibrium in magnetic materials, creating the theoretical challenge of the time-dependent magnetic anisotropy parameter. Moreover, as shown in Figure 1.1, a femtosecond optical pulse is capable of affecting and probing magnetic systems on a wide timescale, corresponding to the fastest exchange interactions (0.01 ps – 0.1 ps), through spin-orbit interactions (0.1 - 10 ps), up to magnetic precession (1 ps - 1 ns) [11].

Controlling and probing the magnetization state on this unique short timescale has become a widely studied field due to its intriguing fundamental implications and potential practical applications. Since 1996, when a precursor experiment involving subpicosecond demagnetization in nickel [12] was triggered by a 60 fs laser pulse on a timescale much

faster than the characteristic time of any known at that time elementary interaction of spins with other reservoirs of angular momentum in solids [13, 14].

Afterward, the interest in the field was fueled by a plethora of counter-intuitive experimental findings that challenged state-of-the-art theories in magnetism. Moreover, it is also believed that ultrafast magnetism can help us to understand the fundamental limits on the time as well as the energy dissipation required for writing magnetic bits. Thus the field has a potential for a tremendous impact on future magnetic data storage technology. Special attention in this case is paid to the materials, mechanism, and scenarios to switch magnetization between stable bit states at the fastest possible and, simultaneously, the least dissipative way.

The study and subsequent understanding of magnetization dynamics, especially on ultrafast timescales, are essential for furthering both basic and applied research.

1.2 MAGNETIZATION DYNAMICS

In classical physics, an applied external magnetic field $\boldsymbol{H}$ exerts a torque $\boldsymbol{T}$ on a magnetic moment $\boldsymbol{m}$, attempting to align it with the field vector. This relationship can be described as:

$$\boldsymbol{T} = \boldsymbol{m} \times \boldsymbol{H} \tag{1.1}$$

The torque $\boldsymbol{T}$ is responsible for the rate of change of angular momentum $d\boldsymbol{L}/dt = \boldsymbol{T}$, which is connected to the magnetic moment via the gyromagnetic ratio γ, defined as $\gamma = g\mu_B/\hbar$, where μ_B is the Bohr magneton, $\hbar$ is the reduced Planck constant, and g is the electron's g-factor. For a single electron without any spin-orbit interactions, γ is approximately 28 GHz/Tesla.

The magnetic moment can be expressed as:

$$\boldsymbol{m} = -\gamma \boldsymbol{L} \tag{1.2}$$

where $\boldsymbol{L}$ represents angular momentum.

Connecting equations (1.1) and (1.2), we can obtain the Landau-Lifshitz equation, which describes the dynamics of the magnetic moment in response to torques:

$$\frac{d\boldsymbol{m}}{dt} = -\gamma \left(\boldsymbol{m} \times \boldsymbol{H}\right) \tag{1.3}$$

In the macroscopic or general case of a ferromagnet, the individual magnetic moments are replaced by magnetization $\boldsymbol{M}$, which characterizes the distribution of numerous magnetic moments within the material volume, and can be defined as $\boldsymbol{M} = \frac{dm}{dV}$. Any change in the direction of uniformly distributed magnetization within the material must adhere to the conservation of angular momentum.

This equation can be generalized to an effective anisotropy field $\boldsymbol{H} = \boldsymbol{H}_{eff}$ which contains any intrinsic or external contributions affecting the material. The resultant movement of magnetization, as shown in Figure 1.2a, involves circular precession with a frequency of $\omega = \gamma \boldsymbol{H}_{eff}$ around the effective magnetic field, through which the tip of the magnetization vector passes. In the absence of damping, this scenario implies an infinite duration of precession.

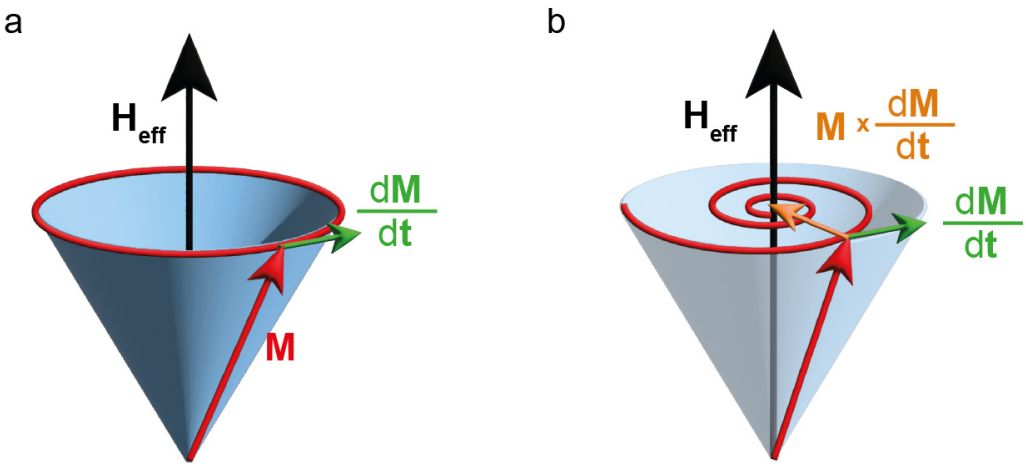

Figure 1.2: Schematic representation of the precession of magnetization vector M around effectiv anisotropy field H_{eff}, both a) without damping and b) with a damping term.

Incorporating damping, as described by Gilbert, transforms the equation into the form represented by the Landau-Lifshitz Gilbert (LLG) equation:

$$\frac{d\boldsymbol{M}}{dt} = -\gamma\left(\boldsymbol{M}\times\boldsymbol{H}_{eff}\right) + \frac{\alpha}{M_s}\left(\boldsymbol{M}\times\frac{d\boldsymbol{M}}{dt}\right) \tag{1.4}$$

Here, α represents a damping term introduced by Gilbert, which places a limit on the number of oscillations, reflecting real-world conditions and $M_s$is saturation magnetization. The gyromagnetic ratio values, resulting in magnetization precession frequencies at the gigahertz scale, underscore the necessity of employing ultrafast methods to sample and study the observed dynamics.

The coherent magnetization dynamics described above assume that the magnetization value remains constant during the evolution. However, substantial temperature changes approaching or exceeding the Curie temperature T_C, induced by for example the absorption of light in metallic materials, can significantly alter the magnetization vector length, potentially leading to demagnetization. In such cases, a different formalism described by the Landau-Lifshitz Bloch (LLB) equation should be employed [15]. This approach is worth noting due to the plethora of various recent applications, such as heat-assisted magnetic recording or temperature-based ultrafast magnetic dynamics and magnetization switching, which have been the subject of intense research in recent years.

1.3 THERMAL MECHANISMS OF ALL-OPTICAL SWITCHING OF MAGNETIZATION

The most desired way of manipulating the magnetization of materials is controlling its reversals, leading to deterministic magnetization switching. The control of the magnetization state relies on the introduction of symmetry-breaking mechanisms to ensure determinism. Traditionally, magnetic fields are used for this purpose. Applying a magnetic field in a specific direction can switch the magnetization. However, to revert the magnetization to its previous state or an antiparallel orientation, changing the applied field direction is necessary. Any subsequent magnetic field pulse in the same direction will not trigger a switch because it generates zero torque.

Light, on the other hand, can introduce symmetry-breaking through the control of polarization. The helicity of polarization, whether left or right, or the orientation of the

plane of linearly polarized light, can influence the direction of switching, whether forward or backward.

However, the most intriguing aspect of controlling magnetic states does not require changing of the pulse's polarization, which would contradict the symmetry inversion. In this scenario, a toggle-switching effect becomes possible, a regime solely demonstrated in the form of thermal demagnetization.

More than a decade has passed since the groundbreaking experiment demonstrating how femtosecond light pulses could alter the magnetization state in ferromagnetic nickel, resulting in ultrafast demagnetization [12]. This breakthrough paved the way for the first-ever demonstration of all-optical magnetization switching using femtosecond laser single pulse [6].

In ferrimagnetic GdFeCo amorphous alloys, where Gd and FeCo sublattices are antiferromagnetically coupled, it was observed that ultrafast switching could be triggered by a single circular-polarized femtosecond laser pulse. For the first time, a light pulse not only had the capacity to demagnetize the sample or induce precessional movement [16] but also offered the possibility to switch it without the need for any external magnetic field. The determinism of the switching process was achieved through the selection of light helicity, which could define the final magnetic state. Subsequent investigations, as depicted in Figure 1.3, established the ultrashort switching timescale of tens of picoseconds[17].

Initially, the impact of light on the GdFeCo alloy was understood to have a dual nature. It involved ultrafast optical absorption, rapidly heating the electron bath within the material, followed by the inverse Faraday effect, which acted as an effective opto-magnetic field [18]. Further experiments, employing synchrotron time-resolved X-ray magnetic circular dichroism (XMCD), allowed for the separation of the influence of the individual Gd and Fe sublattices, revealing their distinct dynamics [19]. As presented in Figure 1.4, it was demonstrated that a single femtosecond laser pulse could demagnetize the Fe sublattice four times faster than the Gd sublattice. These varying dynamics, leading to different times for the magnetization to drop to zero, resulted in the emergence of a transient ferromagnetic state. Given the strong antiferromagnetic coupling between the Gd and Fe sublattices, this change in magnetization state occurred after 1.2 picoseconds.

This result provided the suggestion that switching should be possible to achieve regardless of the polarization state of the light. This mechanism, called All-Optical Helicity Independent Switching (AO-HIS), was presented shortly later [7]. A single 100 fs laser pulse exposed a $Gd_{24}Fe_{66.5}Co_{9.5}$ sample acting as a rapid heating stimulus that was capable to switch the magnetization As shown in Figure 1.5, each subsequent pulse reverses the observed magnetization state, giving a toggle effect making the final magnetization state dependent on the parity of incident pulses.

The thermal origin of this switching is linked to the absorption properties of the metallic material. Therefore, parameters related to wavelength and polarization are not crucial. However, as previously mentioned, circularly polarized light illumination can supplement AO-HIS with Magnetic Circular Dichroism (MCD), which can differentiate absorption based on light helicity [20].

Since the initial experiments, which were primarily focused on rare earth transition metal alloys like GdFeCo, new materials enabling helicity-independent all-optical switching have been discovered [21–23]. Similar magnetization behavior has been observed in other multi-sublattice alloys such as Gd/Co [24]and (Gd,Tb)Co with varying proportions of Gd and Tb [25]. The inclusion of Tb in materials, as it has a higher Curie temperature, was aimed to increase the material's anisotropy consequently reducing the size of

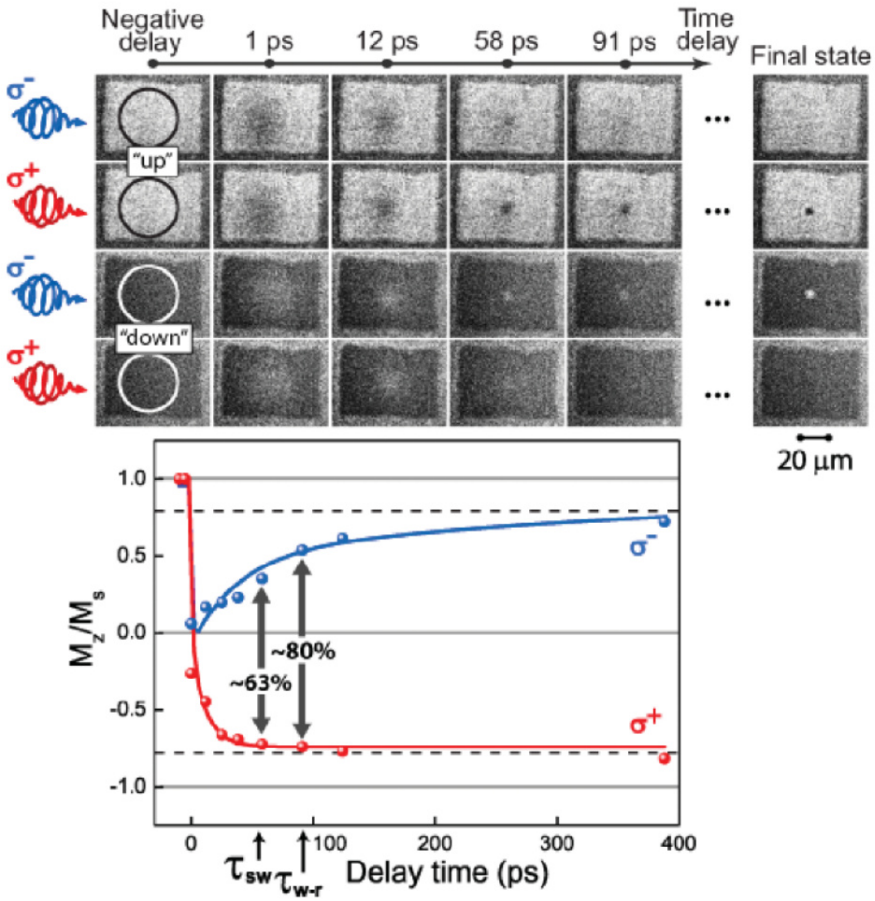

Figure 1.3: Time-resolved images, and extracted from them averaged magnetization, presenting all-optical helicity-dependent magnetization switching in $Gd_{24}Fe_{66.5}Co_{9.5}$ alloy triggered by right-handed (σ^+) and left-handed (σ^-) circularly polarized pulses. Adaptet from [17].

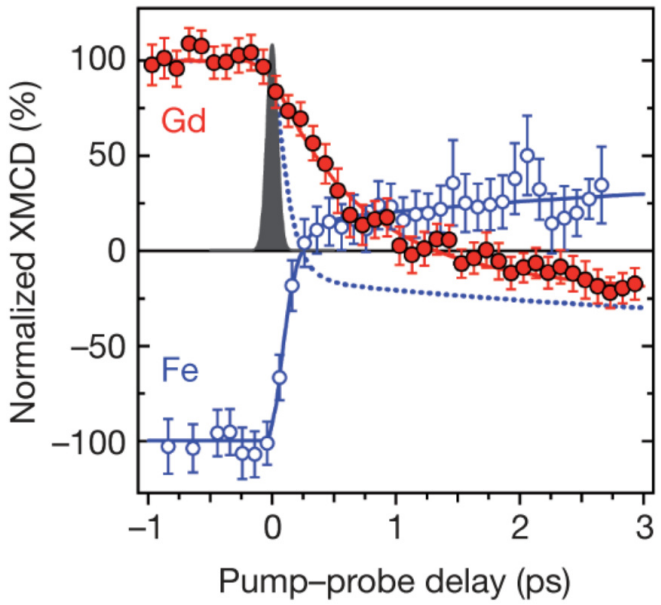

Figure 1.4: The time and element-resolved dynamics in GdFeCo, as measured using the XMCD method. The distinct dynamics of the two sublattices give rise to a transient ferromagnetic state, which plays a crucial role in the magnetization reversal process. Adapted from [19].

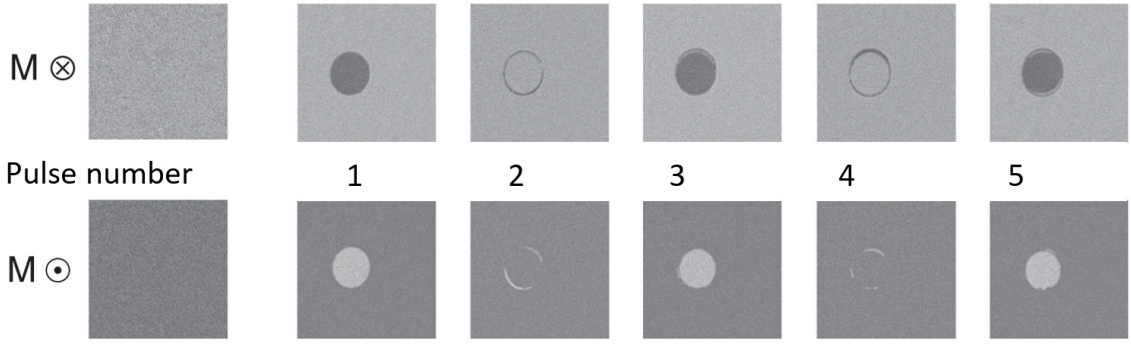

Figure 1.5: Magneto-optical images of a metallic GdFeCo film switched by a sequence of ultrashort laser pulses. Each subsequent laser pulse excites the same domain of the film and reverses the magnetization state by either writing or removing a "magnetic bit". Adapted from [7].

the switched bit. Furthermore, switching has also been demonstrated in rare earth-free Heusler alloy Mn_2Ru_xGa [26, 27].

Subsequently, the range of materials was expanded to include synthetic multilayers with nanostructures of Gd/Co [28], Tb/Co [29–31]. This rapid development has also pushed the achievable frequencies in materials, defining a frequency limit of 3 GHz in GdFeCo [32] and demonstrating write/read cycles in Si/GdCo at an astonishing 140 GHz [33].

On the other hand, All-Optical Helicity-Dependent (AO-HDS) switching, where circularly polarized light helicity determines the switching, has been observed in various materials [8, 34, 35]. However, in this mechanism, a single pulse is typically insufficient to complete the magnetization switching. Multiple pulses, often ranging from tens to hundreds, are necessary for full switching [36], which significantly limits effective write/erase frequencies. This type of switching involves two main steps: helicity-independent nucleation of switched domains and subsequent helicity-dependent deterministic domain wall motion. Despite the need for numerous pulses, this mechanism is noteworthy due to its applicability in a wide range of well-established materials. These materials include synthetic ferrimagnets [37], Tb/Co alloys [38], multilayers like Pt/Co/Pt, [35, 36, 39–41] and Fe/Pt structures, offering the potential for ultra-high-density recording [42, 43]. Subsequent advancements involving pulse packets have reduced the required number of pulses to as few as four [44]. However, achieving switching with just a single pulse has not been realized thus far.

The ultrashort optical stimulus can also be harnessed to thermally modify the material's anisotropy. Transient heating has the capacity to manipulate the magnetocrystalline anisotropy of the material. This concept was put into practice in bismuth-substituted yttrium iron garnet [45]to achieve heat-assisted sub-nanosecond precessional switching. The precession of magnetization was initiated by a transient thermal alteration of the growth-induced crystalline anisotropy induced by an optical pulse, all in the presence of a static perpendicular magnetic field. The transient and enhanced, anomalously large damping played a crucial role in providing a pathway for deterministic magnetization switching.

1.4 NONTHERMAL MECHANISM OF ALL-OPTICAL PHOTO-MAGNETIC SWITCHING

The feasibility of achieving nonthermal all-optical switching, without substantial heating in the medium, mainly relies on the photo-magnetic effect, which has a time-dependent impact on the material's magnetic anisotropy contributing to the light-induced component [46–48]. This effect has been extensively studied in dielectric garnets, known for the substantial strength of the photoinduced anisotropy field, reaching several hundred gauss, comparable to intrinsic anisotropy [48]. This strong stimulus can lead to magnetization deviations of up to 20° from equilibrium. Further estimations of the effective photo-magnetic field inducing high-amplitude precession were conducted in [49], analyzing sub-switching and nonlinear regimes of photoinduced magnetization dynamics.

Moreover, experimental evidence has demonstrated that in Co-doped Yttrium Iron Garnet (YIG:Co) thin films on Gadolinium Gallium Garnet (GGG) (001)-plane substrate with 4° miscut angle [9], it is possible to permanently switch the magnetization state within only 20 ps using a single ultrashort linearly polarized laser pulse. When the light pulse is polarized along either the [100] or [010] axis, it resonantly excites specific $d - d$ transitions

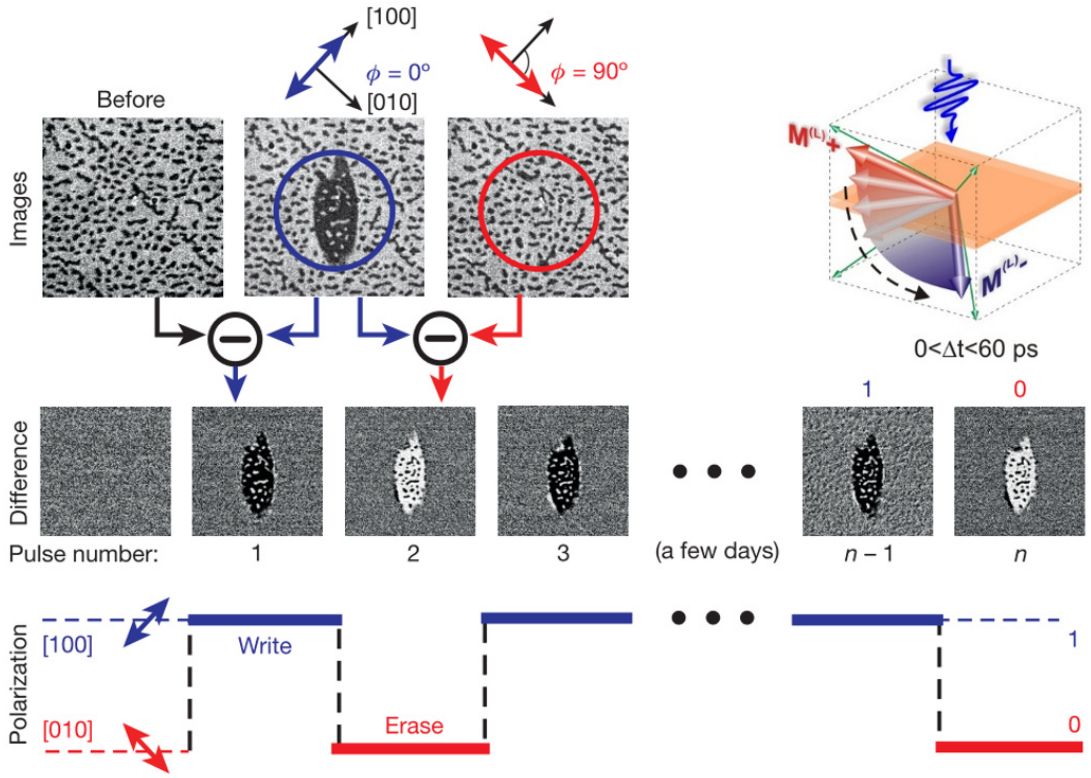

Figure 1.6: Nonthermal ultrafast photo-magnetic switching in YIG:Co. The "magnetic" bit can be written by a single femtosecond laser pulse polarized along the [100] axis. Subsequent similar pulse polarized orthogonally along the [010] axis can erase it. The final magnetization state can be controlled by the polarization plane of an incident laser pulse. Adapted from [9].

in Co ions, thereby modifying the magnetic anisotropy. This photo-induced anisotropy can break the degeneracy between the domain states and, consequently, permanently switch the magnetization. The idea of writing and erasing magnetic 'bits' using nonthermal photo-magnetic switching is presented in Figure 1.6.

However, magnetization switching was demonstrated for only one of the four possible phases that can be induced in YIG:Co. The revealed time-resolved dynamics were observed on an ultrafast timescale but only for the averaged, less detailed states that obscured the dynamics in specific domains.

A detailed analysis of the selection rules, such as possible photon energies and light polarizations for achieving all-optical switching, as well as modeling of switching trajectories was presented in the reference [50]. This analysis reveals the feasibility of switching using two-photon energies of 0.95 eV (λ = 1300 nm) and 1.1 eV (λ = 1140 nm), which have since been expanded into the telecommunication range at 1.1 eV (λ = 1590 nm) [51].

Additionally, despite optical switching, resonant ultrafast phononic switching has been demonstrated in YIG:Co using light pulses within the spectral range of 20-40 THz [52]. This phenomenon relies on altering the magneto-elastic energy contribution via strain induced by exciting longitudinal optical phonons with laser pulses that precisely match the lattice vibration frequencies. The changes in magneto-elastic energy induce magnetization precession and consequently leads to the magnetization switching.

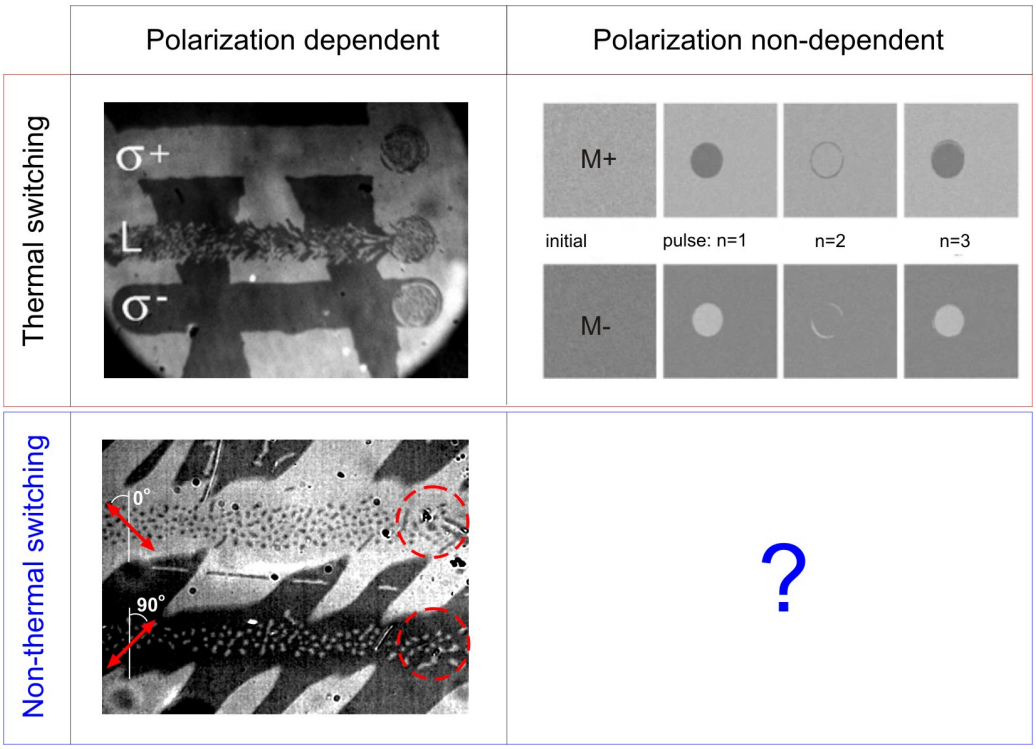

Figure 1.7: The ultrafast all-optical magnetization switching regimes from the point of view of polarization control. Adapted from [6, 7, 50].

The switching time depends on the frequency of the magnetization precession, the effective anisotropy field, and the magnetization trajectory between two defined magnetic states. Thanks to its precisely directed resonant character, this process minimizes heat generation and energy loss, reducing them close to their lowest possible limits. This lack of thermal effects results in very high switching repetition rates, exceeding 20 GHz [53]. This particular research correlates switching times with the effective anisotropy field but has not explored changes in its specific components, such as magnetocrystalline anisotropy.

Nonthermal magnetization switching has only been demonstrated in a deterministic form. In this case, switching magnetization requires changing the direction of linearly polarized light to orthogonal at each cycle of writing and removing the magnetic "bit". As summarized in Figure 1.7, unlike thermal effects, achieving toggle switching without the need for polarization changes has not been demonstrated. This approach is of great interest for practical applications as it eliminates the requirement for additional elements to control the polarization state.

However, based on Curie's principle, which postulates that "the symmetries of the causes are to be found in the effects", it might seem counterintuitive to achieve non-deterministic toggle magnetization switching. Conventionally, it is believed that heating alone, which does not have the symmetry of a magnetic field, cannot lead to a deterministic reversal of magnetization. Nevertheless, as mentioned earlier, if the heating is induced by a femtosecond laser pulse and, therefore, occurs on an ultrafast timescale, it can indeed facilitate toggle switching of magnetization between stable bit-states without any need for a magnetic field [7].

In situations where each excitation event is identical and the symmetry of the cause remains constant, achieving toggling implies that the symmetry of the effect changes from

pulse to pulse. Such a toggle switching mechanism should become feasible, especially in cases of ultrafast precessional switching, a concept that will be explored and verified in this dissertation.

1.5 SCOPE OF THE THESIS

The doctoral dissertation represents novel research aimed at understanding the mechanisms and scenarios behind all-optical magnetization switching without relying on heat dissipation. The results contained in it relate to the study of ultrafast, nonthermal photo-magnetic switching in YIG:Co thin films with and without muscut angle of GGG substrates. The main objective of this thesis is to understand the dynamic mechanisms and scenarios of nonthermal magnetization switching in YIG:Co. This thesis is primarily dedicated to finding ways to enhance the efficiency of this switching method, with a special focus on its spatial, temporal, and heat dissipation characteristics. It underscores how these properties can be modulated through the manipulation of the effective anisotropy field across a wide temperature range.

Following the introductory section, the next two chapters explore the methods employed in this research. Chapter 2 provides an overview of the properties of the investigated garnet samples. It begins by introducing garnets as widely used model materials, with a specific focus on yttrium iron garnets and the substitution of cobalt ions in the material's sublattices. The chapter then gives an insight into the magnetic and magneto-optical properties of the used samples, particularly emphasizing the domain structure and cubic symmetry of the garnet. Lastly, it discusses methods for achieving magnetization reversal using an external magnetic field and via the photo-magnetic effect.

Chapter 3 gives detailed information about the experimental methods utilized in the thesis, discussing their capabilities, limitations, and underlying principles. It begins by introducing the Faraday effect and the topic of magneto-optical imaging, with an emphasis on the transmissive Faraday geometry and static imaging. Subsequently, it covers dynamical measurements that enable observations on the ultrafast scale. Starting with the fundamentals of femtosecond lasers, the chapter provides a detailed description of the setup used. It explains the general pump and probe method and the experimental setups that offer insights into the temporal and spatial dynamics of ultra-fast magnetization changes. Finally, the chapter spotlights the advanced three-color femtosecond setup developed at the Laboratory of Femtosecond Spectroscopy, Faculty of Physics, University of Bialystok, emphasizing its functionality, flexibility, and capabilities for time-resolved image processing using both single and multiple laser pulses across a wide spectral and temperature range.

The subsequent chapters present the results obtained from the YIG:Co samples. Chapter 4 investigates the ultrafast photo-magnetic switching for various initial magnetization scenarios in garnet with non-zero miscut angle. These scenarios encompass single-state switching in monodomain surroundings, single-state switching in multi-domain surroundings, and multi-state switching in multi-domain surroundings. Furthermore, it examines the spatial properties of switched domains, demonstrating the ability to target switching within a single bubble domain. The achievement of bubble domain switching is facilitated by revealing the non-equivalence between the energies required for switching specific domain states. By reducing the domain size, we further lower the threshold laser fluence for photo-magnetic switching.

Chapter 5 provides an in-depth exploration of the temporal properties of multi-state magnetization switching dynamics. It discusses the non-reciprocity of switching trajectories in cases of simultaneous multi-state switching which has not been observed previously. Experimental and simulation results are thoroughly analyzed and explained through the concept of photo-magnetic torque symmetry. The data is compared with simulations employing a theoretical model based on the Landau-Lifshitz Gilbert equation. The results reveal a significant interplay between torque variation and the anisotropy energy landscape, shaping a mutual relationship that defines the choice of magnetization trajectory.

Chapter 6 investigates methods for controlling photo-magnetic switching parameters by manipulating the effective field of magnetic anisotropy. It starts with a description of the new nonthermal toggle regime of magnetization switching in "miscut-free" YIG:Co with a pure cubic magnetic symmetry. The chapter proceeds to explore the dynamics of magnetization switching, its dependence on laser polarization, and the achievable switching repetition rates within the toggle regime. Lastly, it considers the impact of temperature, which strongly affects the magnetocrystalline anisotropy and, consequently, the efficiency of magnetization switching. The control of magnetic anisotropy required for the 'cold' toggle switching is accompanied by lower energy of the heat dissipations, but this energy and the switching time are shown to be competing parameters.

In conclusion, the final chapter synthesizes the findings presented in the thesis and provides insights into future challenges, ideas, and remarks concerning nonthermal magnetization switching with light.

2

FERRIMAGNETIC CO-DOPED YTTRIUM-IRON GARNETS

This chapter will be dedicated to describing the properties of Co-doped yttrium iron garnet thin films which are grown on $Gd_3Fe_5O_{12}$ substrates in (001) plane with and without miscut angle.

Firstly, we will begin by presenting an overview of undoped yttrium iron garnets, detailing their composition and crystalline structure. Following that, we will introduce and describe the specific samples employed in our study, along with their intrinsic magnetic anisotropy affecting the magnetic as well as magneto-optical characteristics. Lastly, we will investigate the magnetic domain structure and pathways for magnetization reversal using an external magnetic field in the samples with different constants of the magnetic anisotropy and miscut angle of the substrates.

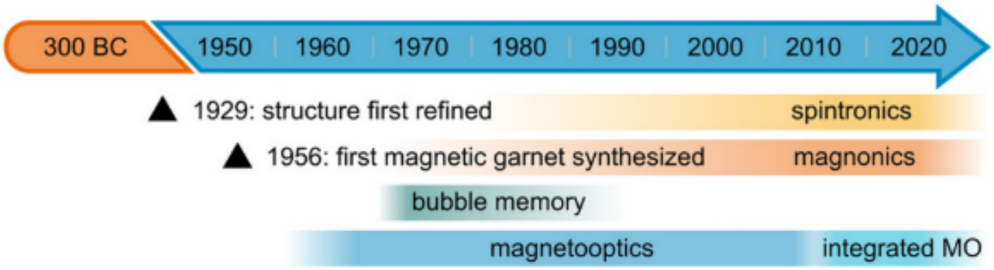

Figure 2.1: Timeline presenting broad garnets application. Adaptet from [61].

2.1 CRYSTALLOGRAPHIC STRUCTURE OF YIG

Generally, iron garnets are exemplary dielectric model materials that have been extensively utilized in the field of magnetism for over 50 years. Since their first synthesis in 1956 [54, 55] various types of garnets have been developed and customized, providing opportunities and paving the way for numerous applications and fundamental studies due to their versatility. The timeline, which provides insight into the widespread use of garnets, not only within the magnetism community, is summarized in Figure 2.1. The synthesis methods developed from the investigation performed on iron garnet Yttrium Iron Garnet (YIG) bulk discs [56], through the thin film grown by liquid phase epitaxy [57], up to the pulse laser deposition [58] and sputtering techniques, enabling the creation of garnet layers with the nanometer-scale thickness [59, 60].

The synthesis of YIG, renowned for its distinctive ferrimagnetic properties [62, 63] opened new opportunities for material studies. Initially, garnets attracted attention due to their narrow ferromagnetic resonance absorption line at GHz frequencies, which resulted in a very low damping of magnetic excitations creating a pathway for an integration in microwave devices. During the 1970s and 1980s, magnetic garnets were extensively investigated as potential candidates for magnetic memory devices. The concept of bubble memories, originally developed using orthoferrites, was later adapted to magnetic garnets [64]. The tunability of magnetic properties through doping with rare-earth elements and the design of magnetic anisotropy, including uniaxial [65] and growth-induced [66] components, made garnets the material of choice for magnetic bubble memories. However, with the advancement of semiconductor technology, interest in bubble memories declined. Nonetheless, the underlying principle remains relevant, as the bubble concept can be viewed as a topological equivalent of skyrmions, holding promise for racetrack memory applications[67].

Optical and magnetic properties of a synthetic material are determined by its chemical composition. Garnets possess a cubic crystal structure and belong to the space group O_h^{10} ($la\bar{3}d$ in international notation). Each unit cell of garnets contains 8 formula units of $\boldsymbol{C}_3\boldsymbol{A}_2\boldsymbol{D}_3O_{12}$. In rare-earth iron garnets, the $\boldsymbol{C}$ position is occupied by trivalent rare-earth metals, which can vary from yttrium to lutetium, and these ions are located in dodecahedral positions. The $\boldsymbol{A}$ and $\boldsymbol{D}$ positions are occupied by the Fe^{3+} ions in octahedral positions (surrounded by six oxygen ions) and tetrahedral positions (surrounded by four oxygen ions), respectively. In total, a unit cell consists of 24 dodecahedral $\boldsymbol{C}$ cations with orthorhombic symmetry, 16 $\boldsymbol{A}$ octahedral cations with trigonal symmetry, 24 $\boldsymbol{D}$ tetrahedral cations with tetragonal symmetry, and 96 O^{2-} anions. The non-equivalence of

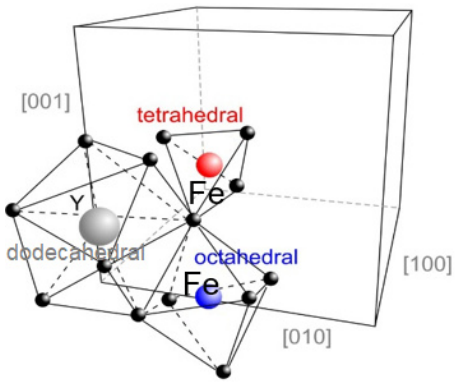

Figure 2.2: The unit cell of YIG. Adapted from [50].

both octahedral and tetrahedral positions is a distinctive aspect of the crystallographic structure of garnets. In the case of octahedra, the local axes of distortion align with the <111>-type axes, while for tetrahedra, they align with the <100>-type axes. Consequently, there are four distinct types of octahedral positions and three distinct types of tetrahedral positions within the garnet structure as presented in Figure 2.2.

For the pure (undoped) YIG, the chemical composition can be represented as:

$$Y_3[Fe_2](Fe_3)O_{12}$$

where different parentheses signify different crystallographic sites. The cubic lattice constant equal 12.376 Å [61, 68]. The magnetic properties arise due to the presence of iron ions located in both the octahedral and tetrahedral sublattices. The antiparallel alignment of magnetization in these ions, which is not completely compensated, results in a net magnetic moment, resulting in the material's ferrimagnetism. The total magnetization is a summation of the magnetizations from each of these three sublattices.

Typically, garnets can be prepared in the form of solid crystals (bulk). However, different substrates might be utilized to develop garnet thin films with a thickness of less than a dozen micrometers. The most popular substrate, due to its optical transparency and its adaptation of the lattice constant, is GGG, with the composition $Gd_3Ga_5O_{12}$. The GGG substrate, with its high purity and a lattice constant size of 12.38 Å, provides a very small lattice mismatch of 0.03%, ensuring optimal fabrication parameters. By controlling the growth parameters such as melt temperature and growth speed, both cubic and uniaxial anisotropies can be tailored. All of the samples used in the thesis were produced using the liquid phase epitaxy method on the (001)-plane GGG substrate, each with a thickness of 400 µm.

2.2 MAGNETIC PROPERTIES OF INVESTIGATED SAMPLES

The key factor defining garnet's magnetic properties and the photo-magnetic effect is the material's magnetic anisotropy. In the bulk monocrystal, the energy of magnetocrystalline anisotropy reflects the magnetic symmetry and easy magnetization axes in the crystal. Additionally, when producing thin films, it is possible to add additional uniaxial growth-induced anisotropy. The energy of magnetic anisotropy, which is a function of the orientation of the magnetization vector relative to the main crystallographic axes, can be written down as the sum of individual contributions to the total energy in the garnet:

$$W_{totatl} = W_C + W_U + W_D \tag{2.1}$$

with, the energy of magnetocrystalline anisotropy that can be described in the form of a series of products of subsequent anisotropy constants K_1 andK_2:

$$W_C = K_1(m_x^2 m_y^2 + m_y^2 m_z^2 + m_z^2 m_x^2) + K_2(m_x^2 m_y^2 m_z^2) + \cdots \tag{2.2}$$

Other components can be treated as additional factors with: uniaxial anisotropy $W_U = K_{u1}(\boldsymbol{M}\boldsymbol{n_u})$ resulting from the strain or the layer growth methodology colinear with n_u direction and the demagnetization energy W_D. The K_{u1} is the first uniaxial anisotropy constant, and $\boldsymbol{M} = M_s(m_x, m_y, m_z)$ is the magnetization vector with saturation magnetization M_s projected with directional cosines on the crystal axis principal <100>-type crystal axis [69, 70].

All the samples investigated in this thesis were cobalt-substituted yttrium iron garnets with the chemical composition $Y_2Ca_1Fe_{5\text{-}x\text{-}y}Co_xGe_yO_{12}$. These samples were fabricated by liquid-phase epitaxy in two series: series I (with non-zero miscut angle of substrates) at Leibniz Institute of Photonic Technology (IPHT) in Jena (Germany) and series II (without miscut) at Centre National de la Recherche Scientifique (CNRS) in Meudon (France)[71]. The doped cobalt ions replaced Fe^{3+} ions in both the tetrahedral and octahedral sublattices. The substantial amount of cobalt doping induced significant changes in the material's properties. Despite its concentration being 40 times lower than that of iron Fe^{3+}, cobalt contributes to strong spin-orbit coupling, significantly increasing by three orders of magnitude the single-ion contribution to magnetic anisotropy. Previously it has been demonstrated that enhancing magnetocrystalline anisotropy in such garnets [72], led to a strong photoinduced magnetic anisotropy [46, 48] and a significant increase in Gilbert damping up to $\alpha = 0.18$–0.22. [73].

All YIG:Co samples tested in this study had similar composition and technical manufacturing parameters, as listed in Table 2.1. However, even minor variations in the growth parameters of the samples had an impact on the observed magnetic properties. For example, a slight reduction in the growth rate led to a smoother surface, resulting in a decrease in the coercive field in the sample.

The significant advantage of the garnet structure is its stability providing a lot of space for the interference in crystal structures by doping various elements ions. For example, tetrahedra sites can be doped with Ga^{3+} or Al^{3+}. Doping of ions with higher valence such as Si^{4+} or Ge^{4+} is also possible but requires an additional addon of Ca^{2+} or Mg^{2+} to provide charge compensation [74]. The introduction of controlled doping and utilization of strain-based growth-induced anisotropy during the crystal growth process allows for engineering garnets with specific characteristics. These characteristics include lattice constant, magnetization, temperature compensation points, and constants of uniaxial and cubic magnetic anisotropy or electrical resistance having an impact on the magnetic, optical, and electrical properties of the material. The doping influence on the first constant of cubic anisotropy is summarized in Table 2.2.

The key magnetic parameters are summarized in Table 2.3.

The temperature dependence has a significant impact on the magnetocrystalline anisotropy of the examined garnets, influencing their magnetization properties. In all the samples, the Curie temperature was 455 K, and no magnetization compensation points

Series	Sample no.	Growth rate [µm/min]	x, Co	y, Ge	Miscut angle	Thickness [µm]
I	705	0.28	0.1	1	4°	7.5
	707	0.25	0.1	1	4°	7.6
II	10	0.27	0.080	0.90	<0.1°	8.0

Table 2.1: Summary of technical properties of investigated samples. Adapted from [71].

ion	site	$\Delta K_1/N$ [cm^{-1}]
Fe^{3+}	tetrahedral	-0.0062
Fe^{3+}	octahedral	0.0056
Co^{3+}	tetrahedral	-0.5
Co^{3+}	octahedral	0
Co^{2+}	tetrahedral	-4
Co^{2+}	octahedral	1

Table 2.2: The contribution to the first constant of cubic magnetic anisotropy, $\Delta K_1/N$ [cm^{-1}] by various single ions for $Y_3Fe_{5-x}M_xO_{12}$garnet localized in different sublattices [68, 72, 75].

Sample no.	705	707	10
Saturation magnetization $4\pi M_s$[G]	90	90	75
Cubic anisotropy constant K_1[erg/cm^3]	-8400	-8000	-5500
Uniaxial anisotropy constant K_{u1} [erg/cm^3]	-2500	-2000	600

Table 2.3: The summary of magnetic parameters of investigated samples at room temperature. [69, 70, 76].

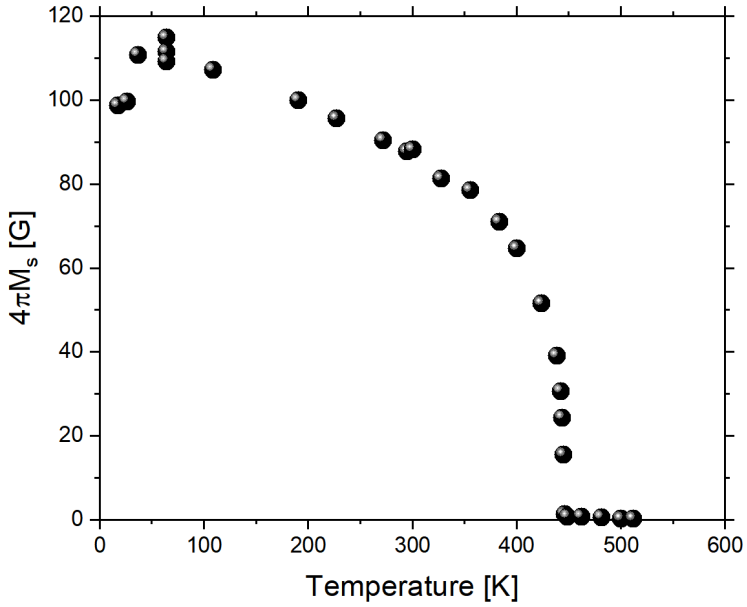

Figure 2.3: Temperature dependence of magnetization saturation for sample no 705. Adapted from [77].

were found. The temperature dependence of saturation magnetization for samples of serie I is depicted in Figure 2.3, showing a broad range between 150-350 K where saturation changes are linear and relatively minor.

Furthermore, temperature variations affect the orientations of the easy magnetization axes and can induce spin-reorientation phase transitions, as illustrated in Figure 2.4. This diagram was typical for both serie of samples. In the temperature range of 160-450 K (region A), four easy magnetization axes along the <111> directions are maintained. Below this range, the magnetization gradually aligns more in-plane, leading to a reduction in out-of-plane magnetization observed in the experiments. Another phase transition occurs within the temperature range of 130-150 K (region B), where the magnetization aligns with two easy axes, namely [110] and [-110]. In the range of 70-120 K (region C), the magnetization aligns with five easy axes, four of which are in-plane, specifically [100], [010], and [001]. Finally, at temperatures between 40-60 K (region D), the magnetization aligns with only the [001] axis [78].

Magnetic garnets exhibit optical transparency across a broad near-infrared range. The absorption coefficient, as depicted in Figure 2.5, demonstrates minimal absorption for wavelengths exceeding >1.3 µm in pure YIG. This transparency extends up to 5 µm and it is restricted in the visible range due to the influence of optical transitions in $Fe3+$ ions and in the infrared range due to phononic absorption (lattice oscillations). Cobalt substitutions have a notable impact on the absorption spectrum, introducing numerous electron transitions [79, 80]. Of particular importance for this thesis is the electron transition in tetrahedral Co^{3+} ions $^5E \rightarrow ^5T_2$ with an energy gap of 1.10 eV, equivalent to 1305 nm, which can be optically excited. Further discussion on the spectroscopy of the investigated garnets can be found in [49].

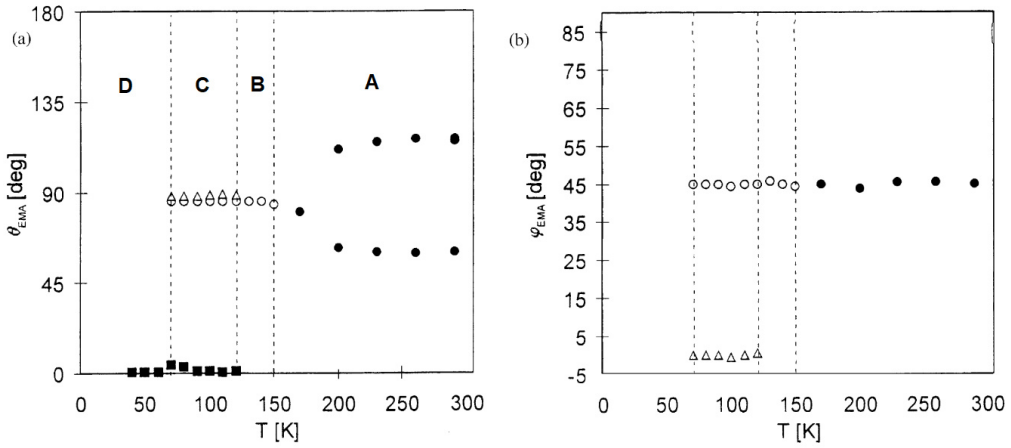

Figure 2.4: The temperature dependence of Easy Magnetization Axes (EMA) orientation in YIG:Co (similar for all investigated samples) for a) polar and b) azimuthal angles of EMA. In the figure, the symbols represent different types of axis alignment: ● - <111>type axis alignment, ○- <110> type axis alignment, △ - <100> type axis alignment, ■ - <001> type axis alignment. Adapted from [78].

Despite absorption, cobalt doping affects also the Faraday rotation. The amount of Faraday rotation is important from an experimental point of view as it allows for probing the magnetization through optical methods thus the domain observation and imaging.

Moreover, the presence of cobalt in YIG:Co gives rise to a strong photo-magnetic effect in both ultrafast and quasi-static regimes [48, 81]. The photomagnetism in YIG:Co is a result of electron transitions enabled by Co^{2+} and Co^{3+} ions replacing Fe^{3+} iin the tetrahedral and octahedral sublattices. These transitions can be optically excited, allowing optical stimuli to address specific transitions and change the valence states of the cobalt ions. This, in turn, can alter the magnetic anisotropy, adding a light-induced and time-dependent component.

Before, research on the photo-magnetic effect in studied YIG:Co samples has been conducted in both quasi-static [46, 81] and ultrafast regimes [9, 48–51, 53, 69, 83, 84]. The quasi-static regime involves constant light illumination, which provides access to only relatively low light intensities.

On the other hand, the use of ultrashort femtosecond pulses has revealed a completely different excitation mechanism that grants access to the ultrafast regime. In YIG:Co, it has been demonstrated that resonant excitation of the $d - d$ transition in Co ions can effectively change their orbital states, thus strongly affecting magnetic anisotropy. This excitation, in particular, disrupts the balance between intrinsic cubic magneto-crystalline anisotropy and the extrinsic magnetic anisotropy promoted by the Co ions. The effective fields of the photo-induced magnetic anisotropy have proven to be strong enough to permanently switch the magnetization to another bit state determined by the polarization of the laser pulse [9].

2.3 MAGNETIC DOMAIN STRUCTURES AND MAGNETIZATION REVERSAL

In investigated YIG:Co the dominant anisotropy component is negative cubic magnetocrystalline anisotropy, which prevails over the smaller, growth-induced uniaxial anisotropy. Consequently, in the absence of an external magnetic field, the garnet's domain structure

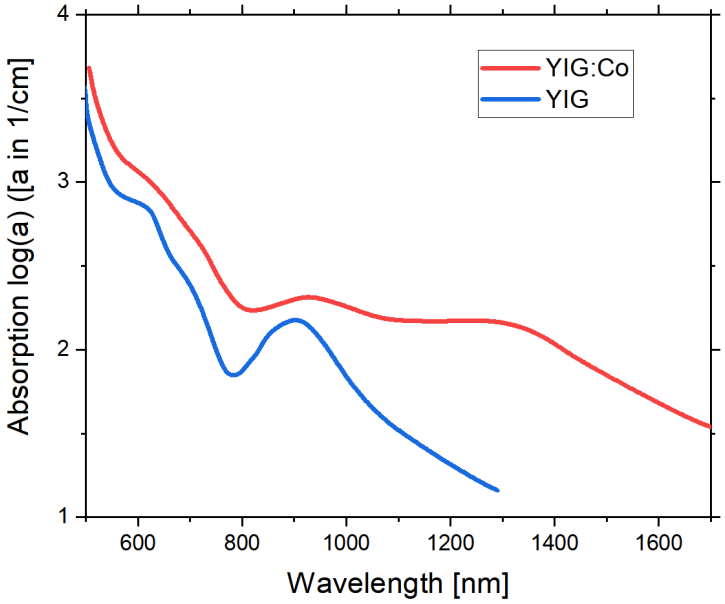

Figure 2.5: The absorption coefficient in YIG:Co with $Y_2Ca_1Fe_{3.9}Co_{0.1}Ge_1O_{12}$ composition, pure YIG with $Y_3Fe_5O_{12}$. Optical absorption at 1300 nm for the 7.5 µm thick sample equals 12 %. Adapted from [82].

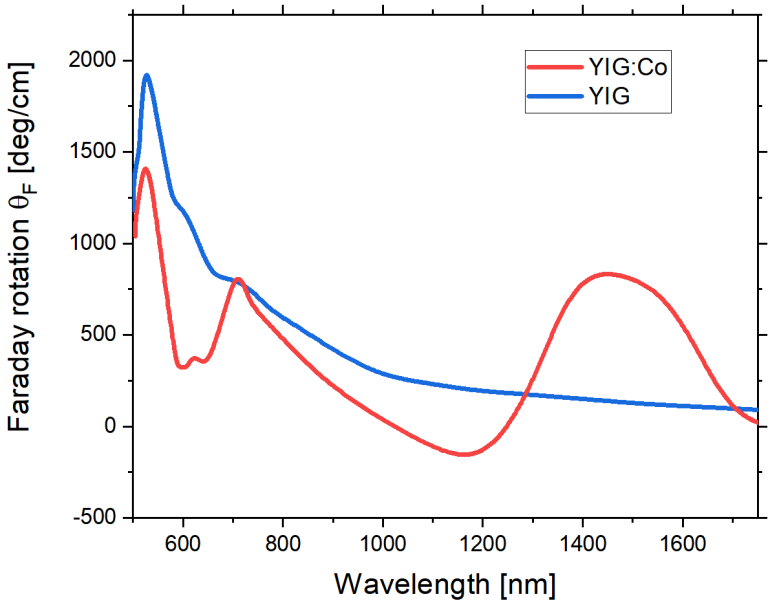

Figure 2.6: The spectral dependence of the Faraday rotation in YIG:Co and YIG samples. Adapted from [82].

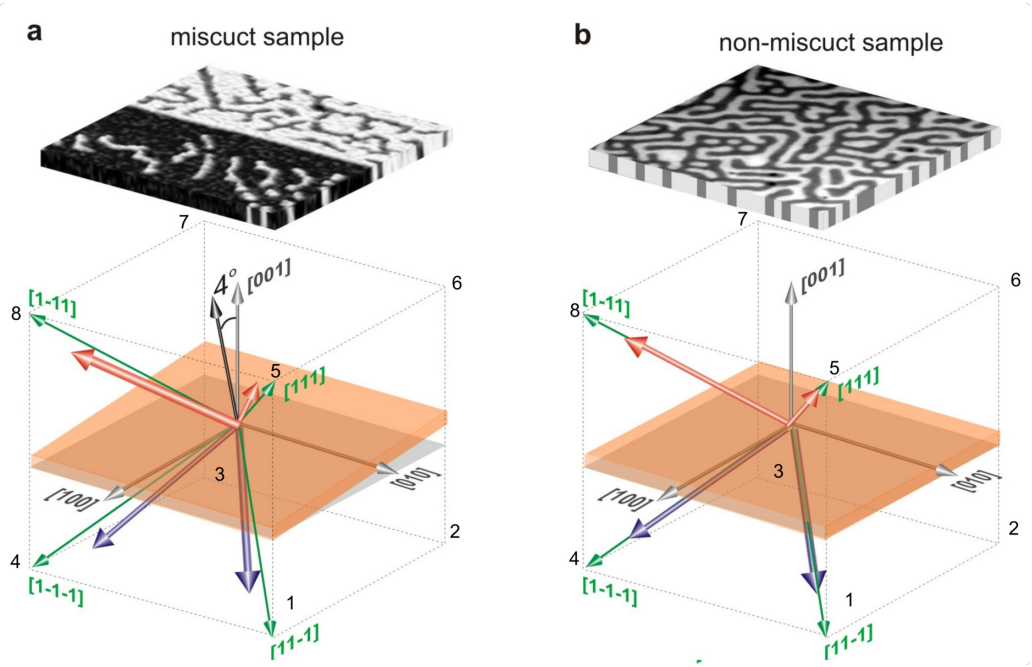

Figure 2.7: The magnetization directions and the domain structure observed in Faraday geometry in the YIG:Co a) with miscut and b) with pure cubic symmetry. In the case of non-miscut samples, domains cover equivalent volumes.

possesses both out-of-plane and in-plane magnetization components. This leads to the existence of four different domain states at each cube's vertex, giving rise to a complex domain pattern [77].

To distinguish between these domain states and make the domain structure more visible in a polarizing microscope, a 4° miscut was introduced. The diagram presenting all possible domain states is shown in Figure 2.7. This miscut partially breaks the degeneracy between the states, causing the magnetic domains to cover non-equivalent volumes. The domain states are labeled as large domains (1) M(L)- and (8) M(L)+ or small domains (4) M(s)- and (5) M(s)+. The large domains correspond to magnetizations close to the [11-1] and [1-11] directions, while the small, labyrinth-like domain states correspond to [1-1-1] and [111], respectively. Although the magneto-optical contrast between the small (4 or 5) and large (1 or 8) states is almost identical, their different spatial distribution makes them distinguishable.

When the miscut is eliminated, resulting in pure cubic symmetry within the sample, the domain structure changes. In this configuration, easy magnetization axes align directly along the cube's main diagonal. Compared to the miscut geometry, the domain structure obtained in magneto-optical microscopy is balanced, with magnetic domains covering equivalent volumes and forming a uniformly distributed labyrinth pattern. Consequently, all eight possible magnetization orientations become energetically equivalent, with no preference for any direction of magnetization within the cube.

The domain structure and magnetization reversal in examined YIG:Co samples have been extensively studied [49, 73, 77]. The hysteresis loop for in-plane and out-of-plane magnetization reversal are summarized in Figure 2.8 and Figure 2.9 respectively. The paramagnetic contribution from the GGG substrate was subtracted from the presented curves.

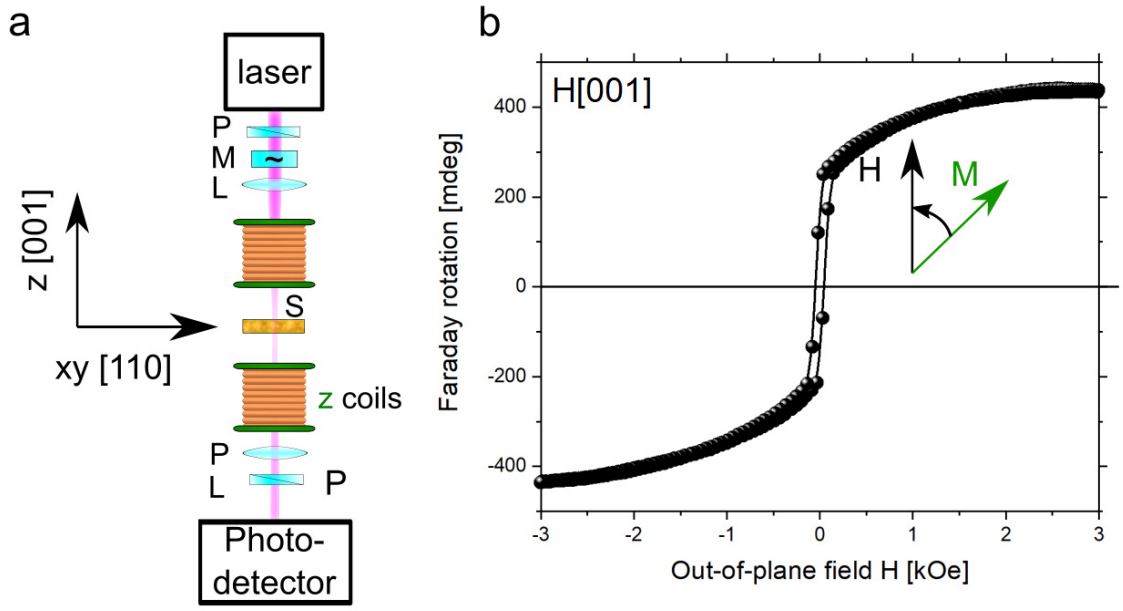

Figure 2.8: Magnetization reversal in examined YIG:Co triggered by an applied external magnetic field in out-of-plane configuration a) The experimental setup describing the geometry used with the following markings: P - Polarizer, M - Modulator, L - Lens, S – Sample. b) The shape of hysteresis loop in the out-of-plane configuration typical for all investigated samples.

The magnitude of the magnetization vector remains constant, while the vector undergoes coherent rotation in response to the effective anisotropy field. The introduction of an external magnetic field contributes an additional component to the effective field. When the external field is comparable in strength to the anisotropy field, the magnetization aligns itself with the external field, resulting in a modification of Faraday rotation, ultimately reaching a saturation value of approximately 0.4°.

The absence of a miscut angle in the samples does not significantly impact the shape of the hysteresis loops. The hysteresis characteristics for all samples remain identical, as represented in Figure 2.9 and Figure 2.8, with variations primarily arising from differences in anisotropy constants.

In the case of in-plane geometry, in the absence of an external field, one can observe the coexistence of domain states up to approximately 0.4 kOe. A further increase in the field value selects a particular magnetization state, defining the effective anisotropy field H_A. For even greater external field values, Magnetization aligns with the field direction at around 2 kOe. The goniometric dependence on the applied in-plane field is illustrated in Figure 2.9e, highlighting the presence and direction of easy magnetization axes of <111> type.

Even for the non-miscut YIG:Co samples, all states can be visualized without applying an external magnetic field. As shown in Figure 2.9c, tilting the sample toward the illuminating light combines both the out-of-plane and in-plane components, contributing to the magnetization projection on the light vector. This reveals all magnetization states simultaneously, confirming their coexistence.

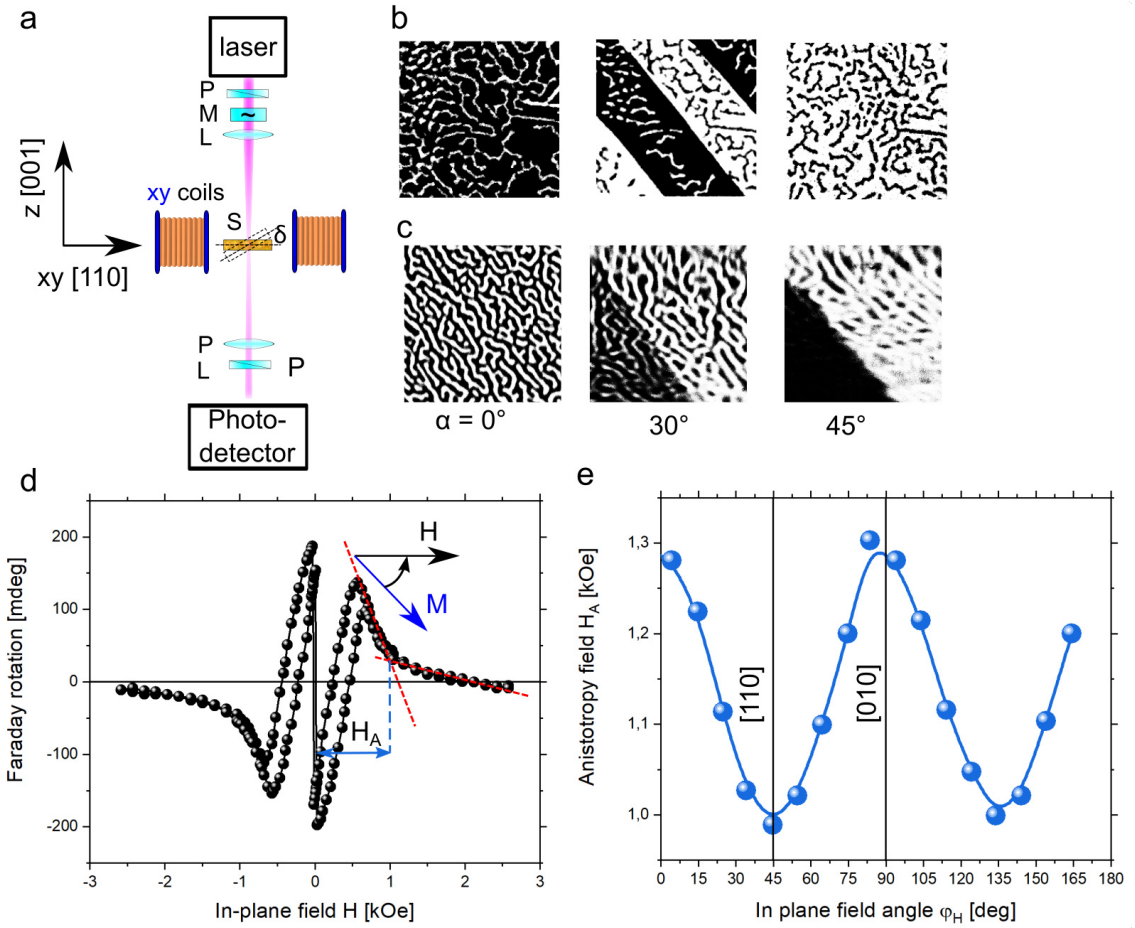

Figure 2.9: Magnetization reversal in examined YIG:Co triggered by an applied external magnetic field in-plane configuration. a) The experimental setup describing the geometry used with the following markings: P - Polarizer, M - Modulator, L - Lens, S – Sample. b) The magnetic domain pattern showing the presence of all domain states in samples with a miscut. The mixed pattern with characteristic state boundaries is obtainable using an in-plane magnetic field sequence, initially aligned with the [110] direction and subsequently with the [1-10] direction. c) Observation of all four domain states in the non-miscut sample using the Faraday geometry (as discussed in Chapter 3). The sample is tilted from the plane normal by a marked angle δ. The projection of the magnetization over the light k vector reveals the presence of all four magnetization states, analogous to the miscut case. d) In-plane configuration, aligned with the [110] crystal axis. e) The anisotropy field (H_A) saturating the domains as a function of the applied angle between [100] and [010] axes, determining the localization of the easy axes.

3

EXPERIMENTAL METHODS

The topics discussed in this thesis are focused on magneto-optical experiments. While Magneto-Optical (MO) microscopy ensures sufficient spatial resolution, down to the optics capabilities and diffraction limits, its greatest advantage is temporal resolution. The use of the principle of the pump and probe method gives an unprecedented temporal resolution of even single femtoseconds. This makes the pump and probe technique an indispensable and widely used tool in the study of ultrafast magnetism. Since most of the performed measurements were based on MO microscopy in the transmissive geometry the main emphasis will be placed on the description of the Farraday effect.

In this chapter, we will describe the fundamental magneto-optical Faraday effect with imaging of magnetic domain structures. Next, starting with the ultrashort laser pulses we will introduce the time-resolved pump and probe spectroscopy. Finally, we will describe in detail the multi-functional experimental system designed and built myself at the Laboratory of Femtosecond Spectroscopy in the Faculty of Physics University of Bialystok allowing for both static MO microscopy, as well as time-resolved spectroscopy with spatial (<400 nm) and temporal (<8 fs) resolution, within single or double pump excitation multi-color schemes.

Sections concerning the experimental setups were partially published in:

Zalewski, T. & Stupakiewicz, A. "Single-shot imaging of ultrafast all-optical magnetization dynamics with a spatiotemporal resolution", *Rev. Sci. Instrum.* 92, 103004 (2021).

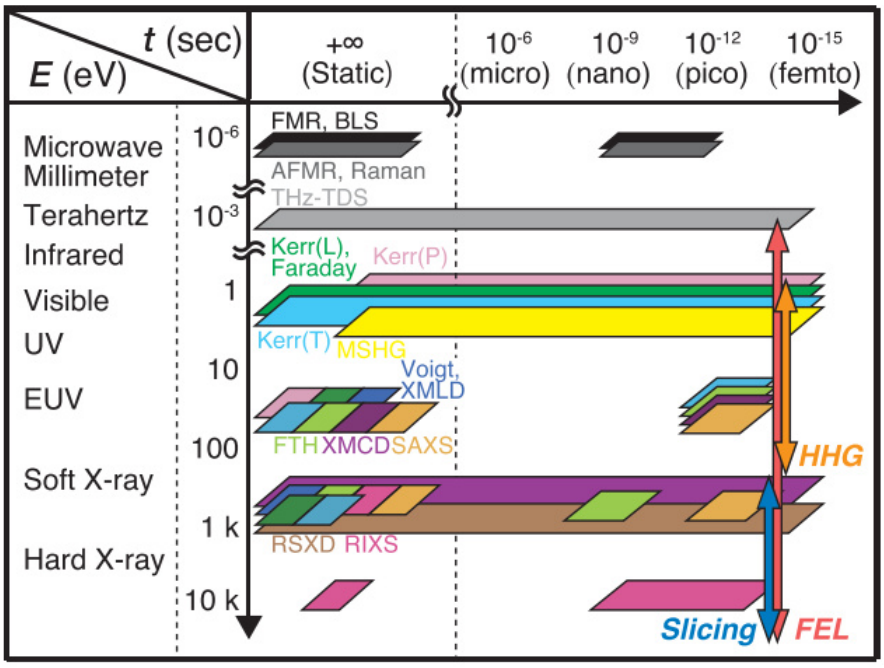

Figure 3.1: Overview of experimental techniques used for tracing the magnetization dynamics with respect to the energy and the timescale. The presented methods are based on using electromagnetic-wave within the photon-in and photon-out scheme. Adapted from [86].

3.1 INTRODUCTION TO EXPERIMENTAL TECHNIQUES

The field of physics inseparably combines theory with experiment. While theory tries to describe the world around us in a mathematical sense, the experiment gives a direct understanding of the intricate behavior and structure of matter. Solid-state physics incorporates countless experimental techniques of which many are used for the magnetic characterization of the material.

One common starting point is conventional magnetometry, which provides macroscopic information about a material's bulk magnetic properties. Another broad branch of studies can be devoted to the interaction of the material with the incident electromagnetic wave. Examined material while being subjected to a static magnetic field, can absorb the energy from the electromagnetic wave tuned to the appropriate frequency which results in a phenomenon known as magnetic resonance.

The field of physics inseparably combines theory with experiment. While theory tries to describe the world around us in a mathematical sense, the experiment gives a direct understanding of the intricate behavior and structure of matter. Solid-state physics incorporates countless experimental techniques of which many are used for the magnetic characterization of the material.

This leads to various specialized experimental techniques, each tailored to different types of magnetic moments involved in the resonance. Notable examples include nuclear magnetic resonance (NMR), electron paramagnetic resonance (EPR), Ferromagnetic Resonance (FMR), Mössbauer spectroscopy, and muon spin rotation (μSR) [85].

However, the interaction between electromagnetic waves and materials goes beyond resonance-based methods, yielding another set of experimental MO techniques. As shown

in Figure 3.1 using electromagnetic waves is not only limited to the optical spectrum. Free electron lasers (FEL) and high harmonic generation (HHG) lasers ensure a variety of different wavelengths and thus energies, ranging from microwaves, through the optical spectrum, up to soft and hard X-rays, give access to the whole range of optical transitions. The addition of pulsed beams opens up an insight into a temporal domain that can probe timescales ranging from static ($+\infty$ - single seconds range) up to ultrafast dynamics (femtosecond range), giving access to different magnetic interactions Figure 1.1.

The versatility and adaptability of laser-based MO techniques, employing MO effects such as the Faraday or Kerr effect, make them invaluable for investigating magnetic properties in various materials. Furthermore, modern femtosecond lasers, which are often compact and reliable, can be used without the need for large and complex facilities. By utilizing nonlinear interactions and optical parametric amplifiers, a wide range of wavelengths, from ultraviolet to near-infrared, becomes accessible. This opens up a plethora of experimental possibilities for spectroscopy with access to the temporal and spatial resolution.

3.2 MAGNETO-OPTICAL FARADAY EFFECT

The rapid development of physics is inseparably connected with the attempt to unify theories combining interactions of various natures. In the early 19th century, magnetism, electricity, and optics were three separate branches of science studied in separate experiments, while the interaction between light and matter was an unexplained phenomenon. The breakthrough began in 1820 with the work of Ørsted, who observed that the compass needle can be deflected from magnetic north by an electric current located in a wire nearby. The experiment revealed an inseparable relationship between electricity and magnetism laying the foundations for the theory of electromagnetism.

The British scientist Michael Faraday was exceptionally aware of the phenomenon of electromagnetism. Firstly, he expanded it by discovering electromagnetic induction. Next, he correctly sensed that light also obeys the laws of electromagnetism. To prove his point, he tried to look for the influence of electric and magnetic forces on light passing through the transparent material under study. In his research, he used polarized light rays, well-known and previously described in the works of Maulus, Fresnel, and Brewster on polarization and birefringence. Various materials, while being appropriately oriented can modify the light's polarization plane.

On 13 September 1845, Faraday experimented with rays of light passed through a polished lead silica borate glass which led to the discovery of the magneto-optical effect named after him [87]. His research was remarkably well documented in his diaries, which he kept continuously for over 40 years. He noticed that *„when contrary magnetic poles were on the same side, there was an effect produced on the polarized ray"* [88]. The applied magnetic force can rotate the plane of polarization of the incident light beam. The angle of rotation is proportional to the strength of the magnetic force.

The effect discovered by Michel Faraday became the first evidence linking light to electromagnetism. In the near future, this result enabled James Clerk Maxwell to unify the theory of electromagnetism. The electro-optical effect, which Farraday began unsuccessfully searching for, was discovered 30 years later by John Kerr. The same Scottish scientist described an effect operating in reflective geometry, called the Magneto-Optical Kerr Effect (MOKE), analogous to the transmissive Faraday effect [89].

A phenomenon similar to the Faraday Effect and having the same origin was demonstrated in 1877 by John Kerr. He noticed that light polarization can be modified not only in a transparent magnetic material but also in the reflective case of a polished magnetized mirror. The presence of the magnetic field and magnetic anisotropy manifests itself also in the reflective case, with a light penetration depth of dozen nanometers only. This facilitates experimental studies on non-transparent metallic ferromagnets, making MOKE a universal and commonly used experimental technique.

The Faraday effect and MOKE have the same microscopical origin - spin-orbit coupling. Because only the first-order term of interaction contributes to the effects both are so-called linear - they depend linearly on magnetization ($\sim M$). Macroscopically, each of them is observed as magnetic circular birefringence. Circular birefringence can be understood as a phenomenon in which a material is optically anisotropic, i.e. having two refractive indices for left-handed Δn_L and right-handed light Δn_R polarizations with a nonzero difference between them $\Delta n \neq 0$. However, the index of refraction written in the form of a complex number $n = n + i\kappa$ contains a coefficient associated with the absorption κ. The anisotropy of the absorption, or in other words the case in which $\Delta\kappa \neq 0$, for two circular light polarizations gives another linear effect called magnetic circular dichroism MCD.

In most cases, the use of MO as an experimental tool is based on linear effects using wavelengths in the visible spectrum. However, it is worth noting the existence of higher-order effects that depend non-linearly on magnetization and also can contribute to the signal. These types of quadratic effects ($\sim M^2$), involving a second-degree term, are usually noticeably weaker. By analogy with the effects listed above, one can distinguish a magnetic linear birefringence (Magneto-optical Voigt effect) and magnetic linear dichroism (MLD).

The phenomenon described by Faraday showed the interaction between matter placed in a magnetic field and a polarized electromagnetic wave passing through it. An external magnetic field H_z acting on isotropic diamagnetic samples causes an arising of magnetization M_z proportional to the susceptibility of the material χ. However, in materials ordered magnetically (ferro- and ferrimagnets) as well as in materials that are transparent enough and at the same time provide a large Faraday rotation such as magnetic garnets, the effect can be observed without any external magnetic field. Therefore, the effect depends on the internal magnetization in the sample, making the MO methods an excellent tool for studying the magnetic structure of materials, extensively used in this work.

Two fundamental types of geometry can be distinguished for magneto-optical effects. The Faraday geometry in which light propagates longitudinally (z-axis index), thus in the magnetic field direction $\vec{k} \| \vec{B}$, and the Voigt geometry where the light propagated transversely to the field $\vec{k} \perp \vec{B}$. The schematic concept of the Faraday effect is shown in Figure 3.2.

A linearly polarized light beam can be considered as a superposition of two identical circularly polarized beams with left-handed and right-handed polarizations and a defined phase difference. In a transparent material, the magnetic field induces circular birefringence, creating complex refractive indices with n_L and n_R for the right-handed and left-handed polarized light beams. This leads to different phase velocities, or, in other words, different propagation speeds for each light helicity, resulting in an additional relative phase shift. In the case of a superposed linearly polarized beam, this effect manifests as a rotation of the beam's plane by an angle θ_F.

The angle of Faraday rotation can be expressed as:

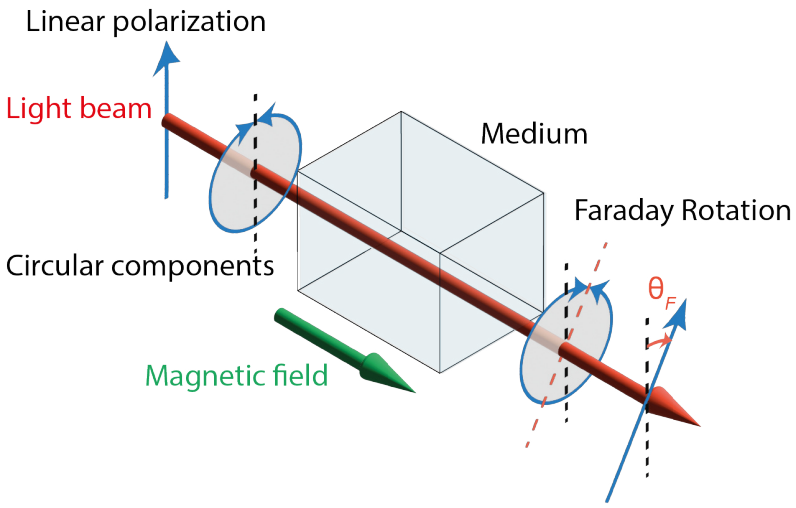

Figure 3.2: The conceptual idea of Faraday magneto-optical effect. Linearly polarized light superposed from right and left circular components of polarization, which propagates through a magnetic medium with different velocities undergoes phase difference resulting in rotation of the polarization plane.

$$\theta_F = V(\omega)dB \tag{3.1}$$

Where d is the sample thickness, B is an inducted magnetic field and $V(\omega)$ is the Verdet constant, strongly dependent on the photon energy.

In normal geometry, only the out-of-plane component of magnetization in the medium affects the light. The rotation effect is directly proportional to the projection of the beam's wave vector onto the magnetic field vector. Consequently, by twisting the orientation of the medium plane relative to the light beam, it becomes feasible to detect a combination of both in-plane and out-of-plane magnetization components in the medium.

The direction of the rotation depends on the sign of the magnetic field. Therefore, the rotation angle is doubled to $2\theta_F$ when the light beam passes through the material and is reflected back passing the material in the opposite direction. For a positive Verdet constant, the plane of polarization is rotated clockwise for a wave vector $\vec{k}$ parallel and anti-parallel to the magnetic field $\vec{B}$. This directionality phenomenologically distinguishes the Faraday effect from normal optical activity. This property of allowing signals to propagate in one direction while blocking reverse propagation is applicable as a working principle for non-reciprocal magneto-optical components such as optical isolators [90].

The ideal rotation of the polarization plane for linearly polarized light interacting with magnetized materials occurs when the amplitudes of its components remain unchanged. The alteration in the amplitude ratio, caused by circular dichroism, introduces ellipticity denoted as η into the light beam. Through a more complex analysis of the beam properties, different magnetization components can be extracted.

3.3 MAGNETO-OPTICAL IMAGING

The use of interactions between light and matter in the form of magneto-optical effects makes it possible to obtain many useful tools for the study of magnetization. The setup geometry, defining the relative position between light and magnetization in the material,

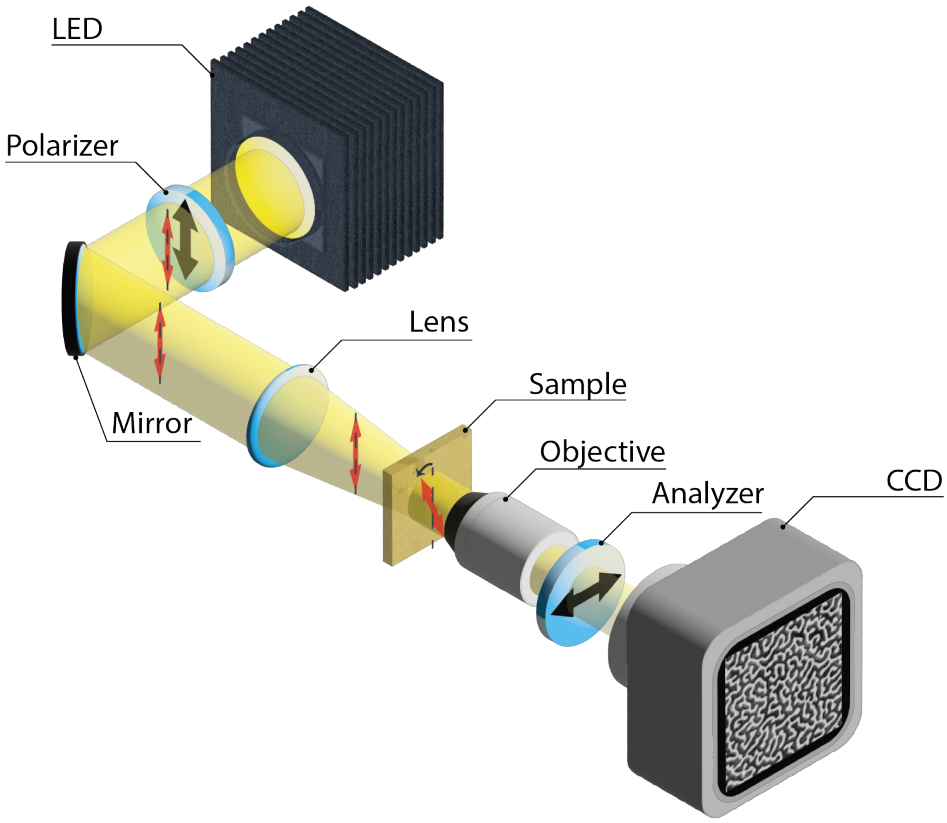

Figure 3.3: The scheme of the MO Faraday microscopy setup. The polarized white Light-Emitting Diode (LED) light is used to illuminate the sample. The local magnetization in a material affects the polarization plane of transmitted light rotating it. The cross-polarizer (analyzer), converts the polarization changes into the intensity changes visible on theCharge-Coupled Device (CCD) camera in form of magnetic domain structure.

allows for selective probing of individual magnetization contributions in out-of-plane or in-plane configurations. Another significant advantage associated with the use of light is the possibility of imaging, providing spatial resolution resulting in magneto-optical (MO) microscopy.However, unlike classical optical microscopy, the image is formed not by sensitivity to the changes in light intensity, but by its polarization. This form of imaging is a well-established laboratory technique, which is typically based on linear MO effects, that is discussed earlier Farraday effect in transmission, and the Kerr effect in reflection using wavelengths in the visible spectra.

The example scheme of the transmissive MO microscopy application allowing visualization of the domain structure is presented in Figure 3.3. The light from the white LED source is transmitted through the polarizer ensuring the linear polarization plane in the desired direction. Next, polarized light is focused on the magnetic sample in which the polarization plane is rotated via the Farraday effect by an θ_F angle. The objective captures the transmitted light and ensures the desired level of magnification. crossed analyzer, rotated to the polarizer by the angle α_{nl} transform polarization rotation into intensity change, which finally can be detected by the CCD camera. Light with an initial intensity I_0, while passing through each of the components undergoes the Maulus law, which can be briefly expressed as $I = \frac{1}{2} I_0 cos^2(\alpha_{nl} + \theta_F)$. In this configuration, measured intensity corresponds to the M_z out-of-plane magnetization component along $\boldsymbol{k}$-vector. For magnetic domains with $+M_z$ and $-M_z$ component the Faraday rotation angle has

an opposite sign, giving $+\theta_F$ and $-\theta_F$ rotations allowing for visualization of magnetic structure in the sample.

Every polarization modulation technique can be comprehensively presented using Jones matrix formalism. In this method, every component in the MO microscope inducing any kind of polarization rotation or ellipticity can be expressed by the corresponding matrix [91]. In a such formalism, an incident probe light can be noted as an electric field vector E_{in} where $E_x$and E_y are complex vertical and horizontal components of the field.

$$E_{in} = \begin{bmatrix} E_x \\ E_y \end{bmatrix} \tag{3.2}$$

Assuming that the polarization axis is set for the vertical x-axis the matrix corresponding to the polarizer can be noted as:

$$P = \begin{bmatrix} 1 & 0 \\ 0 & 0 \end{bmatrix} \tag{3.3}$$

The sample with the polarization changes induced by the Farraday rotation θ_F and the change in ellipticity η is expressed by:

$$S = \begin{bmatrix} \cos\theta_F + i\eta\sin\theta_F & -\sin\theta_F + i\eta\cos\theta_F \\ \sin\theta_F - i\eta\cos\theta_F & \cos\theta_F + i\eta\sin\theta_F \end{bmatrix} \tag{3.4}$$

Moreover, components that can contribute to the parasitic Faraday rotation ϕ, typically caused by the glass lens in the objective subjected to the external magnetic field [92] can be expressed as:

$$F = \begin{bmatrix} \cos\phi & -\sin\phi \\ \sin\phi & \cos\phi \end{bmatrix} \tag{3.5}$$

And finally, the analyzer with transmission axis rotated by α_{nl} angle with respect to the initial polarization plane:

$$A = \begin{bmatrix} \cos^2\alpha_{nl} & \cos\alpha_{nl}\sin\alpha_{nl} \\ \cos\alpha_{nl}\sin\alpha_{nl} & \sin^2\alpha_{nl} \end{bmatrix} \tag{3.6}$$

The modified output electric signal E_{out} illuminating CCD camera can be calculated just by multiplying all matrix components:

$$E_{out} = AFSPE_{in} \tag{3.7}$$

In this form, any other components, which affect the polarization state of the light, can be added. Typically, such components can include quarter or half wave plates, which are often used for generating circularly polarized light, or to rotate the linearly polarized light plane respectively. As the camera is sensitive to the light intensity, the intensity

modulation from the initial one I_0 up to the signal detected by the camera, I can be calculated as:

$$I = |E_{out}|^2 = I_0[(1-\eta^2)\sin^2(\alpha_{nl} + \theta_F + \phi) + \eta^2 \tag{3.8}$$

Assuming a small-angle approximation simplifying squared sine function to a quadratic one, the final result can be expressed as[93]:

$$I(\alpha_{nl}, \theta_F, \phi) \approx I_0^{'}(\alpha_{nl} + \theta_F + \phi)^2 + I_\epsilon \tag{3.9}$$

Here, the I_ϵ is an ellipticity-dependent offset. For the case with no external magnetic field, the parasitic angle can be neglected $\phi = 0$. This result shows the relationship between the magnetization in the sample expressed by the faraday angle and the intensity observed on the camera.

On the other hand, while the intensity also depends on the angle of the analyzer α_{nl}, to obtain the absolute angles of Faraday rotation θ_F, the appropriate position of the analyzer must be considered. This is particularly important in the case of studying the dynamics of magnetization, in which the transitional state between the magnetization with out-of-plane component $+M_z$ and $-M_z$ is represented and expressed by changes in intensity. To accurately determine it, it is necessary to scan the imaged intensity for different positions of the analyzer α_{nl}. This procedure should be performed for the averaged intensity in the domains with opposite out-of-plane magnetization directions $+M_z$ and $-M_z$ resulting for each of them in quadratic functions defining in the parabola minimum the sample-specific Faraday rotation [92]. Moreover, by performing another scan for a demagnetized sample without an out-of-plane magnetization component, a third parabolic function can be found that precisely defines the analyzer angle $\alpha_{nl} = 0$ at its minimum

Discussed methods can be also used to find an analyzer position resulting in maximum contrast $C(\alpha_{nl})$ corresponding to the highest signal-to-noise ratio in imagining.

$$C(\alpha_{nl}) \backsim \frac{I(M_{z+}) - I(M_{z-})}{I(M_{z+}) + I(M_{z-})} \tag{3.10}$$

This formalism can be applied for the plane LED white light as well as for the short, laser probe pulses.

3.4 ULTRAFAST TIME-RESOLVED MEASUREMENTS TECHNIQUES

The use of MO imaging can give an answer regarding the local magnetization in the sample. However, direct imaging applies mainly to the static or equilibrium case. Investigating the dynamical case requires experimental tools responsive to the adequate timescale for the studied system. For slower phenomena, such as domain wall motion Figure 3.1, ranging from micro to nanoseconds, electronic measuring devices have a sufficiently high temporal resolution to handle the measurements. All faster interactions, from spin precession up to the exchange interaction, are entirely beyond the capabilities of electronic devices. Shorter timescales and the transition from nanoseconds to pico and even femtoseconds require other measurement techniques. These time scales must be probed with ultrashort pulses, which can only be achieved with ultrafast pulsed lasers.

Nowadays, there is a huge variety of applications for lasers generating ultra-short pulses. Different types of lasers such as solid-state lasers, fiber lasers, or semiconductor lasers find their use with a dedicated design in various fields including material processing, medicine, laser microscopy, and measurements, or telecommunication. Modern, commercially available scientific lasers are capable of achieving pulse durations of almost several femtoseconds. These are the shortest tabletop and controlled stimuli available to humans. In addition to extreme temporal properties, even a small optical average power contained in such a short pulse leads to huge, unattainable anywhere else peak powers of billions of watts These advantages make ultrafast lasers a complex tool that can provide insights into the scientific frontiers of fundamental interactions not otherwise available.

The development and increasing availability of ultrafast lasers and time-resolved techniques has made it possible to achieve a breakthrough in many fields of science. Chemistry in particular with the whole new field of femtochemistry has applied these techniques with great success. The use of femtosecond pulses of laser light gave access to ultra-short time scales, enabling time-resolved observation of the process of a chemical reaction and rearrangement of particles. This achievement was recognized by the Nobel Committee, which in 1999 awarded the Nobel Prize in Chemistry to the research of Ahmed Zewail "*for his studies of the transition states of chemical reactions using femtosecond spectroscopy*" [94]. Moreover, the half of the Nobel prize in 2018 was awarded jointly to Gérard Mourou and Donna Strickland "*for their method of generating high-intensity, ultrashort optical pulses*" [95]. The rank of the award received for their work on chirped pulse amplification shows how widely appreciated by the scientific community has been the possibility of using ultrashort pulses, in particular in tabletop systems.

For the magnetic community, these tools provided unprecedented insights into ultrafast spin dynamics. The exceptionally strict time resolution down to femtoseconds offers access to information inaccessible in slow, static, or quasi-static regime experiments. Employing a single optical ultrashort stimulus (pump) can initiate the light-induced motion of magnetization. However, there are no typical detectors responsive enough to track such a rapid phenomenon. Therefore, to detect the light-induced change, the temporarily delayed portion of the same triggering optical pulse is used (probe). A precise time delay is introduced by extending the optical path of the probing pulse by a well-defined distance. Virtually all studies of the ultrafast dynamics of laser-induced magnetization exploit this pump and probe principle or a variation of this method [11].

3.4.1 *Femtosecond laser systems*

Lasers have developed rapidly since their birth in 1960 [96]. Already after thirty years in the early 1990s, the discovery of the self-locking Ti:sapphire laser led to the generation of femtosecond pulses with solid-state lasers [97].The word laser is an acronym for light amplification by stimulated emission of radiation. The extension of this commonly used abbreviation includes information about the process that makes the device work - stimulated emission leading to optical amplification. It can be stressed that unlike most phenomena studied in physics, which derive directly from observations of nature, stimulated emission was first predicted and postulated theoretically. It was not observed in nature in any form before the successful confirmation of the theory in a working device.

The basic distinction of lasers is between those operating in the Continuous Wave (CW) mode and those operating in the pulsed regime. Pulse lasers generate optical power with

a specific duration and repetition rate, producing bursts of optical energy instead of a continuous beam. The shortest pulses can be obtained by using a technique called mode-locking. As in a typical laser, to amplify the light, it is necessary to use the active gain medium stimulated by an external energy source in a process called pumping. Moreover, to obtain self-excitation conditions it is necessary to ensure positive feedback. Therefore the beam is enclosed in a resonator, which typically is constructed with a pair of mirrors of length L. The cavity round-trip time T_{RT} is defined by the length of the resonator, its refractive index $n_c$which can be simplified to one, and the speed of light c.

$$T_{RT} = \frac{n_c 2L}{c} \tag{3.11}$$

Unlike CW lasers, where the energy is spatially equalized within the cavity, pulse lasers confine the energy into a spatially small region that propagates back and forth between the mirrors accumulating energy. Pulse can be passed out through the output coupler only at regular intervals, which corresponds to the transit time T_{RT} of the pulse within the cavity. The lasing conditions are defined by a few factors. The emission profile of the active medium and spectral profile of the cavity specifies the gain curve and the losses line. Moreover, the oscillations in the cavity for each transverse mode are permitted only at discrete frequencies ν_n, known as longitudinal modes. For the lowest transverse mode, the corresponding set of the longitudinal, standing wave mods consists of the regularly spaced frequency comb of mods separated by a frequency $\delta\nu$.

$$\delta\nu = \nu_{n+1} - \nu_n = \frac{1}{T_{RT}}. \tag{3.12}$$

Mods only allowed by this condition, enclosed in the gain curve and exceeding the loss profile can last and provide lasing [98]. This multi-mode oscillation of N mods of electric field $E(t)$ in a fixed point of space can be expressed as:

$$E(t) = \sum_{n=0}^{N-1} E_n \sin(2\pi(\nu_0 + n\delta\nu)t + \varphi_n(t)) \tag{3.13}$$

In which the ν_0 is the fundamental or lowest frequency lasing mode and $\varphi_n(t)$ is the phase of n-th mode. In a conventional laser cavity, multiple longitudinal modes with slightly different frequencies oscillate simultaneously, but each mode has its unique phase relationship with the others, thus $\varphi_n(t)$ changes randomly. This results in random interference between separate modes averaging the electric field. Synchronizing mods by fixing the varying phase difference in time to φ_n provides the condition mode-locking. In real laser systems, the synchronization of phases is accomplished by introducing a periodic modulation of loss or gain inside the laser cavity. This modulation, which can be active or passive, is carefully designed to match the round-trip time T_{RT} of the cavity, enabling effective mode-locking. The example of mode synchronization for $n = 4$ electric field mods is presented in Figure 3.4. The interference of all light components leads to the generation of short pulses with high peak power. As the number of modes increases the pulses are getting shorter. The Full Width at Half Maximum (FWHM) of the output pulse duration is approximately equivalent to the inverse bandwidth gain $t_{FWHM} \approx \frac{1}{N\delta\nu}$. Moreover, with increasing the number of mods peak power increases quadratically. Lasers

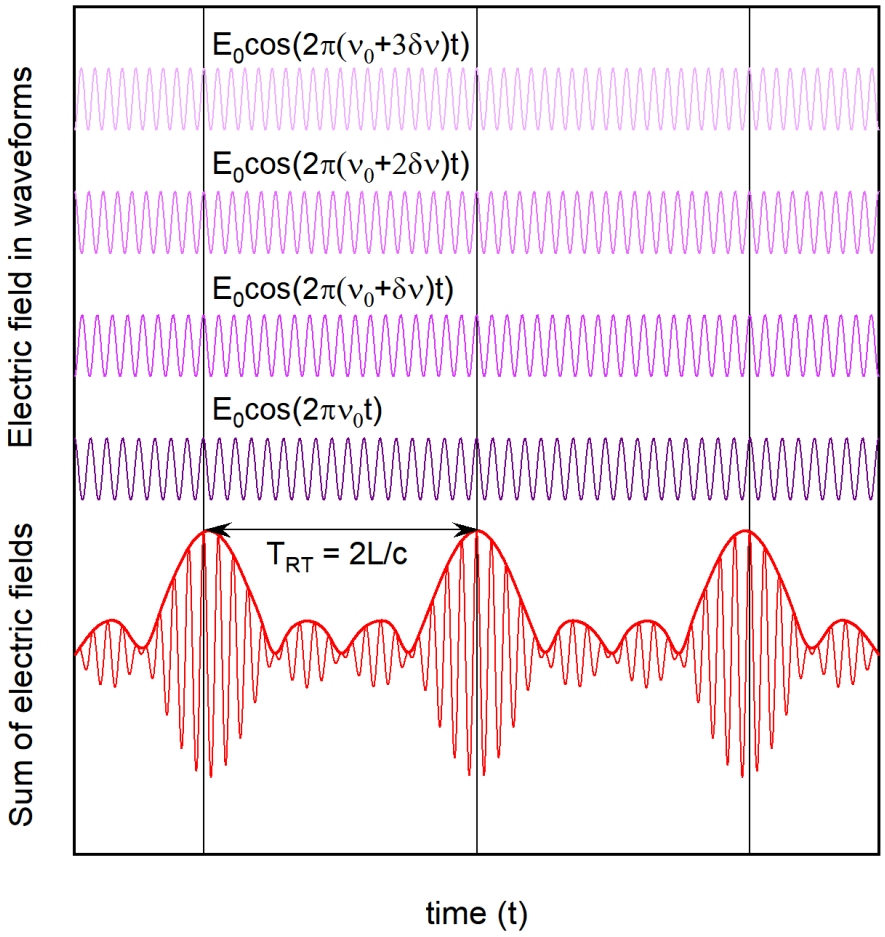

Figure 3.4: The examplar mode synchronization presented as the superposition of $n = 4$ electric field individual waveforms with equal amplitude, differing in frequency by a small constant $\delta\nu$ factor. The fixed phase difference locks laser modes leading to the creation of repeatable with a T_{RT} period pulses. The final output power is proportional to the square of the sum of electric fields.

used for generating pulses with durations below 10 fs typically exhibit a high number of lasing modes, numbering in the millions.

Any pulses generated from the composition of waves with different frequencies can be treated as a wave packet. Using Fourier formalism the complex form of the electric field of the ultrashort pulse can be decomposed into a set of monochromatic waves. The Fourier transform links the temporal domain of the pulse with its frequency spectrum domain.

$$\tilde{E}(\omega) = \mathscr{F}\{E(t)\} \tag{3.14}$$

And otherwise in the case of the inverse Fourier Transform.

$$E(t) = \mathscr{F}^{-1}\{\tilde{E}(\omega)\} \tag{3.15}$$

For instance, a constant function and a Dirac delta function form a Fourier-Transform pair. This means that a temporally constant beam, such as the one generated in an ideal CW laser, has a spectrum consisting of a single frequency. Conversely, to generate an ultra-short pulse, represented by a temporal Dirac delta function, the beam must have a spectrum that spans a wide range of frequencies. According to the uncertainty principle, the product of the temporal and spectral pulse widths must be greater than unity, implying that a light source with a broad spectrum is necessary to obtain ultra-short pulses. For any ultra-fast laser pulse, the minimum achievable duration for its spectrum is known as the Fourier Transform Limit or bandwidth limit. When a pulse is at the transform limit, its spectral phase is frequency-independent and zero, which implies a minimal time-bandwidth product and an absence of chirp [99]. Pulse propagation in any dispersive medium can result in pulse broadening. That is why compressors (or stretchers) with negative group velocity dispersion are used to control the pulse chirp and bandwidth.

The femtosecond laser system with which almost all the results presented in this dissertation were obtained is shown in Figure 3.5. The workhorse of the setup is a one-box integrated Ti:sapphire regenerative amplifier Coherent Astrella which is one of the two ultrafast amplifiers available in the Laboratory of Magnetism at the University in Bialystok.

Although Astrella is integrated into a single sealed box, it consists of several separate components, each with dedicated hardware. The operation of Astrella, like most amplifiers, is based on the master oscillator and power amplifier (MOPA) configuration. In this configuration, an ultrafast mode-locked laser serves as the master oscillator or seed laser, defining the signal with its pulse shape and properties, which are ultimately amplified by the power amplifier. Despite its increased complexity compared to direct methods of achieving desired output power, this configuration offers benefits such as the ability to adjust, optimize, or modulate the signal even at low power levels. As a result, the number of factors and components in the system that are susceptible to high optical intensities is significantly reduced.

In the described system, in the first stage, the seed signal is created in the sealed Ti:sapphire Vitara-S-OEM oscillator. The oscillator uses an integrated Verdi pump laser. The femtosecond signal generated by the oscillator has an output power of approximately 560 mW, a repetition rate of 80 MHz, and a base wavelength of 800 nm. The system allows for extracting a portion of the seed beam externally.

Next, the signal is transmitted to the regenerative amplifier. Here it is trapped in a cavity that allows the beam to be repeatedly passed through the gain medium, which is

again the broad bandwidth Ti:sapphire crystal. The crystal is pumped up or activated to a high energy state by the Revolution 65 high-power Q-switched pulsed laser working at 527 nm wavelength with average power up to 38 W on a 1 kHz repetition rate. Each time the seed passes through the activated crystal, the signal accumulates energy to finally be released outside the resonator. The confinement of the beam in the resonator of the amplifier is done utilizing polarizers and electronically triggered Pockels cells. One Pockells cell is responsible for introducing the seed signal to the resonator, and the other acts as an output coupler. The synchronization of the opening times of the laser and the Pockels cells is done by a time delay generator Elite SDG. Adjustment in synchronization times strictly affects the amplification performance by for instance defining the number of cavity roundtrips. Using the Pockels cells with its time synchronization well-defined by an electronic signal facilitates the synchronization of the laser with other components in the system. Moreover, it allows the setup to operate in a burst pulse triggered internally or externally by a TTL signal or even a single-shot regime.

The regenerative amplifier makes it possible to amplify the seed signal up to average optical power of nearly 10 W. This amount of energy enclosed, in a single ultrashort of 35 fs, translates into tremendous unimaginable peak power in the order of 250 gigawatts. Even the largest nuclear power plants in the world supply only several gigawatts of electricity to the grid, which is a small fraction of this amount. Operating and amplifying the light to such high peak power values leads to many technical difficulties. Therefore, the amplified impulse is intentionally extended in time by introducing a chirp using diffraction gratings, which lowers its peak power. Subsequently, the final step in shaping the beam is to restore its initial temporal properties by compressing the pulse. For this purpose, a sealed compressor with an electronic compression level setting is used. Finally, the output beam, compressed to its time-bandwidth limit, achieves an optical power of 7.6 W, corresponding to 7.6 mJ energy at a repetition rate of 1 kHz with a central wavelength of 800 nm.

All of the described steps happen in a boxed device with most of its internal components sealed. Daily operation requires a minimal amount of maintenance. The whole system is water-cooled by an external chiller. After switching on, the laser stabilizes thermally within several dozen minutes.

To perform magneto-optical experiments in ferrimagnetic dielectrics, a wavelength tunability for both a pump and a probe wavelength is necessary. This is because the excitation of magnetic order particularly in the case of photo-magnetic effect is spectrally selective. Different pump wavelengths can be tuned to exact optical transition in examined material. Moreover, spectral tunability can facilitate the optimization of MO microscopy. The ability to adjust the wavelength of the probe beam can be matched to the transmittance characteristics of the sample, thereby positively affecting the sensitivity of probing in the Faraday geometry. That is why the initially strong femtosecond beam emitted by the amplifier is divided into separate branches in which it will be possible to convert the wavelength to the desired one through nonlinear interactions.

As shown in Figure 3.5, the beam is divided into three branches. Splitting the beam with such high power requires a lot of caution. Before reaching the beamsplitters, the laser beam diameter is increased in a form of a telescope created from parabolic mirrors, which are not marked in the drawing. This reduces fluency and helps to stay below the material damage threshold. One branch of the beam stays unmodulated, and two of them are directed to two separate colinear optical parametric amplifiers Light Conversion

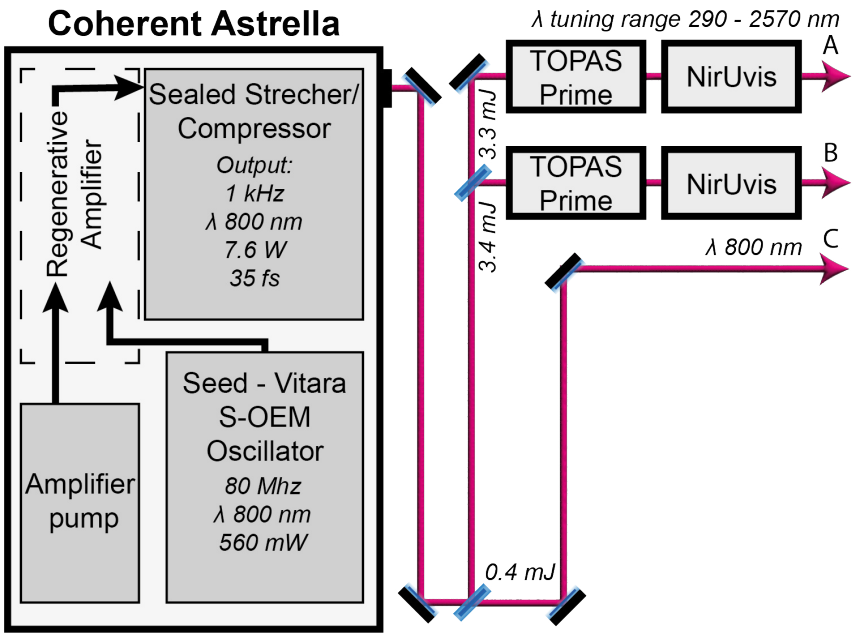

Figure 3.5: The scheme of a three-color femtosecond laser system based on the commercially available ultra-fast Coherent Astrella amplifier. The wavelength of output beams A and B can be separately tuned by Optical Parametric Amplifier (OPA) Light Conversion TOPAS-Prime with optical frequency mixers Light Conversion NirUvis. The third beam C taken directly from the amplifier has a constant wavelength of 800 nm.

TOPAS-Prime with optical frequency mixers Light Conversion NirUVis. The wavelength of both pump and probe pulses can be independently tuned in the 290–2570 nm range.

The OPA is the device that allows wavelength conversion by using nonlinear parametric interactions with nonlinear crystals [100]. The device is similar to optical parametric oscillators (OPO), however, it is not using an optical cavity to resonate any signal many times inside. The incident ultrashort pulse from the high-energy laser amplifier goes directly into the device illuminating the suitable nonlinear crystal. Reversly like in the process of harmonic generation single photon can split its energy into two photons according to the principle of conservation of energy [101]. Therefore the energy from the incident high-frequency ω_3 and high-intensity beam is transferred to a lower frequency and lower-intensity „signal" beam ω_1, in addition forming the another „idler" beam with frequency ω_2 to maintain energy conservation.

$$\hbar\omega_3 = \hbar\omega_1 + \hbar\omega_2 \tag{3.16}$$

Theoretically, the signal frequency can be amplified in the range from 0 to ω_3, and correspondingly the idler frequency can vary from ω_3 to 0. The efficiency of the OPA process is dependent on satisfying both the energy conservation requirement and the phase matching condition, which can be denoted as:

$$\Delta k = k_3 - k_1 - k_2 = 0 \tag{3.17}$$

In which k_i represents the wave vectors of the interacting beams respectively.

This process allows for a continuous and adjustable setting of the center frequency determined by the phase-matching condition. This enables easy tuning over a wide spectral range in a laser system with a fixed central wavelength, making it a versatile and efficient method of frequency control [102].

Using a combination of beams processed in the OPA TOPAS-Prime with the additional extension in form of the NirUvis frequency mixer significantly increases the wavelength output range. Devices provide automated nonlinear interaction selectivity with additional frequency sum or doubling within the signal and idler beams, and appropriate spectral filtering with the output polarity control.

3.4.2 *Pump & probe method*

The investigation of phenomena on sub-picosecond timescales, such as ultrafast spin dynamics, presents technical challenges to overcome. One of the key challenges is the dilemma that to measure an event in time, it is always necessary to operate with a shorter event. This means that to track an event, not only a shorter probing light pulse is required, but also a detector whose response time is even shorter. The time scale of ultra-short femtosecond optical pulses exceeds the responsiveness of any electronic-based detectors. Even measuring the temporal properties of the pulse alone becomes a challenge. To address this issue, it is necessary to utilize a portion of the pulse as a self-referencing tool for measuring its own characteristics.

The laser pulse train split on two beams can be easily varied in the time domain, simply by increasing the total optical path of one beam branch. Such as in interferometric techniques the mechanical delay line, controlling the position of the mirror which reflects the ultrashort pulse, can precisely control the beam path distance and thus the delay. This allows for mapping the time to the translation in space. Since the light beam has to travel to and from the mirror, typically the translation of the mirror is twice as long as the light travels. With precise position control provided by the delay line, temporal separations in the range of a few femtoseconds can be easily achieved.

This concept can be successfully adapted for pules characterization measurements. The most basic all-optical technique for measuring ultrashort pulses involves an intensity autocorrelator based on interferometry. In the Michelson interferometer configuration, two copies of the ultrashort pulse are focused and superimposed spatially and temporarily, creating an intensity output on the detector that can be expressed as the first-order autocorrelation function of the delay Δt.

$$I_1(\Delta t) = \int_{-\infty}^{+\infty} |E(t) + E(t - \Delta t)|^2 \, dt \tag{3.18}$$

However, the first-order autocorrelation function, which can be observed and treated as the overlap signal, does not give any information about the pulse duration. Instead, it can be understood as an analog of the light spectrum and is related to the coherence length of the laser pulse [103]. Nevertheless, the pulse can gate itself using optical nonlinearities, when a nonlinear medium is introduced to the interferometric setup. In this case, the resultant signal is directly proportional to the second-order autocorrelation function. However, the autocorrelation function does not provide complete information about the pulse properties. Firstly, the symmetry of the autocorrelation function with respect to delay results in the loss of information about the direction of the pulse. Moreover, intensity

autocorrelation does not provide information about the temporal shape (phase) of pulses. Therefore, estimating the actual pulse duration requires assuming the specific pulse shape. More sophisticated methods that detect additional beam parameters, such as spectrum evolution over the delay Δt, are necessary for comprehensive pulse characterization [98, 104].

Ultrashort pulses possess not only the capability to track ultrafast dynamics but also the ability to initiate them. This property finds application in a concept known as the pump-and-probe method. The principle of this method is illustrated in Figure 3.6. A train of ultrashort pulses from the same source is split into two optical branches. One of these branches, typically the stronger one, is referred to as the pump beam. It serves as an optical stimulus, initiating the phenomenon under investigation. The other branch, known as the probe pulse, arrives later with a precisely adjustable delay, providing a stroboscopic reference for the changes induced by the pump beam. By examining the time-resolved alterations in various properties of the probe beam, such as intensity, spectrum, and polarization, numerous experimental scenarios can be designed to study specific phenomena.

Theoretically, there is no distinction as to which branch the delay line is applied. The crucial factor is the relative time difference between the pulses. Consequently, scenarios where the total distance of the probe beam is extended or the total distance of the pump beam is reduced are equivalent. However, from an experimental standpoint, it's important to consider potential minor beam misalignments introduced by the movement of the delay line. Furthermore, when dealing with a substantial increase in distance (in the nanosecond range), divergence of the laser beam may occur. Therefore, the selection of the proper adjustable beam should always be considered.

In the case of laser-induced magnetization dynamics, the first part of the pulse (pump), which is significantly stronger, triggers the motion of magnetization. Subsequently, the other part of the pulse (probe), suitably delayed, detects the induced magnetic changes. Measuring the changes in the probe intensity or polarization induced by the pump pulse enables the reconstruction of the actual laser-induced magnetic changes. The temporal resolution, determined by the pulse duration, is applicable for studying electron dynamics and spin oscillations. By selecting the probe pulse spectrum from the far-infrared, optical, ultraviolet, or x-ray range, different spin and orbital degrees of freedom can be probed, providing multiple perspectives on the same phenomenon and yielding comprehensive information [11].

In described setup, two delay lines (Newport DL325) were used separately for each laser beam emerging from the OPA. A multi-reflective retroreflector mounted on the delay of each delay line quadrupled the incremental motion to the optical distance resulting in pulse delay shifting Δt scale up to 4.4 ns. Minimum incremental motion with a guaranteed bidirectional repeatability of ±0.15 µm corresponds to 8 fs resolution, which is shorter than a laser pulse duration.

Single and multiple pulse operation

The ultrafast laser ensures a stable comb function of optical pulses with a repetition rate of 1 kHz. This repetition rate offers multiple ultrashort stimuli over time. Multiple pulses, which can be integrated over time can be used with great success and sensitivity to study non-stochastic and repeatable phenomena. This particularly refers to the conventional pump and probe method, which can probe many transient events in their actual time of

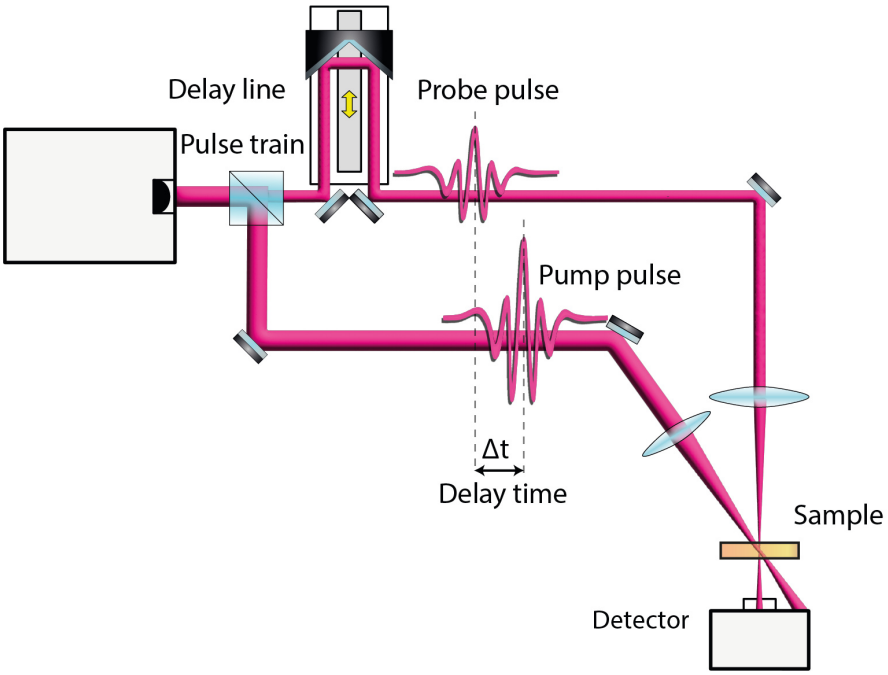

Figure 3.6: The conceptual scheme of the pump and probe method. The femtosecond pulse train is divided into a pump beam (usually the stronger one) and a probe beam. The time delay between these two pulses is regulated by adjusting the spatial separation on the delay line.

occurrence. However, the pump and probe methods are not universally applicable to all phenomena. Ultrafast processes that are non-repeatable or difficult to reproduce, such as irreversible chemical reactions, laser-induced damage, or scattering on living tissue, necessitate the use of so-called single-shot techniques. In this context, the term "single-shot" denotes capturing the entire event without repeating it. The entire measurement sequence is conducted in real-time with the help of a variety of specific methods, in which typically the probing event originates from just one laser pulse [105].

However, it should be noted that in this dissertation the term "single-shot" refers to the magnetization switching achieved by a single laser pulse. Recording of the „magnetic bit" using a single laser pulse changes the initial state of the magnetization within single-shot without returning to the starting point. Therefore, a way to extract individual pulses on demand from the train generated by the laser is necessary.

Different solutions can be used depending on the repetition frequency of the laser to ensure single-shot operation. The conceptually most simplistic approach is just to use a mechanical shutter. Such a device has a large aperture size and does not affect any of the beam parameters. Moreover, it can be synchronized with one of the edges of the electrical signal supplying the optical pulse generation in the laser's regenerative amplifier. However, mechanical shutters are limited by their large inertia and are only suitable for relatively small repetition rates, typically in the tens of Hz range. In the context of single-pulse selection over a longer period, the close/open repetition rate is not as critical. Alternatively, more sophisticated systems utilizing choppers can increase the available repetition rates mechanically. For higher repetition rates, electro-optic[106] or acousto-optic[107] modulators can be employed. These devices offer precise timing, but

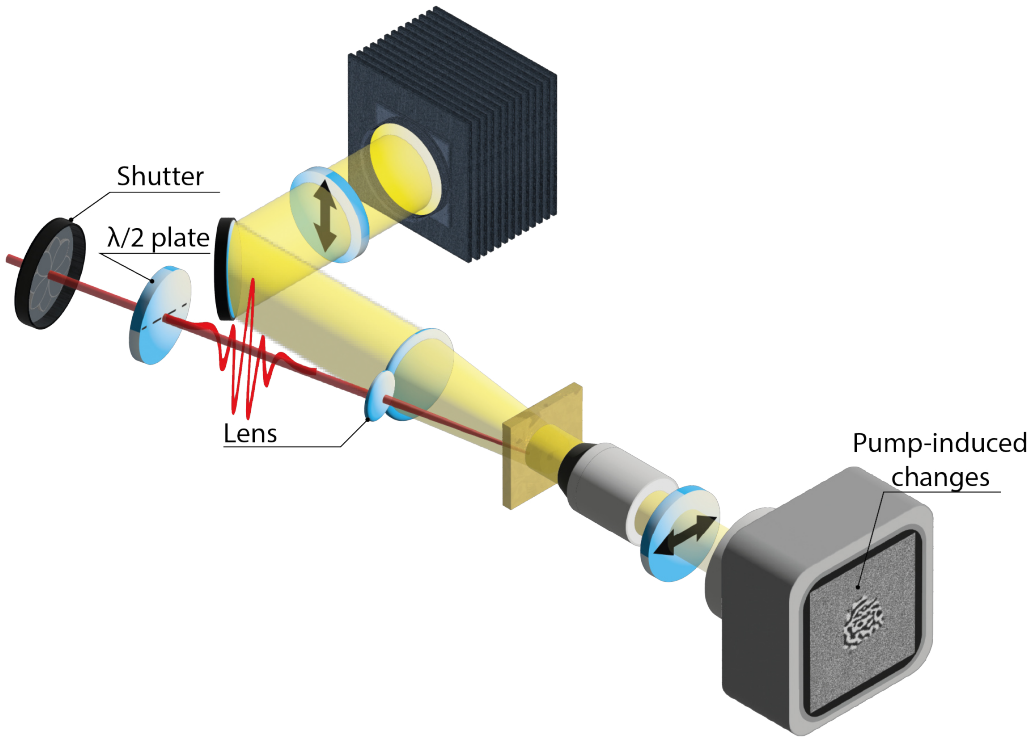

Figure 3.7: Static MO Faraday microscopy setup with an introduced pump laser pulse. This setup allows for the visualization of long-time pump-induced changes, such as magnetization switching. Both pulse trains or only a single pulse can be used to stimulate the sample. Using a half-wave plate facilitates determining the proper polarization plane for the pump pulse.

they may introduce losses in light transmission, have limitations in maximum aperture size, require additional control and polarization, and may not provide perfect selectivity, allowing a part of the beam to pass [108].

In the presented experimental setup, it is noteworthy that the Astrella femtosecond laser system can operate in also a single-shot or burst regime. This is achieved through direct control of the built-in Pockels cell to deterministically generate the desired pulse train. However, it has been observed that such operation regimes can disrupt the thermal equilibrium in the cavity of the amplifier, leading to a negative impact on the stability of the generated pulse train over the long term. Therefore still, the preferable way of obtaining a single-shot regime is to use some kind of external modulation.

Because the built-in laser divider is also capable of decreasing its base repetition rate by dividing it by natural numbers it is possible to use simple mechanical shutters to obtain single-shot on demand. As shown in Figure 3.13a, the laser repetition rate was reduced by 40 times using, from 1 kHz to 25 Hz. To ensure proper pulse synchronization, a digital time delay generator (DG) (Stanford Research Systems DG645) was used, which is capable of picking no more than one trigger pulse per second, defining the base system operation frequency at 1 Hz Figure 3.13b. This provides a sufficiently long time window for other components synchronized in the experiment and ensures single pulse selectivity. By using separate shutters all beams from the Astrella can be controlled independently.

The used mechanical shutter (Thorlabs SHB05T) has a relatively long open-close time cycle (>35 ms). It transfers to the opening and closing times of about 10 ms. As a result, the first pulse is always suppressed, and the Delay Generator (DG) always selects the second

subsequent pulse, as shown in Figure 3.13c. The time shift introduced from the triggering pulse to the subsequent optical pulse allows enough time for the mechanical shutter to open, as illustrated in Figure 3.13d. This configuration facilitates easy synchronization of other components, such as a camera, with an incident ultrashort pulse. Further details of the experimental setup using synchronized camera and imaging will be provided in the section on Time-resolved single-shot imaging.

The use of external shutters, even at the reduced operation frequency, leads to a more stable laser cavity and decreased energy fluctuations in the pulse train when compared to burst or single-shot built-in regimes. The system is controlled by a PC using LabView software, providing flexibility and the ability to integrate with various other components, such as coils, step motors, modulators, or heaters. This allows for the design of multiple experimental variations.

The setup for the observation of the magnetic domain structure changes due to the single pump pulse excitation is illustrated in Figure 3.7. The pump beam is directly focused on the sample by the lens with a 100 mm focal distance to a diameter of about 130 µm. The piezo motor-driven mirror (CONEX-AG-M100D) was used for adjusting the pump beam position. The half-wave plate enables the rotation of the linear polarization plane of the pump beam, adjusting it to the crystallographic axes of the sample. The introduced shutter facilitates single-shot operation within the discussed scheme. Since the pump-induced changes are observed using LED light, rapid dynamics cannot be captured. This setup was primarily employed to examine switching efficiency, typically determined by the area of the switched region.

3.4.3 *Time-resolved magnetization dynamics*

Utilizing the pump and probe method allows for time-resolved studies of magnetization dynamics and spin precession. The common implementation[69, 109, 110] of this setup is illustrated in Figure 3.8. Analogous to the previous scenario, a focused pump pulse stimulates the sample, inducing spin precession. The densely focused linearly polarized probe beam acquires Faraday rotation θ_F as it passes through the sample, which in this dynamic case is proportional to the time-dependent oscillating out-of-plane magnetization component. By adjusting the delay line to introduce a controlled time difference Δt between the pump and probe beams, the entire time-dependent behavior can be extracted.

From an experimental standpoint, it is typical for both beams to be densely focused on the sample, with the probe beam diameter usually being less than 70 µm and smaller than the pump beam diameter. This allows for precise localization of the pump-induced changes in the desired region and increases sensitivity. Since the pump beam is primarily used to initiate the initial motion of magnetization, ideally it should be completely blocked after interacting with the sample. Any remaining portion of the pump beam that passes through the optical setup to the detector will act as a parasitic signal, as the detection relies solely on observing changes in the probe beam. The spatial separation of both beam branches, which are not aligned, facilitates the removal of parasitic pump effects. However, it is always recommended to incorporate an additional band-pass filter with a wavelength adjusted to that of the probe beam, after the sample. Conversely, the fluence of the probe beam should be maintained at a small value, significantly lower than that of the pump beam, to ensure that it does not induce any optical or magnetic effects on the sample.

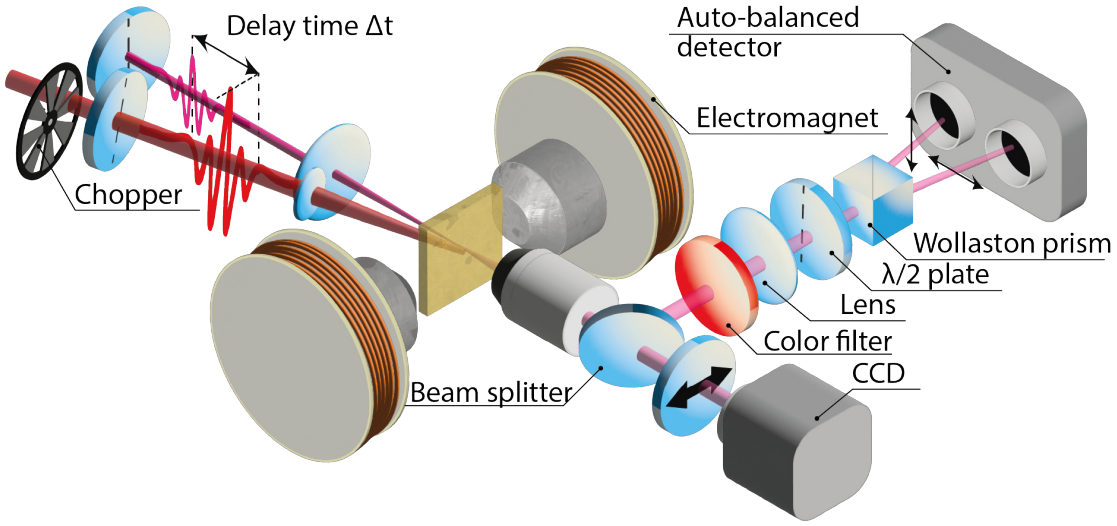

Figure 3.8: The time-resolved pump (red) and probe (rose) scheme employed for investigating magnetization dynamics. The transient Faraday signal detection is performed using an auto-balanced photo-diode. The implementation of lock-in detection, along with signal modulation using a chopper in the pump signal, enhances measurement sensitivity. In this setup, the inclusion of a direct optical branch that directly passes beams to the CCD camera is optional. However, it allows for domain observation and facilitates beam alignment as well as the determination of spatial overlap.The electromagnet allows for studying the magnetization dynamics affected by external magnetic fields.

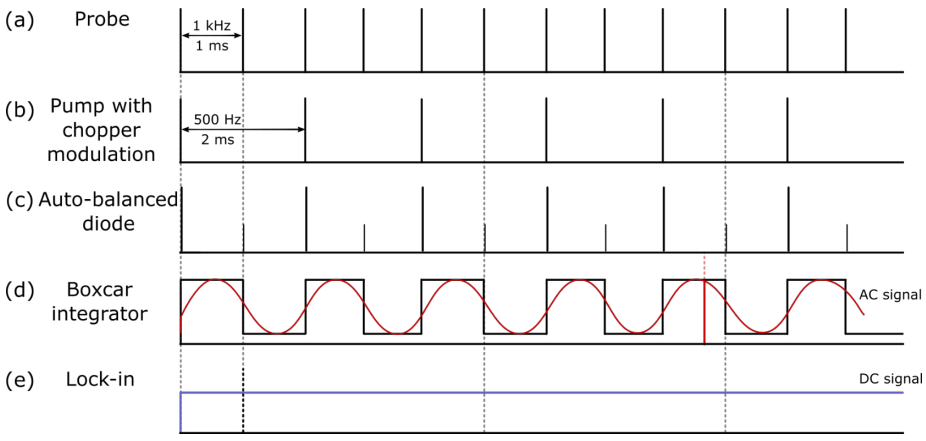

Figure 3.9: Timing Synchronization Scheme for time-resolved diode measurements (a) The probe beam illuminates the sample with a laser fundamental repetition frequencyf. b) The pump beam modulated by the chopper blades to $\frac{f}{2}$ c) Electronic signal in the form of spikes captured by auto-balanced photo-detector. d) The signal integrated by the Boxcar into a square wave. e) The synchronized DC signal measured on the lock-in, with its amplitude corresponding to the Faraday rotation.

To significantly enhance the sensitivity of the setup, instead of regular intensity measurement in cross-polarizer configuration, the auto-balanced photo-detector and lock-in amplifier were employed. To make use of the auto-balanced photo-detector, the probe beam is split into two orthogonally polarized components, vertical $I_{\parallel}$ and horizontal $I_{\perp}$, using a Wollaston prism. These components are then directed into the separate diodes of the auto-balanced photo-detector. The relationship between these components can be modulated by adjusting the half-wave plate placed before the prism. When the polarization plane angle is set to $\frac{\pi}{4}$, the intensity of both components becomes equal. Therefore, under initial conditions with no magnetization changes, the $I_{\parallel} = I_{\perp}$. Any slight disturbance from this equilibrium state will be registered by the auto-balanced photo-detector as a change in the intensity difference between the components, which can be expressed as:

$$I_{\parallel} - I_{\perp} = I_0(t)\cos^2\left(\frac{\pi}{4} + \theta_F(t)\right) - I_0(t)\sin^2\left(\frac{\pi}{4} + \theta_F(t)\right) \cong 2I_0(t)\theta_F(t) \tag{3.19}$$

The intensity of light entering the Wollaston prism, denoted as $I_0(t)$, is split into two polarized components with a phase difference of $\frac{\pi}{2}$, which can be represented as a cosine and sine functions. The approximation that simplifies the trigonometric functions is valid for small $\theta_F(t)$ angles. Time-dependences of $I_0(t)$ and $\theta_F(t)$ components are understood as their variation over subsequent measuring points in pump and probe geometry.

Notably, measuring the combined signal:

$$I_{\parallel} + I_{\perp} = I_0(t)\cos^2\left(\frac{\pi}{4} + \theta_F(t)\right) + I_0(t)\sin^2\left(\frac{\pi}{4} + \theta_F(t)\right) = I_0(t) \tag{3.20}$$

simplifies to a time-dependent intensity, essentially representing a transmission signal.

To enhance sensitivity, the repetition rate of the laser beam was modulated, enabling detection based on a lock-in amplifier. The initial pump beam repetition rate was halved to 500 Hz using a synchronized chopper, as depicted in Figure 3.9. This modification facilitated acquiring both the pump and probe sequence, as well as a probe-only sequence, which served as a reference for the lock-in amplifier (Zurich Instruments MFLI).

The ultrashort laser pulse registered by the photodiode generates a voltage spike, with a duration corresponding to the diode's response time, usually within the range of microseconds. However, these spikes, when probed at the relatively low 1 kHz repetition rate, exhibit a very low duty cycle, during which the signal largely lacks any informative content. Consequently, to enhance the signal-to-noise ratio, the Boxcar integrator (Stanford Research SR250) was employed. This analog device enables the selection of an appropriate time window, featuring the desired width and relative position with respect to the signal. The device then integrates the amplitude from this window into the rectangular signal, effectively cutting off redundant regions without pulses.

The described system allows for the measurement of ultrafast magnetization dynamics, as exemplarily shown in Figure 12. The Faraday rotation of the angle of polarization plane in the probe beam detected in the used geometry corresponds to the change in the out-of-plane magnetization component, ΔM_z. Before the pump pulse at $\Delta t < 0$, the magnetization is stabilized and aligned with the effective anisotropy field. The pump pulse creates a perturbation that excites the magnetization, moving it out of equilibrium and setting it in motion. By adjusting the time delay between the pump and probe pulses, the entire dynamics described by the Landau-Lifshitz-Gilbert equation can be captured.

The observed dynamical evolution of the Faraday rotation, $\Delta\theta_F$, in the form of damped oscillation can be described as follows:

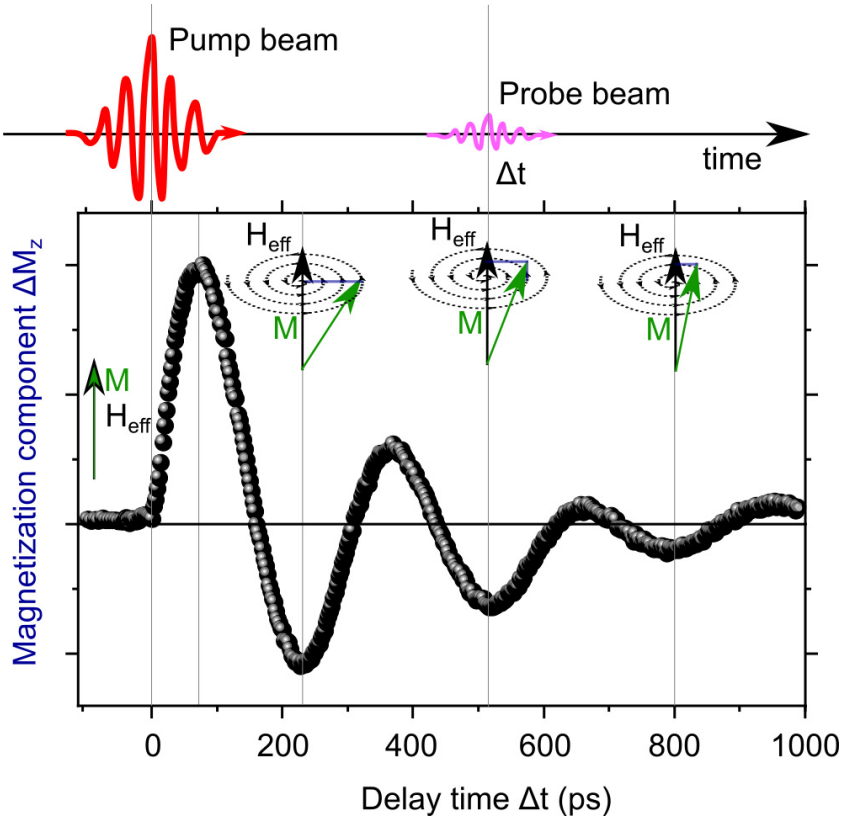

Figure 3.10: Example magnetization dynamics measured in the described stroboscopic experimental configuration. The time-controlled delay time between the pump and probe beams sets the observation point. The measured MO Faraday rotation signal is proportional to the out-of-plane magnetization component ΔM_z. Subsequent oscillations of magnetization M over the effective field of anisotropy H_{eff} correspond to the dynamical trajectory described by the LLG equation.

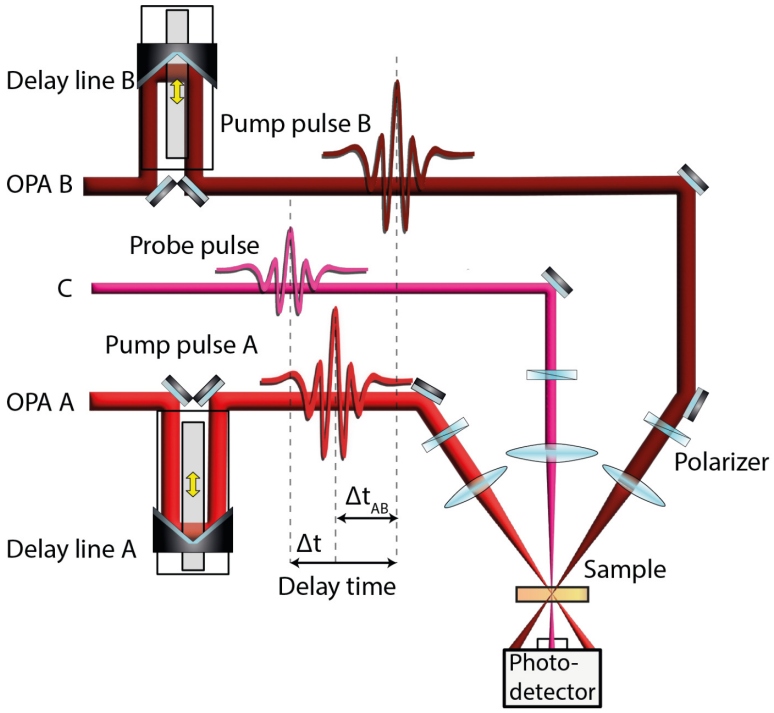

Figure 3.11: The scheme of the three-color double pump and probe method. Two pump pulses, labeled as A and B, with controllable delay times, illuminate the sample consecutively. The pulse sources are as indicated in Figure 3.5. By adjusting the relative timing of the probe pulse, the induced changes can be effectively monitored.

$$\Delta\theta_F(\Delta t) = A_F sin(2\pi f \Delta t + \varphi) exp(-\frac{\Delta t}{\tau_1}) + B exp(-\frac{\Delta t}{\tau_2}) \tag{3.21}$$

Where Δt is the mutual delay between the pump and probe beams, A_F is the amplitude of the oscillating part, f is the frequency of oscillation with phase φ. The characteristic decay time of the precession is marked by τ_1. Moreover, the function contains a non-oscillatory background signal associated with optical signal which may be influenced, for example, by absorption, and which decays exponentially with an amplitude B and characteristic decay time τ_2 [49].

Time-resolved double pump and probe

An extension of the pump and probe method for measuring magnetization dynamics involves the use of an additional pumping stimulus. In this setup, the test sample is exposed to two pumping pulses separated by a controlled time interval Δt_{AB}. These pulses can be directed at the sample linearly using a beamsplitter in one path [32, 53], or as shown in Figure 3.11, in two separate branches allowing total control over the parameters of both beams. The induced changes can be examined similarly to the previously discussed setups, both in static cases using magneto-optical microscopy with LED light illumination, and in dynamic scenarios with the time-resolved probe beam.

To effectively control the mutual position of the beams, an additional delay line has to be utilized. This allows for the determination of the mutual spatial and temporal overlap of all three beams.

In one scenario, one of the pump beams and the probe beam can be directed to the delay lines. In this case, the first pump pulse acts as the reference point. By increasing the length of the optical path for the second pump beam, the parameter Δt_{AB} can be defined. Similarly, increasing the probe optical path distance defines Δt.

Alternatively, both pump beams can be directed to the delay lines, where they will be moved apart relative to each other, thus defining Δt_{AB}, and also relative to the static probe beam, introducing Δt delay. In this case, the delay lines will need to move in the reverse direction, shortening the length of the pump beam paths.

3.4.4 *Time-resolved single-shot magneto-optical imaging*

The utilization of an auto-balanced photo-diode with lock-in detection for tracking magnetization dynamics offers an unmatched level of sensitivity. However, this particular setup does not provide any spatial resolution. To overcome this limitation, two primary approaches can be identified to achieve spatio-temporal resolution.

Firstly, by controlling the relative positions of the pump and probe beams, a scenario involving repeated X-Y scanning of the beam can create a spatio-temporal magnetization map [93, 111–113].While this approach maintains high sensitivity, performing multiple spatial scans can be time-consuming, leading to reduced spatial resolution.

Alternatively, dynamic changes can be directly visualized using a synchronized CCD camera, where the probe pulse acts as a stroboscopic illuminator. As the camera captures images using only the probe light, the exposure time of the camera becomes irrelevant and can even be in the slow millisecond range. The resulting image, presented in 2D format, provides a qualitative representation of the dynamics, which can be transformed into quantitative information by appropriately scaling the intensity levels.

Imaging methods based on pump and probe techniques have been recognized for nearly four decades, initially capturing processes on photographic films [114]. Over time, many diverse adaptations of this general concept have been extensively employed, especially in chemistry and biology [115, 116].However, the pump and probe methods cannot be universally applied to all phenomena. For stochastic processes that are non-repeatable or challenging to reproduce, such as irreversible chemical reactions, laser-induced damage, or interactions with living tissues, the concept of "single-shot imaging" becomes crucial. Here, "single-shot" refers to the capability to capture an entire event without needing to repeat it. The entire measurement sequence occurs in real time, enabled by just one laser pulse [105].

The setup for time-resolved single-shot imaging is illustrated in Figure 3.12. In this configuration, the magnetization dynamics initiated by a single pump pulse is observed through MO microscopy using a single probe pulse. The probe pulse is positioned on the sample using an adjustable lens, staying slightly out of focus to ensure illumination of a sufficiently large area. The focal point of the pump beam is positioned before the sample, allowing it to illuminate the sample's surface with a divergent beam. This arrangement serves to protect the sample and objective, as well as to prevent any unintended probe-induced non-linear processes. Moreover, by incorporating a quarter-wave plate after the objective and employing the rotating analyzer method, it becomes possible to monitor the ellipticity of the probe light[117]. The spot sizes of the probe laser beam, which are considerably larger than the localized spot size of the pump beam on the sample surface,

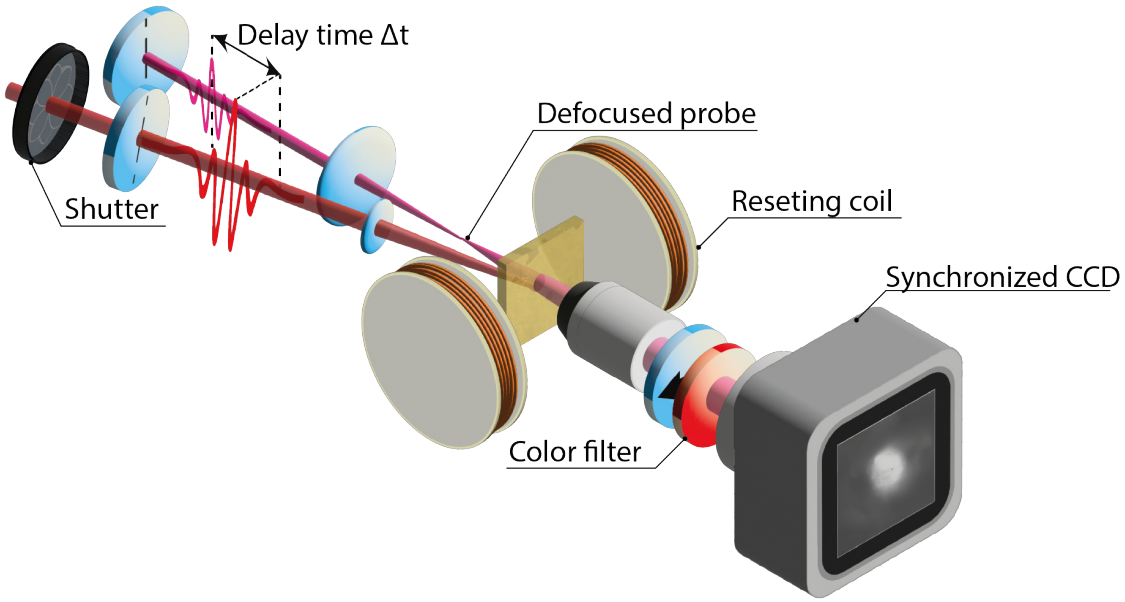

Figure 3.12: The time-resolved pump and probe scheme for imaging of magnetization dynamics. The dynamical changes are captured on a synchronized CCD camera illuminated by the defocused probe beam. Resetting coil allows for restoring the initial state of the magnetization in the sample after every exposure.

are depicted in Figure 3.14. In both cases, a lens with a focal length of 100 mm was employed.

The CCD camera utilized in this setup (Instruments ProEM 1024) was configured to operate in full-frame mode. It records and digitizes 16-bit images with a resolution of 1024×1024 pixels^2. To mitigate thermal noise and unwanted charge accumulation, the built-in continuous cleaning procedure of the array was employed between each frame. It removes any charge from the array until a trigger pulse is detected and stops as soon as the frame collection begins.

For eliminating residual pump light, a spectral bandwidth color filter was placed before the CCD camera. The camera is triggered immediately after the mechanical shutter, and its exposure time is set to 1 ms, as depicted in Figure 3.13, though this aspect isn't critical for this kind of experiment. Additional time is required for the camera's data acquisition process.

Given that a single pump pulse is adequate to switch the magnetization, the experiment is non-stroboscopic. Consequently, prior to the subsequent shot, a predefined 100 ms duration voltage pulse is directed to the resetting coil via a power supply (Kepco BOP 72-6 DL). This pulse generates a magnetic field with an amplitude of H = 100 Oe, used to restore the initial state of the sample's magnetization.

Following this, while the pump beam is still blocked by the mechanical shutter, only the probe beam illuminates the sample. The image captured at this stage serves as the background or reference image. Ensuring a new background image for each measurement sequence helps counteract the impact of long-term laser beam instabilities.

Finally, the mechanical shutter opens, and both the pump and probe beams illuminate the sample during a single shot of 35 fs, creating the time-resolved image. This entire sequence is consistently repeated for each delay value Δt.

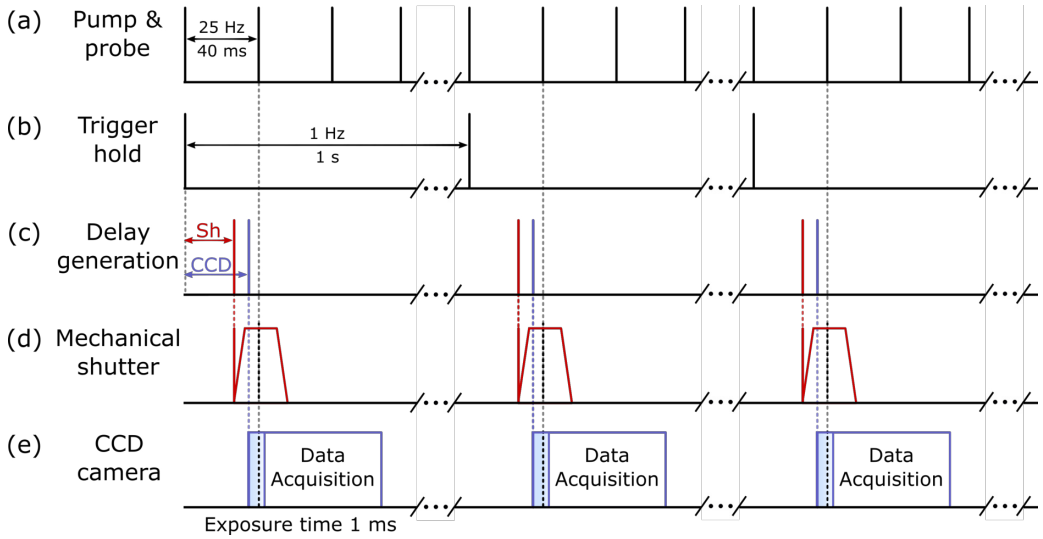

Figure 3.13: Timing Synchronization Scheme (a) The pump and probe pulses are formed from an electronically triggered amplifier's pulse, which serves as the synchronizing edge. (b) The digital time DG holds the trigger for 1 second. (c) TheDG omits the first pulse and synchronizes the shutter and CCD camera with the subsequent one. (d) The mechanical shutter's open-close time. (e) The CCD camera exposure time and the time required for obtaining the required data. Note: The delay between the pump and probe pulses is negligible and not noticeable in the presented scale.

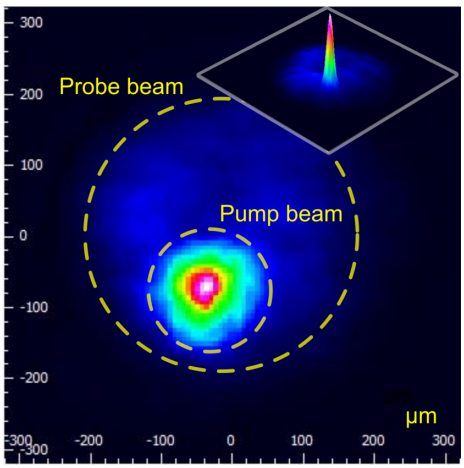

Figure 3.14: The profiles of the probe and beam used for time-resolved imaging. In this configuration, the pump is intentionally off-centered to illuminate the region with the most uniform probe illumination.

3.5 MULTI-FUNCTIONAL SETUP FOR SPATIO-TEMPORAL MEASUREMENTS

All the measurement schemes discussed in this work have been integrated into a single functional multi-color pump and probe system, enabling the execution of various measurement scenarios. This configuration is depicted in Figure 3.15 . By employing flip mirrors, the laser beam can be conveniently redirected to create different arrangement combinations, as follows:

- The most stable beam, taken directly from the amplifier, with a non-adjustable wavelength of 800 nm, serves as the probe beam in time-resolved experiments using the auto-balanced detector. The beam from OPA A, modulated by a chopper, functions as the pump beam.
- By using a flip mirror (FM) 2, the adjustable beam from OPA B, passed through and filtered in the pinhole, serves as the probe with a 650 nm wavelength. Both the OPA A pump beam and OPA probe operate in the single-shot regime facilitated by the reduced laser frequency and mechanical shutters. This configuration is employed for time-resolved imaging.
- FM 1 redirects the OPA B beam to function as a pump, enabling double pump and probe measurements.
- Through flip mirror (FM) 3, static MO imaging on a CCD camera is achieved using an LED illuminator.

In all configurations, the OPA A beam serves as the pump beam with a wavelength set to 1300 nm.

The entire system is integrated and managed through a personal computer utilizing LabView software. This approach guarantees flexibility and allows for the integration of the system with diverse components like coils, step motors, modulators, or cryostats, enabling the design of various experiment configurations.

The implementation of spatial filtration using a pinhole has significantly improved the quality of time-resolved imaging, particularly when observing magnetic domains with low magnetic contrast, such as in the case of YIG:Co. Spatial filter pinholes are useful components, often employed to maintain high beam quality in high-energy pulsed laser systems[118]. In this context, a filter featuring a 50 µm diameter, as illustrated in Figure 3.16, was implemented to reduce high-frequency noise within the probe-pulse beam profiles. This also helps minimize the spatial shift of illumination linked with the movement of the delay line. To facilitate the beam's passage through the pinhole, two lenses with a focal length of 40 mm were employed. To couple and decouple the beam through the pinhole, two lenses with a focal length of 40 mm were employed. Nevertheless, even within this non-uniform profile, the presence of the magnetic domain structure remains distinguishable within the images and the cross-section profile, as demonstrated in Figure 3.16.

To obtain a better contrast and to suppress the impact of the probe's wavefront nonuniformity, differential images were generated. These were obtained by subtracting image B, taken after irradiation with a single pump pulse, from the initial background image A, as illustrated in Figure 3.17. However, a few considerations need to be taken into account when working with this image stack. First, for meaningful comparison of images acquired under varying illumination conditions, their intensity levels should be normalized. To

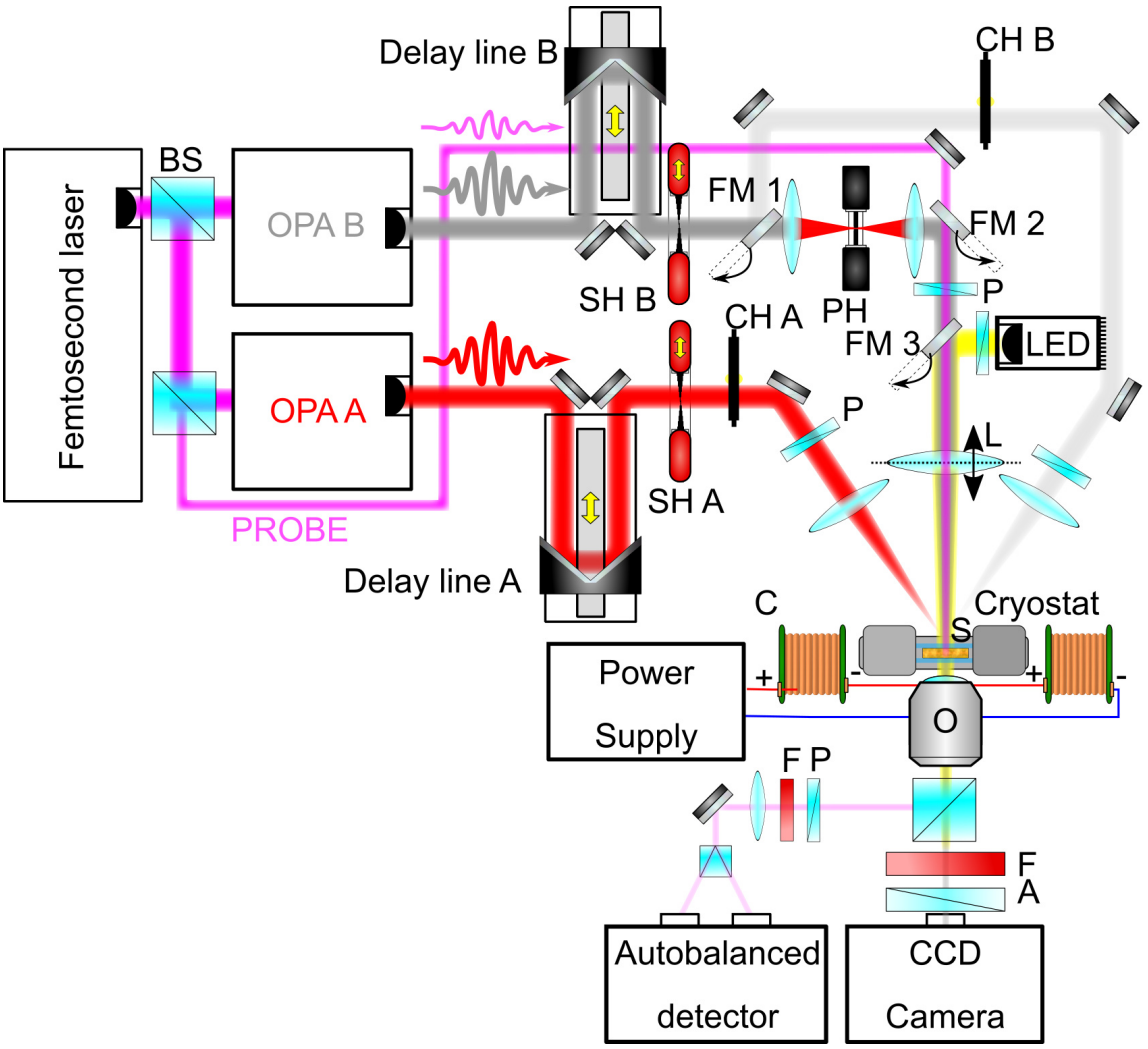

Figure 3.15: The multi-functional three-color pump and probe setup designed for spatiotemporal measurements of magnetization changes, combining all the experimental schemes discussed earlier. The use of a flip mirror allows for the selection of the beam paths and, consequently, the experimental geometry. All the results presented in this thesis were obtained using this setup developed at the Laboratory Femtosecond Spectroscopy in Bialystok. The following symbols are used in the scheme: TDG - Time delay generator, BS-Beam splitter, OPA- Optical parametric amplifier, P - Polarizer, L - Lens, S – Sample, F- Colour Filter, A - Analyzer, CH Chopper, SH - Shutter, FM - Flip mirror.

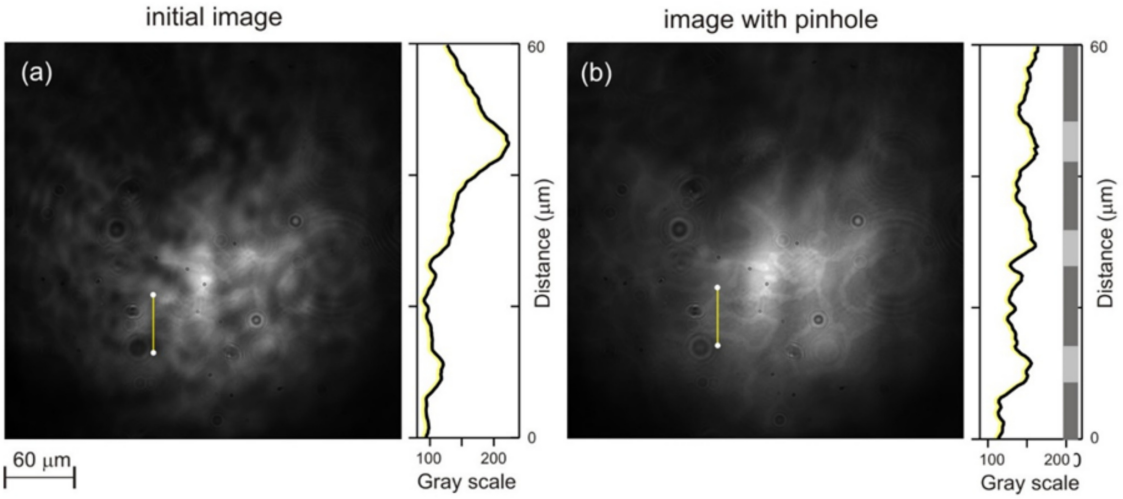

Figure 3.16: Magneto-optical images captured in the YIG:Co film, illuminated by a single probe pulse. The corresponding distance profiles are in line with the yellow cross-section marked on the images. a) Initial Image, taken without the use of a pinhole, reveals the impact of the nonuniform incident wavefront, resulting in high-frequency noise. This noise masks the true nature of the magnetic structure. (b) Image with Pinhole: In contrast, this image, obtained using a pinhole, presents a more accurate depiction of the domain structure. The revealed domain structure corresponds to the large (1) M– and small (5) M+ magnetic domains, which are marked as stripes on the profile. These images are depicted in a normalized 8-bit grayscale format. The image dimensions are 380 × 380 µm^2.

achieve this without distorting the single image intensity levels, a uniform contrast-enhancing procedure is applied to all images in a consistent manner. This involves using the histogram of the entire stack rather than individual image histograms to rescale each image's intensity levels.

Second, it is crucial to ensure that the background intensity level remains consistent across all images. Without this uniformity, differential images would not be spatially comparable. If background intensity is not consistent, additional post-processing algorithms can be employed to rectify this issue [119].

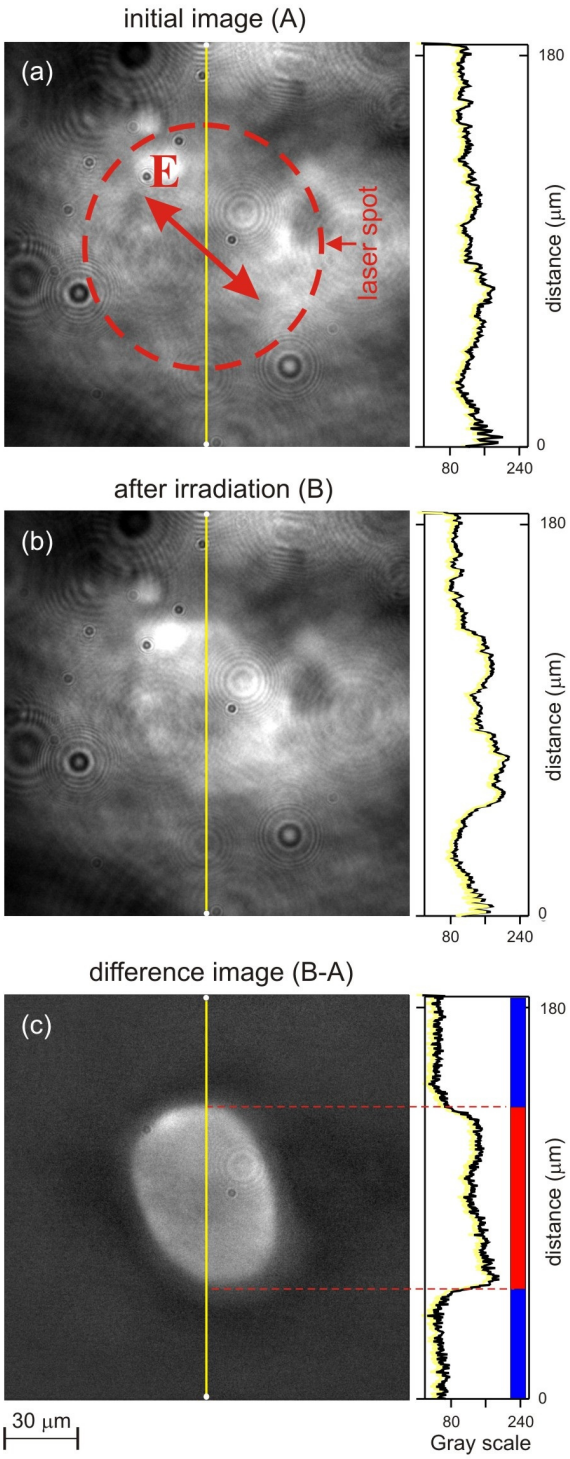

Figure 3.17: a) Single-shot imaging of YIG:Co in a monodomain state with magnetization (1) M- along the [11-1] direction before any excitation, illuminated only by a single probe pulse with λ = 650 nm. (b) Image recorded after a single pump pulse with λ = 1300 nm for Δt = 185 ps. The magnetization of the switched domain was along the [1-11] direction and corresponds to state (8). (c) Differential image (B–A) The slightly elongated shape of the switched domain is related to both the beam shape and the miscut angle of the sample and schematically marked (red dashed line) on a profile.

4

SPATIO-TEMPORAL DYNAMICS OF LIGHT-INDUCED MAGNETIZATION SWITCHING

Understanding different scenarios of nonthermal magnetization switching is inherently tied to clearly defining the initial ground and final switching states. YIG:Co films have the dominant cubic magnetic anisotropy with a complex multi-state magnetic character. As outlined in Chapter 2, at room temperature and without an external magnetic field, the magnetization in the YIG:Co sample can occupy eight distinct magnetization states, forming four different magnetic phases. Through the implementation of sample miscuts, the spatial equilibrium between these states can be disrupted, resulting in the separation of states into larger and smaller domains, which become distinguishable in MO imaging. Despite static imaging, the development of a time-resolved single-shot imaging technique enables the probing of dynamic properties in each state. This simultaneous insight into the spatial and temporal characteristics of magnetization opens up a multitude of possibilities, allowing for the nonthermal control of magnetization states in the garnets using photo-magnetic effect.

Both magnetic single-state and multi-state switching scenarios are intriguing and have not been comprehensively explored before. The key to understanding switching lies in the magnetic symmetry, which influences magnetization dynamics in every state and the angles between simultaneously moving magnetizations. Even in the most simplistic uniaxial case of a single domain switching, which has not been demonstrated before, the switching is not trivial as magnetization can be altered by temperature demagnetization, temporarily reducing the vector length. All subsequent scenarios related to multi-domain and single-domain switching can be characterized by distinct magnetization trajectories.

In this Chapter, we will describe various scenarios of photo-magnetic switching involving the ground states and their spatial properties. The first section of this chapter delves into the time-resolved dynamics of single-state switching between two magnetization states. Subsequently, our focus will be directed towards the efficiency of photo-magnetic switching in multi-domains. Lastly, from a practical perspective on applicability, we will describe the concept of minimizing the spatial extent of a single domain, with an emphasis on photo-magnetic switching within a single bubble domain in YIG:Co film.

The results discussed in this chapter were published in:

Zalewski, T. & Stupakiewicz, A. "Single-shot imaging of ultrafast all-optical magnetization dynamics with a spatiotemporal resolution", *Rev. Sci. Instrum.* **92**, 103004 (2021).

Zalewski, T., Maziewski, A. & Stupakiewicz, A. "Time-resolved photo-magnetic switching of bubble domains in ferrimagnetic garnets", *Appl. Phys. Lett.* **123**, 032402 (2023).

4.1 PHOTO-MAGNETIC SWITCHING IN A SINGLE DOMAIN AT GARNET WITH MISCUT

The simplest scenario of photo-magnetic switching, which was not investigated before, involves transitioning between two magnetization states at large magnetic domains using a single laser pulse. While the initial state may depend on the magnetic history of the sample and can be selected by applying an external magnetic field, the trajectory of the transition to the switched state is governed by the properties of the light pulse, including its fluence and polarization. Comprehensive characterization of these aspects is essential for a complete understanding of the switching process with spatial and temporal sensitivity.

As described in Chapter 2, in investigated series of YIG:Co garnet with a miscut angle the magnetization within a single domain can adopt one of eight distinct states. These states, oriented closely along the cube diagonals of the [111] crystallographic direction, are further illustrated in Figure 4.1a. The switching discussed in this section refers to the transition between states denoted as M- along the [11-1] axis and M+ along the [1-11] axis.

It should be noted that both the out-of-plane and in-plane components exhibit differences. However, considering the experimental perspective of magneto-optical imaging in the normal Faraday geometry, the imaging of such a structure follows only the out-of-plane $M_z$magnetization component of [001]-direction in YIG:Co. For a pure cubic symmetry, the in-plane components remain indistinguishable. To observe the desired in-plane component, an alteration in the probing light angle is necessary. This can be achieved, for instance, by rotating the sample plane toward the illuminating light source. Otherwise, in samples with miscuts, under room temperature conditions and in the absence of a magnetic field, the degeneracy among magnetization states is partially disrupted. This establishes an arrangement in which domains cover non-equivalent volumes leading to the in-plane component distinction based on their size either large or small labyrinth-like.

All possible domain states can be induced by applying the in-plane field of approximately 20 Oe directed along one of the four [110] crystallographic axes. Despite the existence of individual states, the domains, upon removal of the applied magnetic field, tend to organize themselves into one of four distinct phases. These phases pair states sharing the same in-plane component.[77] Notably, the sample does not need to be uniformly magnetized in every region. Localized application of a magnetic field or well-defined light pulse can selectively alter magnetization in a specific region. Resulting in for example the creation of new labyrinth-like domains, shrinking them into bubbles or completely removing them. Alternatively, the magnetic structure in the form of well-separated stripes consisting of two phases (4 states) next to each other can be obtained.

Whether the domain will be permanently stable or not hinges on the local coercive field, a factor influenced by sample grown parameters. Coercivity can undergo modifications owing to sample quality, localized defects, or surface irregularities. If the coercive field falls below a certain threshold, sustained switching might become unattainable. In such case, domains exposed to ultrashort light pulses may undergo ultrafast changes, yet, owing to the influence of slower magnetostatic processes, they tend to back to an energetically preferred alignment. Nevertheless, this scenario possesses experimental advantages, particularly for time-resolved visualization within stroboscopic pump and probe experiments. In this context, the demand for restoration to the initial state via an external magnetic field is not essential. This especially favors scenarios wherein a light pulse acts upon a small labyrinth-like or bubble domain, which after a magnetic field removal may not return to the exact same spatial position.

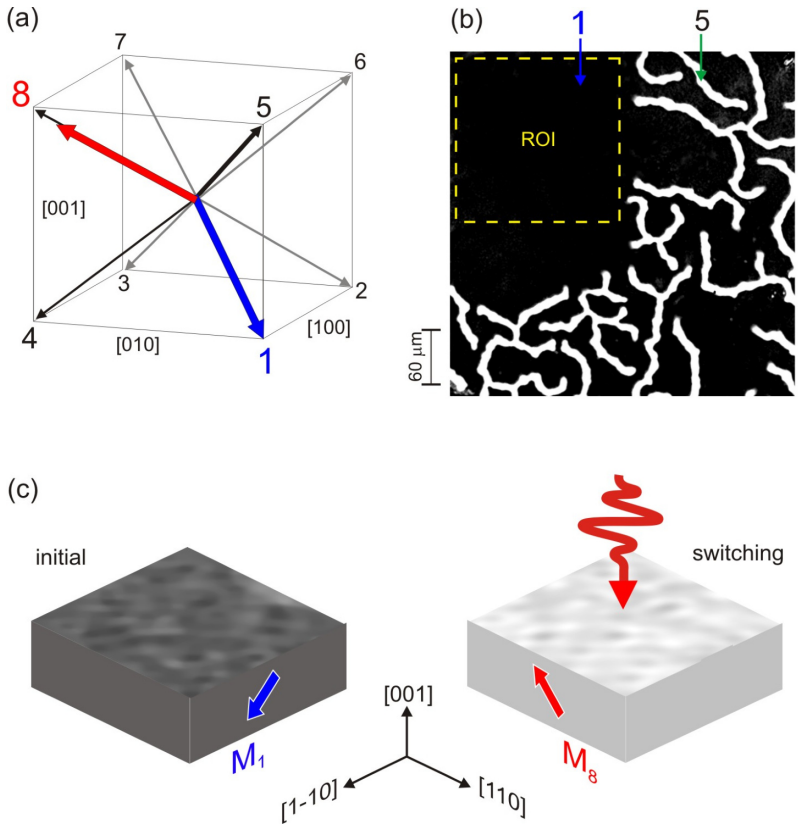

Figure 4.1: (a) Summarize of magnetization axes in the YIG:Co film (b) static MO image observed under LED illumination, displaying the remanent magnetic domain structure in YIG:Co at zero magnetic field. The contrast was enhanced through image processing. A magnetic phase comprising two states can be distinguished: a large domain (1) oriented along [11-1] and a small domain (5) along [111] directions. In specific sample areas, only a monodomain state (marked as Region Of Interest (ROI)) can be selected. The size of the image is 380 × 380 µm² c) The example of photo-magnetic single-state single-domain switching in YIG:Co with a miscut.

Previous studies[9] demonstrated the simultaneous photo-magnetic switching of both large and small labyrinth-like domains solely under static conditions. The contrast achieved in imaging the time-resolved switching dynamics was inadequate for revealing the movement of both domains. The concealed dynamic information remained obscured within a spatially averaged and blurred image. Unfortunately, a detailed spatial analysis and the determination of the spatial distribution of the effective field of the photo-induced anisotropy were not performed.

In this Chapter, to focus on dynamics within states under unified conditions, we employed a garnet with a reduced coercive field. [81] The YIG:Co sample no. 707 (see Chapter 2) was utilized to investigate all described scenarios of behavior in distinct single, multi, and bubble states. The reduction in the coercive field was achieved by slowing down the crystal growth rate from 0.28 to 0.25 µm/min during the sample preparation, which positively influenced surface roughness by decreasing irregularities. Since the laser-induced switched state reverted to the initial state within a few milliseconds without requiring restoration through an external magnetic field, this selection simplified stroboscopic experiments. It ensured the imaging stability of a consistent single domain with precise shape and position during the stroboscopic experiment

By selecting a region on the sample where no small labyrinth-like domains are present, monodomain switching can be achieved. The monodomain state, as depicted in Figure 4.1b, might be spatially confined, but it remains a stable initial state that persists over time. Its size, limited by the number of small labyrinth domains, can be manipulated by applying a magnetic field. Application of a 50 Oe external field during approximately 1 second along the [110] direction can eliminate the small domain pattern.

Using the single-shot time-resolved magneto-optical imaging setup, we directed the pump beam, linearly polarized along the <100> axis of the sample, with a fluence of 75 mJ/cm² and a wavelength of 1300 nm onto the monodomain region. This allowed us to monitor the dynamics of photo-magnetic switching. A defocused probe pulse with a wavelength of 650 nm, which uniformly illuminated the observed area of the sample on the CCD camera, was introduced with a controlled delay relative to the pump pulse, providing insight into the spatiotemporal dynamics. The utilized geometry, resulting in single-domain switching, is depicted in Figure 4.1c.

The obtained experimental data, presented in the form of a differential image stack, is shown in the top panel in Figure 4.2 for specific time delays Δt. The intensity in each image, represented in grayscale, corresponds to the local out-of-plane component of magnetization M_z acquired through the magneto-optical Faraday rotation. The dynamic changes probed over time within the pump laser spot allowed us to track the evolution of the switching process.

Below, to highlight the mutual spatiotemporal behavior of the change in magnetization orientation from normal direction [001], the data is represented character in a three-dimensional manner. The 3D map was created using intensity profiles from a stack of 150 differential images acquired during a single-shot pump and probe experiment. The region selected for extracting the intensity profiles from the cross-section of the stack is marked by a yellow dashed rectangle in the first image of Figure 4.2. The selection of the rectangular profile with a width of 10 µm instead of a single line helped to improve the signal-to-noise ratio by averaging the signal spatially. The color code employed in the 3D map corresponds to the out-of-plane magnetization component, which was normalized to the Faraday rotation.

The 3D map illustrates ultrafast photo-magnetic switching in a single domains in YIG:Co. The observed transition occurs between states (1) and (8), which can be translated to the monodomain states M- and M+ respectively. The switching mechanism is identical to the one previously discovered and described in the publication [9].

Before pumping, the magnetic anisotropy in the initial state can be characterized by its intrinsic parameters, with a predominant cubic anisotropy and a minor uniaxial contribution. The magnitude of the short-lived photo-induced component is comparable to the combined intrinsic anisotropy. This noticeable change can lower the energy barrier, facilitating the switch in magnetization to the final state. However, the presence of significant damping suppresses the photo-induced anisotropy within a time span of less than 60 ps at room temperature. This time value corresponds to a quarter of the period of the laser-induced precession, which represents the quickest path for magnetization to transition between the two states.

Both the angle of the precession cone, guiding the magnetization from the initial to the final state, and the damping, are closely dependent on the fluence of the pump light. [49] On the other hand, due to the Gaussian shape of the incident pump beam, the observed monodomain switching is influenced by the spatial intensity profile. This implies that the central point of the illuminated spot is affected by a greater effective

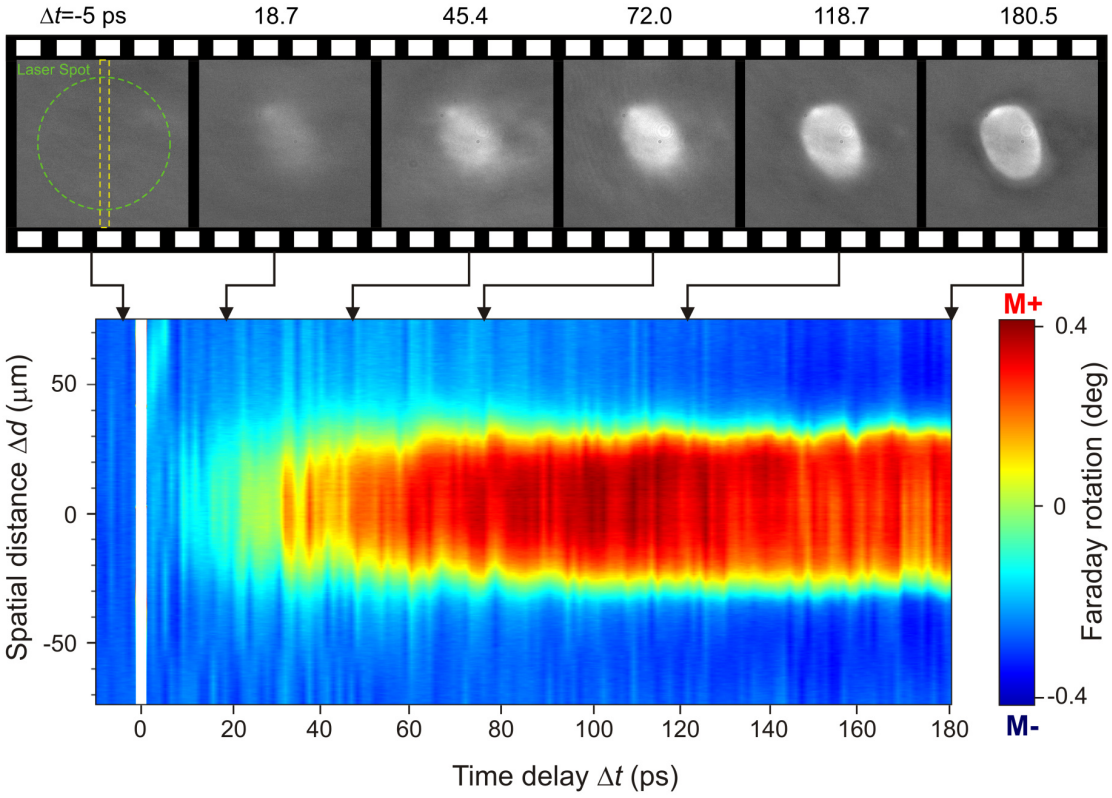

Figure 4.2: Single-shot time-resolved imaging of single state switching in YIG:Co represented in the form of an image stack, which is then transformed into a three-dimensional representation. A distinct blink, observable during imaging, precisely defines the overlap position of the pump and probe at $\Delta t = 0$ ps. The color code in the 3D diagram and intensity in the image stack corresponds to the Faraday rotation. The deep blue color represents the initial magnetization state (1) M−. The green color corresponds to the magnetization aligned in-plane, while the red color indicates the area switched to state (8) M+. The yellow rectangle in the top panel indicates the ROI used for determining mapped profiles.

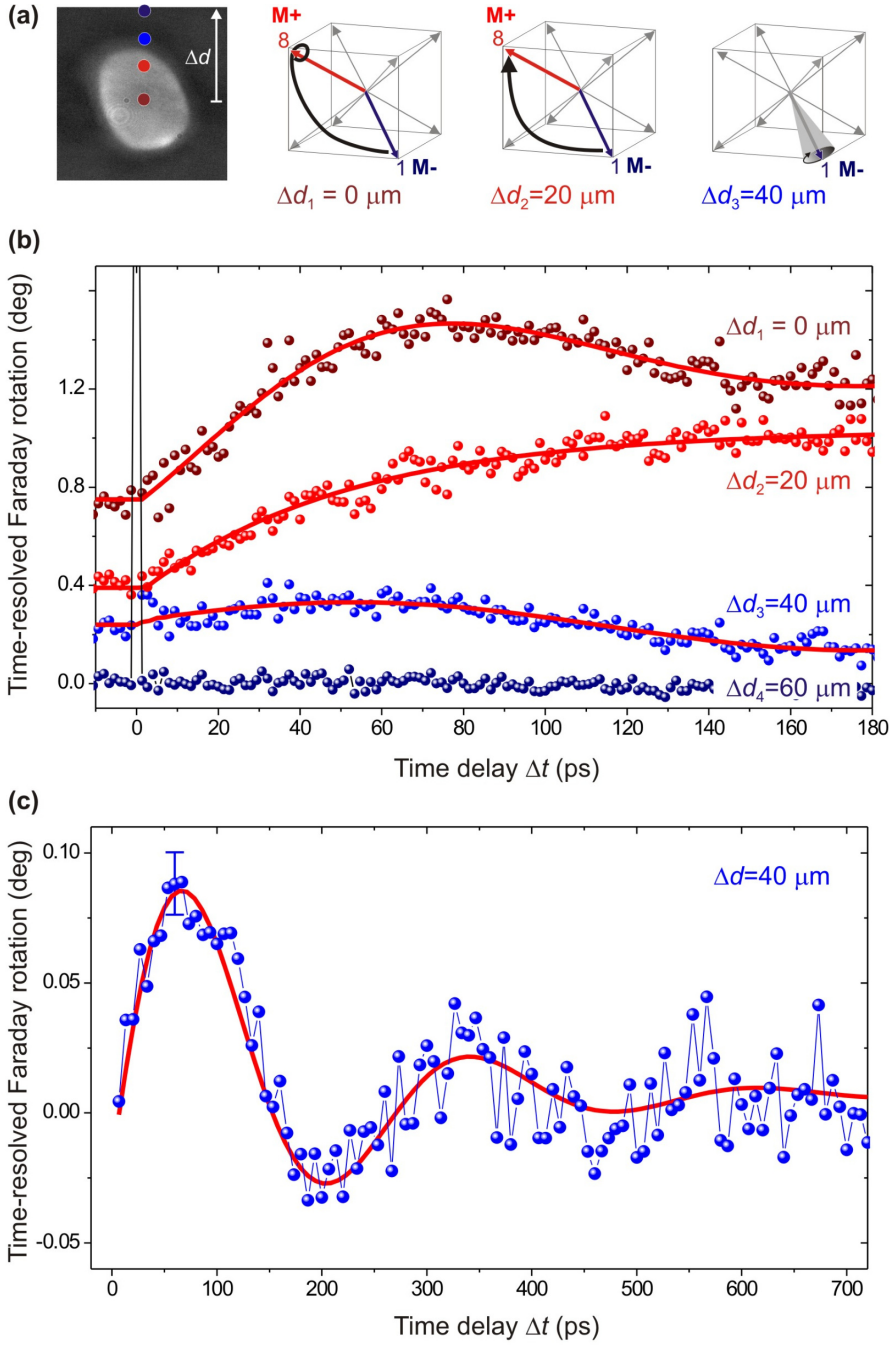

Figure 4.3: a) Selected RoIs shifted from the center by Δd distance marked in the time-resolved image. Chosen Δd values illustrate different scenarios of magnetization dynamics b) Time-dependent behavior of the M_z magnetization component for selected regions of interest in YIG:Co. The curves are vertically offset. Red solid lines represent fits using the damped sine function (Equation 3.21) c) Obtained magnetization precession for Δd = 40 μm. In long time-scale presenting the full precessional signal obtained through single-shot imaging measurements.

field of photo-induced anisotropy than the edges. The shape of the intensity profile is determined by the pump beam focusing, which defines the maximum spot size, and the average energy in the pump pulse, as measured by the optical power meter. Moreover, it should be noted that any local nonuniformities of the pump beam generated during its generation and guiding to the sample can impact the profile.

By analyzing the change in intensity (grey level) in the image (e.g. the horizontal cross-section of the 3D diagram in Figure 4.2 for spatially distributed regions of interest), one can distinguish the temporal changes in the amplitude of the photo-induced anisotropy field. From the presented data, as shown in Figure 4.3, four characteristic regions with distinctive behaviors of the magnetization vector become apparent. Selected regions of interest, were formed as a circle with a constant diameter of approximately 10 µm. Starting from the center of the switched spot, the region of interest was successively shifted beyond the spot by a defined distance Δd. The mean intensity value extracted from each region was used for further analysis. The decision to select a larger region, rather than individual pixels, aimed to diminish the impact of noise, although at the cost of insignificantly reduced spatial resolution. All presented regions of interest are indicated in the inset image in Figure 4.3a, with corresponding colors matching the plotted lines. Sequentially beginning from the farthest point:

- For $\Delta d > 60$ µm, the selected region remains unaffected by the pump pulse. Regardless of the pump beam power, no change in magnetization could be observed here. This region serves as a background region which during the measurements should be completely flat. All observed variation in the background defines the noise figure.

- For $\Delta d = 40$ µm, the analyzed region overlaps with the edge of the pump pulse. The local fluence still remains below the switching threshold. However, the pump beam influences the magnetization dynamics in the sample, inducing precessional motion over state M- (1). By enhancing the average power of the pump beam while maintaining the same focus, it might be possible to induce switching in this region. Although the small amplitude of induced intensity changes may not be evident in raw images, they can be accurately traced through a profile analysis. The precessional motion of the magnetization observed through the single-shot imaging technique can be compared with the signal obtained using the regular pump-and-probe measurement with an auto-balanced diode. The comparison of data obtained using the two methods is presented in Figure 4.3b, defining the time-resolved Faraday rotation sensitivity of time-resolved imaging as 30 mdeg for the 7.5 µm garnets, which can be scaled to about 4 mdeg/µm. Single-shot imaging accurately determines the phase and frequency of the small precessional movement of magnetization, making it a perfect complement to the classical pump and probe measurement method.

- For $\Delta d = 20$ µm and smaller, the local intensity exceeds the threshold value, supporting the magnetization switching from M- (1) to M+(8) state, thereby reversing the out-of-plane magnetization component. This behavior is also applicable to the region of interest covering and averaging the entire switched spot. Previously, this region was used to determine switching dynamics [9]. However, due to inadequate resolution and magneto-optical contrast, the spatial dependence was completely obscured.

- For the center of the spot Δd = 0 µm, the local fluence achieves the highest value. Here, the photo-induced anisotropy field is sufficiently large, resulting not only in switching between M- (1) and M+ (8) states, but also in a damped precession over the final M+ (8) state after about 60 ps. The amplitude of this precession corresponds to the ferromagnetic resonance mode, remaining small and keeping the magnetization at the switched state. Although this effect was predicted [50], it is being observed experimentally here for the first time.

The nature of photo-magnetic switching in a single state, despite being the simplest case, is not devoid of nuances. Its spatiotemporal characteristics, described in this section, are influenced by the intensity profile of the incident pump pulse. Changes in intensity affecting the photo-induced anisotropy field can alter the switching trajectory, leading to temporal variations or different types of magnetization motion. The use of a light source with flat-top pulses could potentially mitigate spatial disparities in behavior.

4.2 EFFICIENCY OF PHOTO-MAGNETIC SWITCHING IN MULTI-DOMAINS

Translating the region of interest from Figure 4.1 to the area where two domain states coexist opens up another scenario for examining multi-state switching. In contrast to the monodomain scenario, the presence of small labyrinth-like domains, can lead to uneven distribution across the sample, resulting in varied shapes and spatial arrangements. Consequently, the nature of the initial state can be modified by applying an external in-plane magnetic field to the YIG:Co sample.

For instance, if the initial domain structure was induced by a magnetic field applied along the [110] axis in YIG:Co, the entire sample can be switched by a magnetic field of approximately 20 Oe along the [1-10] axes. During this switching process, the shape of the small domain structures should be preserved due to the shape memory effect.[120, 121] This effect is caused by magnetization-induced anisotropy, particularly influenced by the anisotropic cobalt ions. The presence of local domain walls serves as a typical stabilizing element. Furthermore, in this specific case, the non-colinearity of magnetization vectors in neighboring domains generates a "volume" memory carrier that functions as a component maintaining the shape integrity during switching.

Applying excessive external magnetic fields can lead to the growth of labyrinth-like pattern domains or the contraction of certain regions into separate bubble domains. This offers the possibility to arrange diverse spatial configurations, such as regular arrays or patterns. An illustrative image showing the switching of a multi-state configuration involving both bubble and labyrinth-like domain shapes is presented in Figure 4.4.

The arrangement of domains in both the initial and final states follows the garnet symmetry. The initial state consists of the large state M_8 along the [1-11] axis and M_4 along the [1-1-1] axis. Following the switching process, which can be triggered either by a magnetic field or a single light pulse, domains realign along the M_1 parallel to [11-1] and M_5 parallel to [111] axes. It is important to highlight that again both the large and small states undergo changes in their out-of-plane and in-plane magnetization components during the switching.

Contrasting the previous subsection, where the monodomain state was discussed, this section focuses on the behavior within the small domains. Here, the initial state of the large domain is reversed, accompanied by altering the plane of the incident pump light

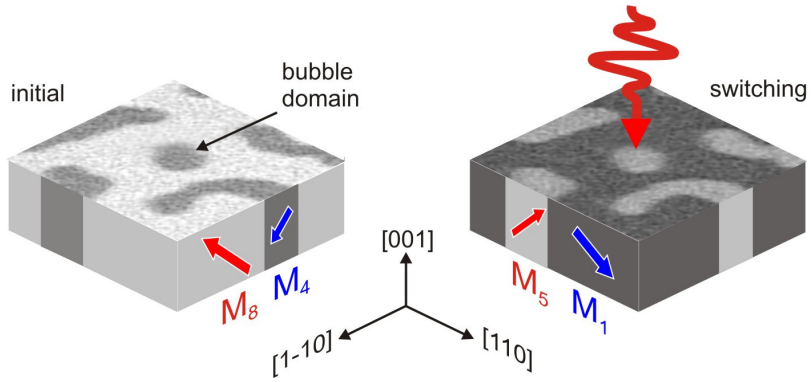

Figure 4.4: The exemplar structure of a YIG:Co sample showing the geometry of a mixed multi-state containing labyrinth-like and bubble domain switching case. Such switching can be obtained either globally by applying a magnetic field of 20 Oe along the [1-10] axis or locally using a single light pulse. Both large domain M_8 and small domain M_4 can be switched simultaneously to M_1 and M_5 respectively.

to orthogonal. A comprehensive description of available trajectories and torque control enabling precise state transitions will be explored in Chapter 5.

To investigate the mutual behavior of photo-magnetic switching in large and small domains, we focused on the final state within the time-resolved experiment. This approach helped eliminate slower magnetostatic processes that could affect and revert the switched domain. To obtain this, as shown in Figure 4.5a, the initial image and differential time-resolved images captured Δt= 1 ns after pump pulse was presented for various fluences. Throughout the series, the pump beam's focus giving a pump diameter of 120 µm was maintained. Fluence increase was achieved by raising the optical power of the beam through a reduction in the number of gray filters along the beam path. Importantly, the pump beam's spatial intensity distribution follows a Gaussian shape once again. The fluence values correspond to the pulse energy delivered to the entire illuminated area.

Switching efficiency, quantified as the normalized switched area, is summarized in Figure 4.5b. While the switched area for large domains is evident, for small labyrinth-like domains, the switched area aligns with the pattern envelope. Three distinct regions characterized by different fluence levels of the pump beam are apparent.

- For fluences below I<17 mJ/cm^2, no consistent switching patterns were observed. These fluence values are insufficient for switching, yet they perturb the magnetization from equilibrium, causing it to precess over the initial state. Although this precession can be observed on the shortest timescale, it vanishes completely before Δt = 1 ns.

- Higher fluences, ranging up to 40 mJ/cm^2, begin to induce switching. However, as seen in Figure 4.5a, these changes are noticeable only in the small labyrinth-like domains. This implies that photo-magnetic switching solely occurs between small domain states M_4 and M_5 in this region. The switched area's range depends on the spatial alignment between the pump beam and the initial distribution of small domains. The switched area expands with increased fluence, being surrounded by a larger portion of the pump beam beyond the intensity threshold.

- Further increase in fluence starts to impact not only small domains but also large ones. Crossing the threshold fluence > I_L allows for switching between the large

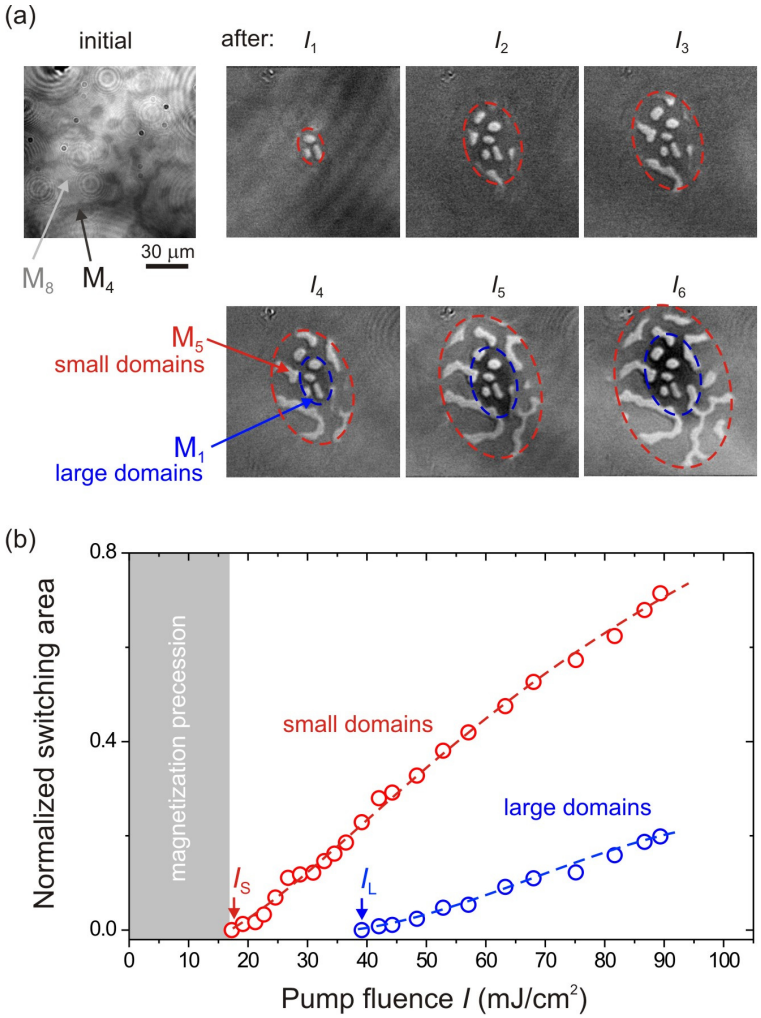

Figure 4.5: a) Illustration of an initial magnetic structure featuring states M_8 (large white domains) and M_4 (small black domains), followed by differential time-resolved images captured at Δt = 1 ns after pump irradiation, with varying pump fluences. The presented fluence values correspond to I: I_1 = 20, I_2 = 30, I_3 = 40, I_4 = 50, I_5 = 75, I_6 = 90 mJ/cm^2. Dashed envelopes delineate regions where switching is observable. b) The normalized switching area for both small and large domain types.

states M_8 and M_1. This scenario results in simultaneous switching within both domains, indicating a multi-states switching regime.

The emergence of distinct regimes with varying threshold energies can be attributed to the different types of magnetization trajectories within the two domain categories, which will be discussed in detail in Chapter 5. Because the angle between the switched states is determined by the extent of cubic and uniaxial magnetic anisotropies, by adjusting the mutual balance of these internal magnetic anisotropies, it becomes feasible to regulate the threshold energies and consequently the size of the fluence gap.

The ability to control these switching regimes, achievable by manipulating the pump power, presents an intriguing prospect from an application standpoint. Laser fluence control introduces an additional degree of freedom of possibilities for modulating the final magnetization state.

Considering that adjusting the fluence allows for the possibility of exclusively switching small domains in such garnets, we explored the potential of switching a single bubble domain using single pump pulse. The idea of "isolating" a single bubble for magnetization switching is directly linked to practical applications, as a bubble is the smallest domain size that can be sustained on the magnetic sample.

Historically, the concept of utilizing a magnetic bubble to store one bit of information was extensively investigated during the 1960s and 1970s, leading to numerous commercial applications.[64, 122–124] At that time, orthoferrites and magnetic garnet films were identified and selected as suitable materials for such devices.[64] In this approach, the presence of a bubble signifies a binary "1", while the absence of the bubble signifies a binary "0". Bubbles can be organized in fixed arrays or allowed to propagate freely in space. A single bubble can be generated from the stripe magnetic domain or thermally generated, eliminated, captured, and manipulated using a laser beam. [125]

The recent resurrection of interest in the investigation of magnetic skyrmions [126] has also directed attention towards magnetic bubbles, which can be viewed as their topological equivalent [127, 128]. The stabilization of nano-sized bubble domains in ferroelectrics with polar topologies, such as vortices and skyrmions, has been achieved in thin films [129] and more recently in bulk materials, leading to the creation of multi-conformational domain structures exhibiting significant electromechanical activity and a plethora of physical properties.[130] Skyrmion bubbles formed from stripe domains [131, 132] present an ideal platform for studying the Dzyaloshinskii-Moriya interaction. Moreover, the ability to manipulate these bubbles using magnetic fields [124], electric current/field [133], and continuous light [125] substantially broadens their potential applications.

To explore the feasibility of exclusive bubble-based switching, we targeted a region pre-patterned with bubble domains. By utilizing the character of a Gaussian profile of the pump beam and optimizing the interplay between beam focusing and localization, we managed to tune the peak fluence level to go just above the threshold value I_s required for initiating magnetization switching. The threshold effect is visualized in Figure 4.6a and b in which a slight increment in peak fluence facilitates switching between M_4 and M_5 states solely within a single bubble. As the pump fluence is further elevated, the area under the influence of switching broadens, impacting nearby bubbles. Notably, the pump beam diameter of 80 µm substantially surpasses the dimensions of the switched spot. This specific beam profile was formed to ensure that only the peak intensity goes beyond the I_s threshold, of approximately 18 mJ/cm^2. Translating this fluence value to dissipation in used YIG:Co with 12% absorption at 1300 nm and thickness of 7.5 µm correspond to only 2.9 J/cm^3 heat load, which is about half of what was demonstrated previously. [9]

Subsequently, to investigate the dynamics of the switched bubble domain, a time-resolved experiment was undertaken with varying delay time Δt. Employing identical conditions that facilitated the single bubble switching, we captured a stack of 150 single-shot pump and probe images, mirroring the approach in Figure 4.2. Illustrative MO images, presenting the initial structure with an induced bubble pattern, are displayed in Figure 4.7a. Here, the switching process starts from the initial bubble domain state M_4, visually depicted in black area, and progresses to state M_5, characterized by white area. In the final state, the contrast becomes indistinguishable compared to the larger white domain, as the out-of-plane magnetization component attains the same magnitude. The dynamics of switching, apparent as intensity changes, can be much easier distinguished from differential images presented in Figure 4.7b.

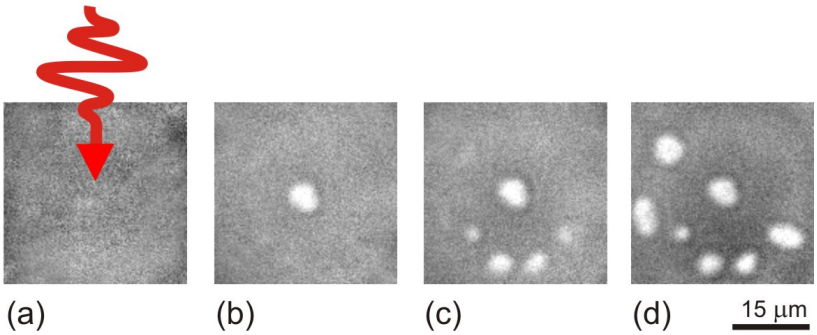

Figure 4.6: Differential images presenting magnetic bubbles switched by a single pump shot with an 80 µm diameter. The initial domain pattern of magnetic bubbles was predetermined. Through pump fluence control, the switching area extends from a) no switching, to b) switching of a single bubble, and further to c) and d) where multiple bubble domains undergo switching.

Spatio-temporal characteristics of photo-magnetic switching are presented in Figure 4.7c in the form of a three-dimensional graph. The central region of this graph, transitioning from blue to red, signifies the switching of a single bubble domain with a size of approximately 5 µm. Just beyond this region, the sub-switching photo-magnetic precession can be noticed only. The characteristic area of green color represents the increase of the magnetization precession to its maximum during the first quarter of oscillation.

Analogously to the monodomain switching case, Figure 4.7d displays individual cross-sections that illustrate the dependence of Faraday rotation changes as a function of the distance from the center and, consequently, the beam intensity. In this scenario, magnetization switching only occurs within the domain of the M_4 magnetization state. Just beyond this region, within the M_8 domain area, only precessions with variable amplitudes can be observed. These precessions vary depending on the strength of the effective anisotropy field.

By using the time-resolved single-shot imaging technique the ultrafast dynamics of the labyrinth-like or bubble domain states in YIG:Co was experimentally checked for the first time. Experimental findings confirm the picosecond-scale dynamics of switching within labyrinth-like domains. Moreover, by optimizing both the pump fluence and the focusing conditions the least-dissipative ever ultrafast magnetization switching of a single bubble-domain was achieved. Notably, the intensity threshold necessary for effecting the switching of this isolated bubble is merely half that required for the multi-domain magnetization switching.

To achieve a further reduction in the dimensions of the switched domain within the dielectric material, it is essential to engineer both the magnetization anisotropy of the material and the garnet thickness down to the nanoscale level. By utilizing the concept of bubble domain switching through the photo-magnetic effect with the currently intensified research in the field of skyrmions, numerous potential applications can be anticipated, extending well beyond cold data storage.

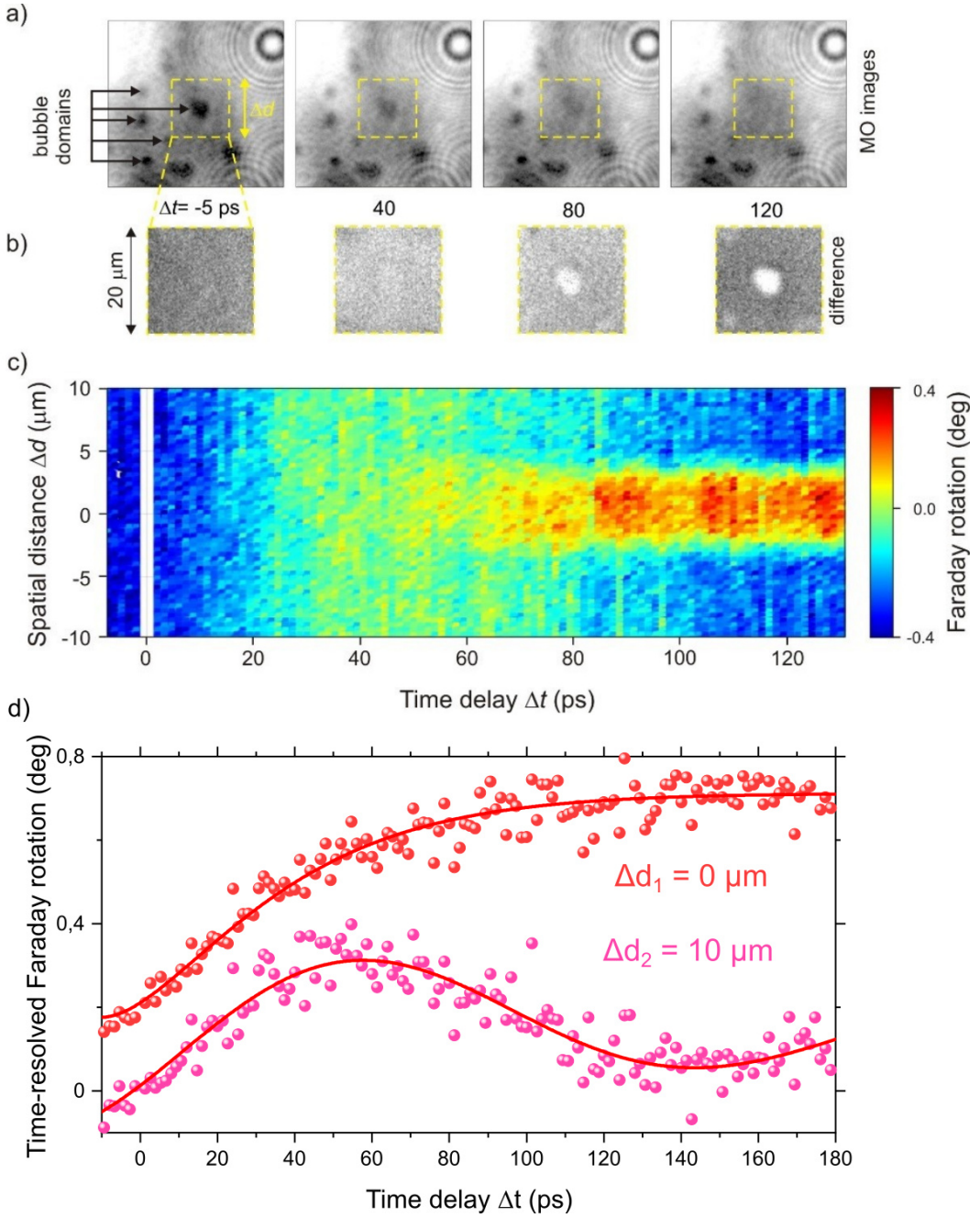

Figure 4.7: The time-resolved stack of images presenting magnetization switching within a single-domain bubble. a) Initial bubble pattern displayed in raw MO images. b) Differential images emphasizing the single-domain switching. c) Three-dimensional spatiotemporal diagram, analogous to Figure 4.2, illustrating the switching dynamics from state M_4 to state M_5 within a singular bubble domain. d) Selected traces for RoIs shifted from the center by a distance Δd. The curves are vertically offset. Outside the switched bubble domain ($\Delta d > 5$ µm), only precession with varying amplitude can be observed.

5

NON-RECIPROCITY OF NONTHERMAL PHOTO-MAGNETIC SWITCHING

Given that the investigated garnet exhibits cubic symmetry, resulting in a complex multi-state nature of the photo-magnetic switching, a more in-depth analysis of its dynamics becomes essential. In the previous Chapter 4, it was demonstrated that the energy of laser pulses required to switch between different states (domains) can vary. This leads to the hypothesis that the difference in the switching threshold may be related to different trajectories of magnetization vector motion. Immediately, questions arise as to whether the trajectories of magnetization motion are symmetric concerning the direction of the polarization vector. Overall, the laser-induced simultaneous manipulation of magnetic moments in a multi-state switching scenario is influenced by the interplay between topology, crystal symmetry, and the free energy landscape. Examining the influences of these factors will enable us to understand multi-state dynamics more comprehensively.

In this Chapter, by experimentally and computationally examining the differences in switching trajectories, we highlight the non-reciprocal nature of photo-magnetic switching, where the choice of the switching path is determined by the interaction between the photo-magnetic torque and magnetic anisotropy. Initially, we will discuss distinct coherent magnetization precession at the magnetic domains and the magnetization switching trajectories, which depend on both the directions of linear polarization of the laser and the initial magnetization states in garnets. Next, by employing the Landau-Lifshitz Gilbert formalism, we will introduce the tensor of photo-magnetic symmetry, revealing that the non-reciprocal dynamics is triggered by a sign change in the photo-magnetic torque. Finally, we will present a framework and the results of numerical simulations that model the experimentally obtained trajectories.

The results discussed in this chapter have been submitted as a preprint in:

T. Zalewski, V. Ozerov, A. Maziewski, I. Razdolski, A. Stupakiewicz "Non-reciprocal coherent all-optical switching between magnetic multi-states", *arXiv:*2308.12771 (2023).

5.1 PHOTO-MAGNETIC DYNAMICS OF COHERENT MULTI-STATE SWITCHING

The ultrafast nonthermal all-optical switching of magnetization in garnets has primarily been studied in the context of single-state (between two states of magnetization in the single domain) switching. However, YIG:Co film has four easy magnetization axes that can enable multi-state coherent switching in different domains using linear polarization laser pulses. In such cases, the ability to control light-induced torque becomes crucial for achieving controllable changes between multiple magnetization states and trajectory selectivity.

Although all-optical magnetization switching has been demonstrated in a wide range of magnetic materials, manipulating torques using polarized light remains a challenge. Recent research has shown that ultrafast torque control can be achieved through various modulation mechanisms, including current modulation in spin-orbit torque systems [134–137], the use of ultrashort acoustic pulses [138–142], and utilizing coherent phonon-magnon coupling [52, 143–147]. Among these methods, the ability to manipulate multiple magnetization states solely using laser pulses holds tremendous potential for future technologies. All the results presented in this chapter were obtained using YIG:Co sample no. 705, the same sample in which ultrafast photo-magnetic switching was first demonstrated [9].

To deepen our understanding of the dynamics of multi-state switching, as discussed previously in Chapter 4, we conducted a series of dynamic measurements to monitor laser-induced dynamics in all domain states. For this purpose, initial domain phases, as shown in Figure 5.1, containing M_4 and M_8 states and with M_1 and M_5 states, were illuminated by a pump pulse with polarization aligned either with $E\|[100]$ or $E\|[010]$. All possible domain states can be induced by applying an in-plane magnetic field of about 20 Oe directed along one of the four [110] axes [77]. The multi-domain magnetic structure was achieved by applying an external magnetic field from two orthogonally mounted coils. Initially, an 800 Oe magnetic pulse in the [1-10] direction induced states M_8 and M_4 in the entire sample. Subsequently, a 20 Oe pulse along the [110] direction from the second coil converted a part of the phases to 1 and 5 states, inducing the coexistence of all phases in the form of well-separated stripes.

To initiate photo-magnetic precession in magnetic domains of the YIG:Co film with a 4° miscut angle, we used a low pump fluence <10 mJ/cm² below the switching threshold. These experiments were conducted using the pump-probe setup described in Chapter 3.3.4, which allowed us to obtain magnetization precession data for each state and polarization, as shown in Figure 5.1. The data were fitted with a damped sine function using Equation 3.21.

The presence of precession in domains without an external magnetic field confirms that the dynamics are coherent and depend on the initial magnetization orientation and/or the direction of linear polarization of the precession excitation laser pulse. Therefore, due to the cubic symmetry, it is possible to distinguish between eight possible directions of magnetization and two directions of the polarization vector.

Analogous to the results presented in Chapter 4.2 for the pump fluence $I > I_L$, we achieved multi-domain switching for the magnetic phase containing initial states M_4 and M_8, as indicated in Figure 5.2a. The switching dynamics were observed using the time-resolved single-shot imaging setup described in Chapter 3.3.5. The stack of exemplary time-resolved differential images of the magnetization projection M_z, excited by a pump with polarization $E\|[100]$, is shown in Figure 5.2. The switching of large domain states

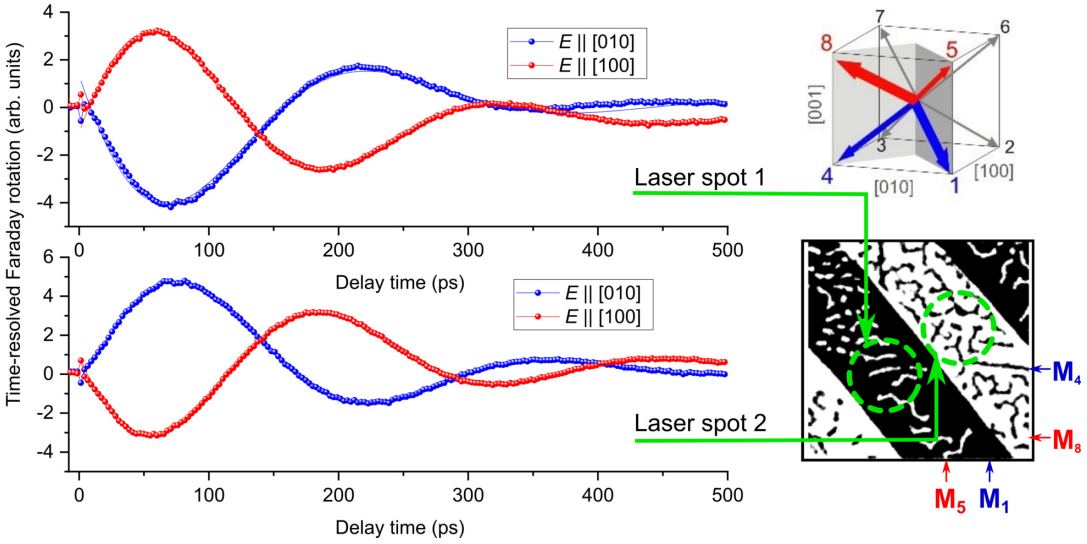

Figure 5.1: Image of the initial multi-phase magnetic domain structure in YIG:Co with a 4° miscut angle and time-resolved precession of magnetization in domains. The presented magnetization precession was measured in two separate regions marked by the 'laser spot,' where a combined domain containing large and small domains exists. In both cases, the measurements were performed for the pump beam with polarization along the [100] and [010] directions in YIG:Co.

M_8 to M_1 is marked by a decreasing in brightness, while the switching of the small domains between states M_4 and M_5 is indicated by increasing in brightness. Grey values represent no pump-induced out-of-plane magnetization changes, indicating zero signal. It's noteworthy that the pattern of the small domains remains constant throughout the experiment, confirming the nonthermal nature of the photo-magnetic switching. The differentiation with the background images enhances the signal-to-noise ratio but conceals the initial magnetic structure. Only changes in magnetization are tracked. After each switch, the initial domain structure was restored by the coil system generating the external magnetic field pattern. Time-resolved imaging was performed using the pump at a wavelength of 1300 nm and fluence of about 50 mJ/cm².

To understand this behavior, we focus on the dynamics of a single magnetic phase. By analyzing changes in the signal from non-differential time-resolved images, instead of the differential signal $\Delta M_z(\Delta t)$, we can obtain the initial and final state positions leading to the $M_z(\Delta t)$) signal. Such a trace, illustrating the switching of M_8 to M_1 and M_4 to M_5 states with $E\|[100]$ pump pulses, is shown in Figure 5.2d, along with an accompanying sketch in Figure 5.2c that illustrates the rotation of magnetization pairs in adjacent domains (indicated by red and blue arrows). The transient variations in the angle between magnetization vectors are linked to the inequality of the two trajectories, resulting in different switching times.

We note that after about 30 ps, the magnetization, which initiates its dynamics from the M_1 direction, reaches a transient perpendicular state to the sample plane. This is in contrast to previously reported magnetization switching between states in YIG:Co via the in-plane direction [9]. We note that the angle between M_4 and M_8 is governed by the magnetic energy landscape at room temperature. Due to the lack of substantial laser-

induced heating, the energy potential and angular distances between all energy minima remain unchanged.

We repeated the experiment for a subsequent initial magnetic phase containing states M_1 and M_5 and for the beam with orthogonal polarization of $E\|[010]$. In total, similar measurements were conducted for all 8 different magnetic states. For each state, we selected appropriate regions of interest within the borders of individual domains and integrated the variations over them, resulting in a set of traces corresponding to the laser-induced changes. These traces can be then normalized to the static Faraday rotation or to the change of the out-of-plane magnetization component ΔM_z and plotted as a function of the optical delay between the pump and probe pulses, Δt. Analyzing the temporal behavior of spatially defined RoIs in the image corresponding to one of the domain states allowed us to distinguish the magnetization trajectories in each domain independently. By selecting the ROI position and size, we achieved simultaneous probing of spatially averaged ΔM_z changes, enabling precise separation of the magnetization dynamics in different domain states. To account for the spatial dependence of the photo-induced anisotropy strength originating from the Gaussian pump beam profile (Figure 5.3a), the analyzed RoIs in the domains were manually chosen to have the same size and to be located close to each other. The obtained traces for all cases are summarized in Figure 5.3b and c.

Taking into consideration the studied garnet's absorption of 12% (a_λ = 0.12) at 1300 nm, a molar mass of m = 706 g/mole, a heat capacity C = 430 J/mole, thickness of d = 7.5 µm, and density ρ = 7.12 g/cm^3 (sample no. 705), we estimated the energy q of local laser-induced heat load to the sample as:

$$q = a_\lambda I = \Delta T C \rho d / m \tag{5.1}$$

The measured average pump fluence was I = 50 mJ/cm^2, which corresponds to a peak value of 100 mJ/cm^2 for a centrally located RoI. This resulted in an approximate temperature change ΔT of 4 K, as indicated in Figure 5.3a.

Additionally, we compared the dynamics of magnetization precession using our spatially-resolved time-resolved imaging method (Figure 5.3d) to that obtained with the conventional pump-probe technique (with spatial averaging) shown in Figure 5.1. Both measurement methods yielded highly consistent results. However, using time-resolved imaging, we were able to retrieve data for small domains.

The obtained traces, presented in Figure 5.3, reveal their surprising asymmetry and can be classified as either type I or type II, depending on the initial magnetization state and pump polarization.

In Figure 5.4a, we expand these results to include traces for orthogonal pump polarization. The inequivalence of these trajectories becomes strikingly apparent. This observation is highly surprising considering the fourfold crystalline symmetry and magnetic anisotropy of the garnet.

To understand the physical origins of the dissimilarity between the two trajectories $M_{E\|100}(t)$ and $M_{E\|010}(t)$, we decomposed them into even and odd contributions: $M_{(e,o)}(t) \equiv \left(M_{E\|100}(t) \pm M_{E\|010}(t)\right)/2$. Because there are only two unique trajectories, these $M_{(e,o)}(t)$ show the same dynamics for every pair of magnetization states topologically connected with a pair of switching trajectories. These are shown in Figure 5.4b with green and black data points, respectively.

Notably, the even part closely resembles the averaged over multiple domains, step-like switching trace previously reported [9]. By 100 ps, the switching is already completed,

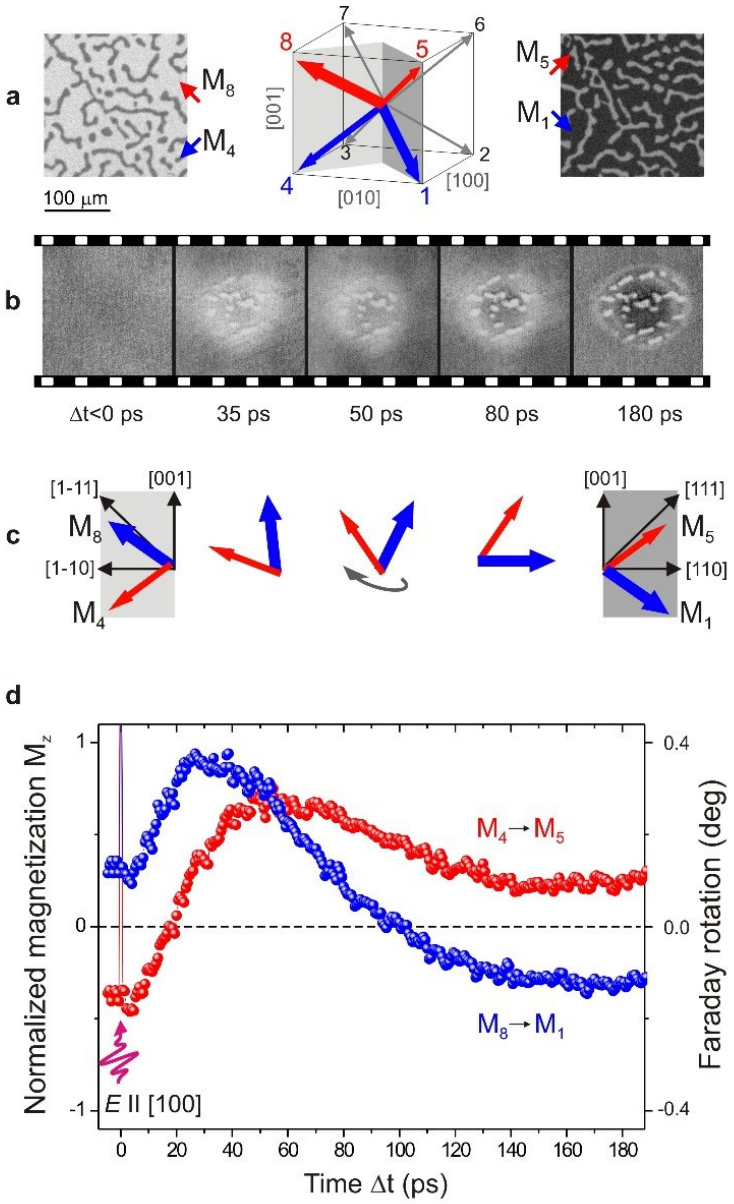

Figure 5.2: a) Images of multi-state magnetic domain structure and orientation of easy magnetization axes in YIG:Co films. b) The differential stack of time-resolved images illustrating the transient dynamics of photo-magnetic switching in YIG:Co. The experiment involved the use of a 50 fs single pump pulse with and polarization along E|| [100] direction in the garnet. c) The sketch illustrates the motion and rotation of magnetization at domains for different delay times Δt. d) The normalized out-of-plane component of magnetization M_z for the simultaneous switching between four magnetic states (M_8 to M_1 and M_4 to M_5).

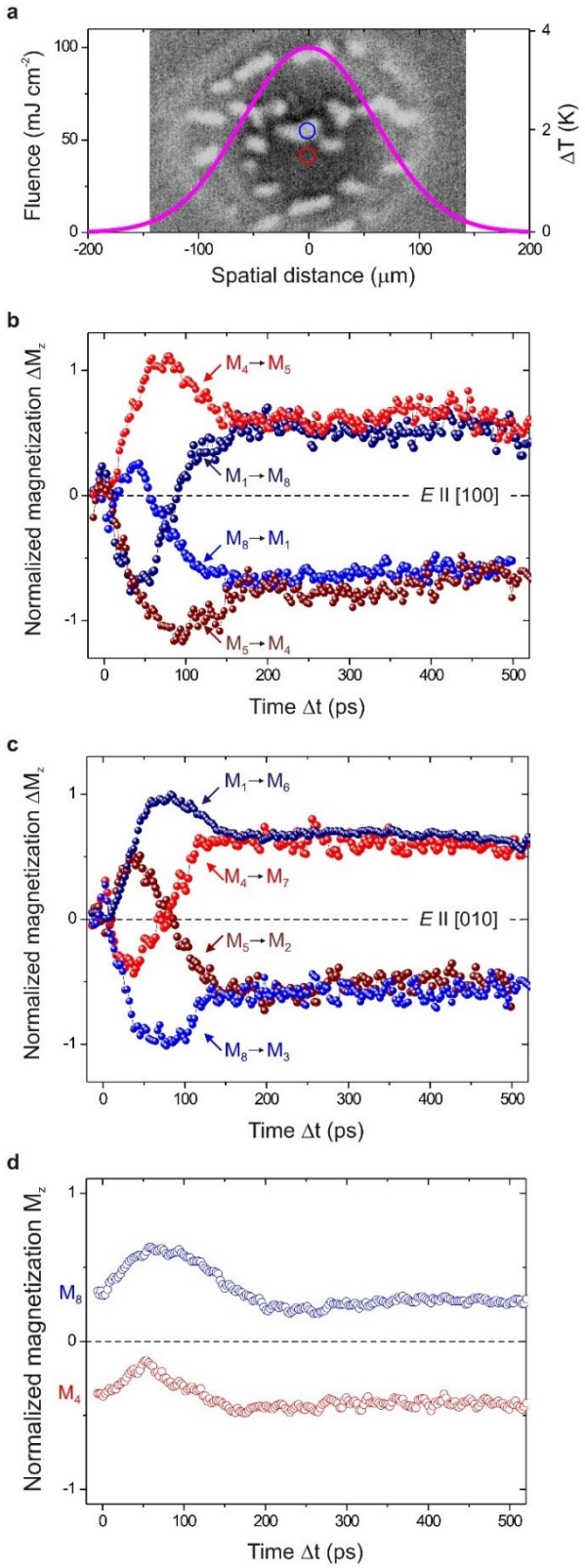

Figure 5.3: Dynamics of magnetization reversal between all states in YIG:Co. a) The pump intensity profile measured with a beam profiler resulting in the spatially inhomogeneous field of photo-magnetic anisotropy. The red and blue circles indicate RoIs in the two domains chosen for the subsequent analysis. The right vertical axis indicates the calculated spatially-resolved laser-induced heating. b) The normal component of magnetization ΔM_z for all different magnetic states illuminated with $E\|[100]$ or c) $E\|[010]$ pump polarization. d) The magnetization precession in the initial states (M_4 and M_8) at a pump fluence of 10 mJ/cm² below the switching threshold.

and the remaining variations are related to the relaxation of magnetization within the corresponding potential minimum. On the other hand, the odd part exhibits a strongly damped oscillatory character, highlighting the precessional character of the switching dynamics in general. It is the odd contribution that is responsible for the non-reciprocal switching seen in Figure 5.4a, thus the switching along the M_4 to M_5route and back proceeds along different trajectories.

We argue that the odd, non-reciprocal contribution can be understood as a fingerprint of the interplay between torque symmetry and coherent magnetization dynamics. In this context, coherence implies that individual magnetic moments in all simultaneously stimulated states behave in a coordinated manner, maintaining a consistent phase relationship during the spin dynamics. The solid line in Figure 5.4b represents the (scaled) time derivative of the even contribution. Its striking similarity to the odd part suggests that the latter originates in the precession of magnetization when moving along the switching route. This results in the emergence of the orthogonal component $\frac{dM}{dt}$ since $\left(M \cdot \frac{dM}{dt}\right) = 0$. The sign of this orthogonal component is governed by the direction of movement along the switching route, thus giving rise to the odd contribution to the magnetization dynamics. In other words, a new curvilinear reference frame can be introduced where the even contribution depicting the genuine switching route is bereft of any rotational part. In such a reference frame, the LLG equation will be transformed accordingly, acquiring an additional term similarly to the mechanical equations of motion in a rotating reference frame. This additional term can be viewed as a fictitious magnetic field giving rise to the magnetization dynamics in the direction orthogonal to the switching route, or the aforementioned odd contribution. The characteristic shape of the normal projection of this contribution is then determined by the change rate of M_z along the switching route, in agreement with Figure 5.4b.

5.2 PHOTO-MAGNETIC TORQUE SYMMETRY

To get further insight into the laser-induced asymmetry of the magnetization switching trajectories, we performed a tensor analysis of the photo-magnetic excitation. In particular, the photo-magnetic Hamiltonian contribution reads:

$$\mathcal{H}_{p-m} = \hat{\beta} \boldsymbol{E}\boldsymbol{E}^* \boldsymbol{M}\boldsymbol{M} \tag{5.2}$$

where $\boldsymbol{E}$ is the electric field of the optical pump, and $\hat{\beta}$ is a fourth-order polar tensor responsible for the photo-magnetic susceptibility[50]. The microscopic origin of the photo-magnetic susceptibility tensor in Co-doped garnets is still insufficiently well understood. It is believed [9] that resonant optical excitation of the $d - d$ transition in Co ions effectively changes the orbital state and symmetry which has a strong impact on the magnetic anisotropy. In particular, the balance between the intrinsic cubic magnetic anisotropy and the uniaxial photo-induced anisotropy promoted by the Co ions in destroyed. This balance shift is conventionally described by an effective field of the photo-induced magnetic anisotropy or a photo-magnetic tensor $\hat{\beta}$, allowing for the permanent switching of magnetization $\boldsymbol{M}$ between different magnetic states with resonant, linearly polarized laser pulses $\boldsymbol{E}$.

Our analysis shows that the asymmetry of the trajectories is inextricably linked to the cubic symmetry of the photo-magnetic medium. In particular, for a considered reference frame aligned with the main crystal axes the analysis is substantially simplified by the

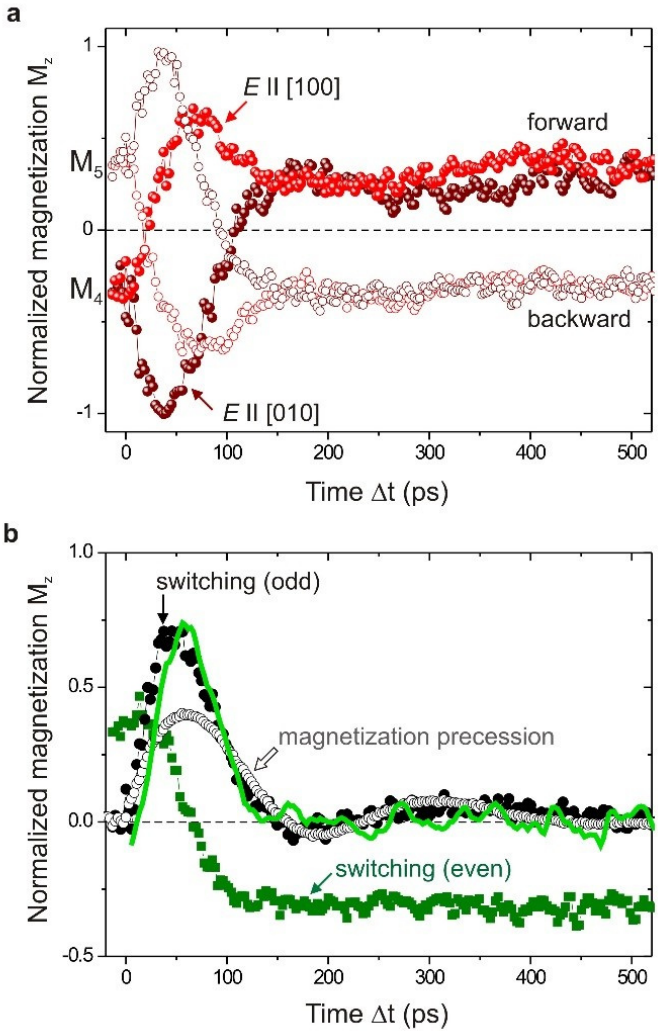

Figure 5.4: Non-reciprocal all-optical magnetization switching. a) Pump polarization effect on magnetization trajectory enabling selecting switching trajectory and final state for orthogonal orientation of laser pump polarization along [100] and [010] direction in YIG:Co film. b) The differential signal of switched states (close black points) compared to the measured magnetization precession (open points) below the threshold level of switching. The even and odd contribution of photo-magnetic switching. The green solid line is the scaled derivative of the even component of photo-magnetic switching.

normal incidence of the pump beam, that is, parallel to the (001) direction. In the initial state, magnetization $\boldsymbol{M}$ has all three non-zero components (M_x,M_y,M_z). Owing to the cubic $m3m$ symmetry of the non-distorted garnet and setting $E_x \| (100)$, $E_y \| (010)$, E_z=0, we can outline the following non-zero components of the photo-magnetic susceptibility tensor β:

$$\beta_1 \equiv \beta_{xxxx} = \beta_{yyyy} \tag{5.3}$$

$$\beta_2 \equiv \beta_{xyxy} = \beta_{yxyx} = \beta_{yxxy} = \beta_{xyyx} \tag{5.4}$$

$$\beta_3 \equiv \beta_{xxyy} = \beta_{yyxx} = \beta_{xxzz} = \beta_{yyzz} \tag{5.5}$$

The photo-magnetic excitation of spin dynamics is mediated by the effective photo-magnetic field $\boldsymbol{H_L} = -\frac{\partial H}{\partial M}$. It then exerts a torque T on magnetization, thus setting it into motion according to the LLG formalism: $\frac{\partial M}{\partial t} = -\boldsymbol{M} \times \boldsymbol{H_L}$.

At the initial stage directly after the laser excitation, under the action of the effective photo-magnetic field $H_{L,I} = -\beta_{ijkl} E_i E_j M_k$ the magnetization dynamics takes the following shape:

$$\frac{\partial M_x}{\partial t}|_0 = (\beta_3 - \beta_1) E_y^2 M_y M_z - 2\beta_2 E_x E_y M_x M_z \tag{5.6}$$

$$\frac{\partial M_y}{\partial t}|_0 = -(\beta_3 - \beta_1) E_x^2 M_x M_z + 2\beta_2 E_x E_y M_y M_z \tag{5.7}$$

$$\frac{\partial M_z}{\partial t}|_0 = (\beta_3 - \beta_1)(E_x^2 - E_y^2) M_x M_y + 2\beta_2 E_x E_y (M_x^2 - M_y^2) \tag{5.8}$$

which for, the out-of-plane laser-induced magnetization can be simplified to a:

$$\frac{\partial M_z}{\partial t} = \beta^{'} (E_x^2 - E_y^2) M_x M_y + 2\beta^{''} E_x E_y (M_x^2 - M_y^2) \tag{5.9}$$

where $\beta^{'}$ and $\beta^{''}$' are the linear combinations of the non-zero β components: $\beta^{'} \equiv (\beta_3 - \beta_1)$, $\beta^{''} \equiv 2\beta_2$.

Two main conclusions can be drawn from this result. First, consider the two initial magnetic states M_8 and M_4, as indicated in Figure 5.1, that is, with identical in-plane magnetization components but opposite out-of-plane ones, $M_z^8 = -M_z^4$. Without the loss of generality, we refer to them as the "up" and "down" states, although the choice of up and down directions is arbitrary. Then, since it is even with respect to M_z, the normal component of the magnetization dynamics $\frac{\partial M_z}{\partial t}|_0$ will be the same for these two states. In other words, the "up" state will get the momentum towards the final "down" state of the switching process, whereas the "down" state will start its motion in the direction away from its destination. It is thus seen that the asymmetry of the switching trajectories

is introduced immediately after the photo-magnetic excitation, and is governed by the tensor nature of the photo-magnetic effect and the cubic crystal symmetry.

Secondly, consider an excitation with linearly polarized light. Because the uniaxial anisotropy in our garnet film is much weaker than the cubic one, the equilibrium magnetization directions are close to the diagonals of the cubic unit cell. We thus can assume $M_x \approx M_y$ so that the first term in the normal torque component dominates. As such, the in-plane symmetry of the excitation is given by the $E_x^2 - E_y^2$ term, reducing to $E^2 cos2\varphi$, where φ indicates the light polarization. Effectively, the in-plane symmetry of the photo-magnetic switching is lowered from four-fold to two-fold, which can be illustrated by rotating the polarization of the incident light from the [100] to the [010] direction. This leads to the reversal of the switching asymmetry: the normal component of the torque changes its sign, and thus the switching trajectories of the two considered initial magnetic states will be flipped. All these implications are in striking agreement with the experimental findings.

5.3 SIMULATION OF THE MAGNETIZATION TRAJECTORIES

We conducted simulations of multi-state magnetization switching in a real YIG:Co(001) thin film using an extended LLG model of photo-magnetic switching, developed in the reference [50]. In this model, laser pulses serve as a perturbation to the free energy density, allowing us to simulate trajectories for multi-state magnetization switching.

For our numerical simulations, we introduced a tetragonal distortion to the cubic magnetic symmetry. This distortion enabled us to perform simulations of magnetization trajectories during the photo-magnetic reversal in a YIG:Co film with $4mm$ point group symmetry (with or withiout muscut angle). We achieved this by numerically solving the LLG equation in spherical (θ,φ) coordinates, which can be expressed in the following form:

$$\begin{aligned} \dot{\theta} &= -\frac{\gamma}{M_s \sin\theta}\frac{\partial W_{tot}}{\partial \varphi} - \alpha \sin\theta \dot{\varphi} \\ \sin\theta\dot{\varphi} &= \frac{\gamma}{M_s}\frac{\partial W_{tot}}{\partial \theta} + \alpha\dot{\theta} \end{aligned} \tag{5.10}$$

Here, γ is a gyromagnetic ratio, α is a Gilbert damping parameter, M_s is a saturation magnetization. W_{tot} represents the total free energy, consisting of the cubic and effective (including demagnetization term) uniaxial anisotropy terms W_c and $W_{eff} = W_u - 2\pi M_s^2 \sin^2\theta$ respectively, and of the photoinduced magnetic anisotropy W_L [49] with the field H_L. The last term plays the role of the short laser-induced perturbation that exponentially decays with a timescale of about $\tau \approx 20$ ps. All these terms can be written, as follows:

$$W_{tot} = \frac{K_1}{4}\left[(\sin 2\theta)^2 + (\sin\theta)^4 (\sin 2\varphi)^2\right] + K_{eff}(\sin\theta)^2 + |E|^2 \beta_{ijkl} m_i m_j e_k e_l \tag{5.11}$$

In this equation we introduced the notations: $m_i = \frac{M_i}{|M_s|}$, $e_i = \frac{E_i}{|E|}$. Vector $\boldsymbol{E}$ represents the induced electric field due to photoinduced magnetic anisotropy and it has a decaying time dependence: $|E|^2(t) = |E_0|^2 e^{-t/\tau}$.

The cubic and uniaxial anisotropy constants were adjusted to match the material properties of the YIG:Co sample (as discussed in Chapter 2).

The introduced fourth-rank photo-magnetic tensor β_{ijkl}, in the case of the tetragonal $4mm$ point symmetry group, has seven independent components which can be expressed as: $\beta_{1111} = \beta_{2222} = \overline{11}$, $\beta_{3333} = \overline{33}$, $\beta_{1122} = \overline{12}$, $\beta_{1133} = \overline{13}$, $\beta_{3311} = \overline{31}$, $\beta_{1212} = \overline{44}$, $\beta_{2323} = \beta_{3131} = \overline{55}$.

Hence, the anisotropy term W_L can be represented as:

$$\begin{aligned}\frac{W_L}{|E|^2} &= \overline{11}(m_1^2e_1^2 + m_2^2e_2^2) + \overline{33}m_3^2e_3^2 + \overline{12}(m_1^2e_2^2 + m_2^2e_1^2) \\ &+ \overline{13}(m_1^2 + m_2^2)e_3^2 + \overline{31}m_3^2(e_1^2 + e_2^2) \\ &+ 4[\overline{44}m_1m_2e_1e_2 + \overline{55}m_2m_3e_2e_3 + \overline{55}m_1m_3e_1e_3]\end{aligned} \tag{5.12}$$

After simplifications and considering $|m|^2 = |e|^2 = 1$, equation can be simplified to:

$$\begin{aligned}\frac{W_L}{|E|^2} &= (\overline{11} - \overline{12})(m_1^2e_1^2 + m_2^2e_2^2) + (\overline{33} + \overline{12} - \overline{31} - \overline{13})m_3^2e_3^2 \\ &+ (\overline{31} - \overline{12})m_3^2 + (\overline{13} - \overline{12})e_3^2 \\ &+ 4[\overline{44}m_1m_2e_1e_2 + \overline{55}m_2m_3e_2e_3 + \overline{55}m_1m_3e_1e_3]\end{aligned} \tag{5.13}$$

Taking into account, that $e_3 = 0$ (electric field lies in the plane of the film, $\cos\theta_L = 0$), parametrizing $e_1 = \cos\varphi_L, e_2 = \sin\varphi_L$ and introducing the notations $B = \overline{11} - \overline{12}$, $A = B - 2(\overline{31} - \overline{12}) = \overline{12} + \overline{12} - 2\left(\overline{31}\right)$, $C = \overline{44}$, we will get:

$$\frac{W_L}{|E|^2} = (\sin\theta)^2 \left\{ B\left[(\cos\varphi)^2(\cos\varphi_E)^2 + (\sin\varphi)^2(\sin\varphi_L)^2\right] + \frac{A-B}{2} + C\sin 2\varphi\sin 2\varphi_L \right\} \tag{5.14}$$

For simplicity, we can normalize the induced electric field in the following way: $E' = E\sqrt{A}$. Thus, we can exclude parameter A from consideration and introduce new normalized parameters: $A \to a$, $B \to b = \frac{B}{A}$, $C \to c = \frac{C}{A}$. The Gilbert damping in simulation was set to α=0.2.

In the case of $E\|$[100] polarization (similar for sample no. 705), the expression takes the form:

$$W_L = \frac{1}{2}\left|E'\right|^2(\sin\theta)^2\left\{a + b\cos 2\varphi\right\}e^{-t/\tau} \tag{5.15}$$

Note, that a change of polarization $E\|$[100] to the orthogonal one $E\|$[010] can be effectively considered as a change of sign of coefficient b, while a change to "antiparallel" polarization $E\|$[-100] will not change anything.

Substituting the expressions for W_L, W_c, W_u in LLG equations, we will get equations describing dynamics in spherical (θ,φ) coordinates:

$$\begin{aligned}\dot{\theta} &= -\frac{\gamma K_1}{2M_s}(\sin\theta)^3\sin 4\varphi + bFe^{-t/\tau}\sin\theta\sin 2\varphi - \alpha\sin\theta\dot{\varphi}, \\ \sin\theta\dot{\varphi} &= \frac{\gamma K_1}{M_s}\sin 2\theta + \frac{\gamma K_1}{2M_s}\left[\sin 2\theta(\sin\theta)^2(\sin 2\varphi)^2 + \sin 4\theta\right] \\ &+ \frac{F}{2}e^{-t/\tau}(1 + b\cos 2\varphi)\sin 2\theta + \alpha\dot{\theta}\end{aligned} \tag{5.16}$$

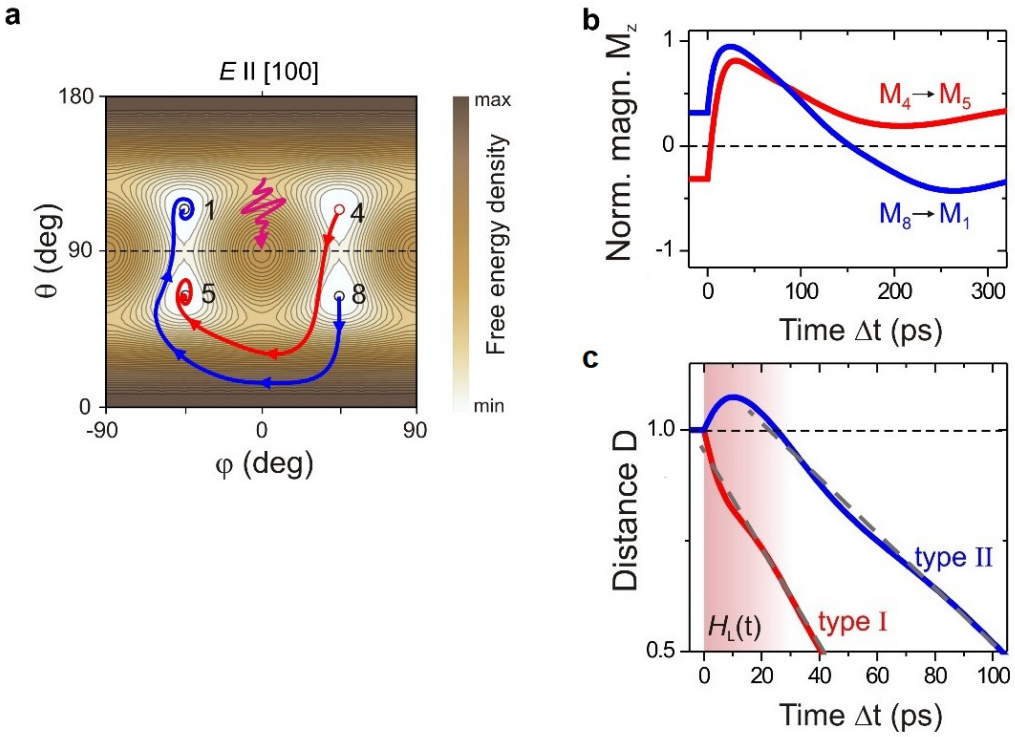

Figure 5.5: a) The simulated energy map with multi-states switching for different initial states b) The trajectories of a normalized out-of-plane component M_z c) The evolution of the distance to destination D highlighting type I and type II trajectories (dashed grey lines are the linear fitting). The red-shaded area shows the photo-induced anisotropy field $H_L(t)$ with a lifetime of about 20 ps

Here we introduced $F = \frac{\gamma A |E_0|^2}{M_s}$. It is responsible for the induced anisotropy, which mostly plays the role in timescales $t < \tau$. After that, the dynamics is almost "free" and is determined only by the properties of the system itself.

By fitting the model to the experimental data, we were able to extrapolate and obtain the complete trajectory, including all magnetization components (M_x, M_y, M_z). This allowed us to visualize the magnetization switching trajectories induced by a normally incident laser pulse with the electric field E, as depicted in Figure 5.5. This representation highlights the selectivity based on polarization.

The variations in M_z are summarized in Figure 5.5b. Notably, the difference in the rates of movement between the two simultaneously precessing magnetization vectors is a result of their lack of coupling. This is further verified through simulations, where the angle between these two magnetization vectors (bottom panel) displays significant fluctuations during the switching process. The weak magneto-dipole interaction between adjacent domains is negligible on the timescale of our observations, typically manifesting on the nanosecond timescale. Consequently, the two magnetization vectors move independently.

At low excitation levels (F=10, below the switching threshold), as shown in Figure 5.6c, the system's dynamics exhibit precession around its equilibrium point. This precession occurs after the system is perturbed from equilibrium and aligns well with the small-angle precession observed in the experimental results (Figure 5.1 and Figure 5.3d).

As the excitation level, F increases and surpasses the threshold value, the precessional dynamics transition into a switching behavior. This change occurs because the initial impact of the induced anisotropy becomes too significant, preventing the magnetization from remaining near its initial equilibrium point. This shift is illustrated in Figure 5.6c and b , showcasing multi-state magnetization switching at F = 60. These simulation results align closely with the experimental observations (see Figure 5.3b and c).

In the modeling, we adjusted the parameter b to obtain a better agreement with the experimental results of multi-state switching. We note that the tetragonal distortion of the cubic garnet lattice is characterized by $(b-1)$, and in a perfect cubic symmetry $b = 1$. Previously,[50] for the single-state switching we considered the parameter b in the range $0.3 < |b| < 0.5$. Here, we set $|b| = 1.6$ and obtained a good correspondence with the results of the multi-state experiment.

It is apparent that the model captures the pronounced asymmetry of the switching trajectories, thus paving the way for further analysis. In particular, we turn to the apparent dissimilarity of the characteristic timescales when the magnetization takes either one of the two available switching routes. To quantify this, we calculated the evolution of the normalized distance to the route destination as:

$$D = \sqrt{\sum_i \left(M_i(t) - M_i^f\right)^2} / D_0 \tag{5.17}$$

where M_i^f are the magnetization components of the final point on the trajectory and D_0 is the initial distance to the destination. A striking almost twofold difference in the movement rates along the two trajectories, shown in Figure 5.5c, corroborates their inequivalence and enables the qualitative distinction between the faster and slower (type I and type II as above) switching routes.

Lastly, the simulations reproduce the non-equivalence of the two types of trajectories in terms of transient variations of the normal magnetization component $\Delta M_z(\Delta t)$ (Figure 5.7b). Depending on the polarization (parallel to either [100] or [010]) of the optical

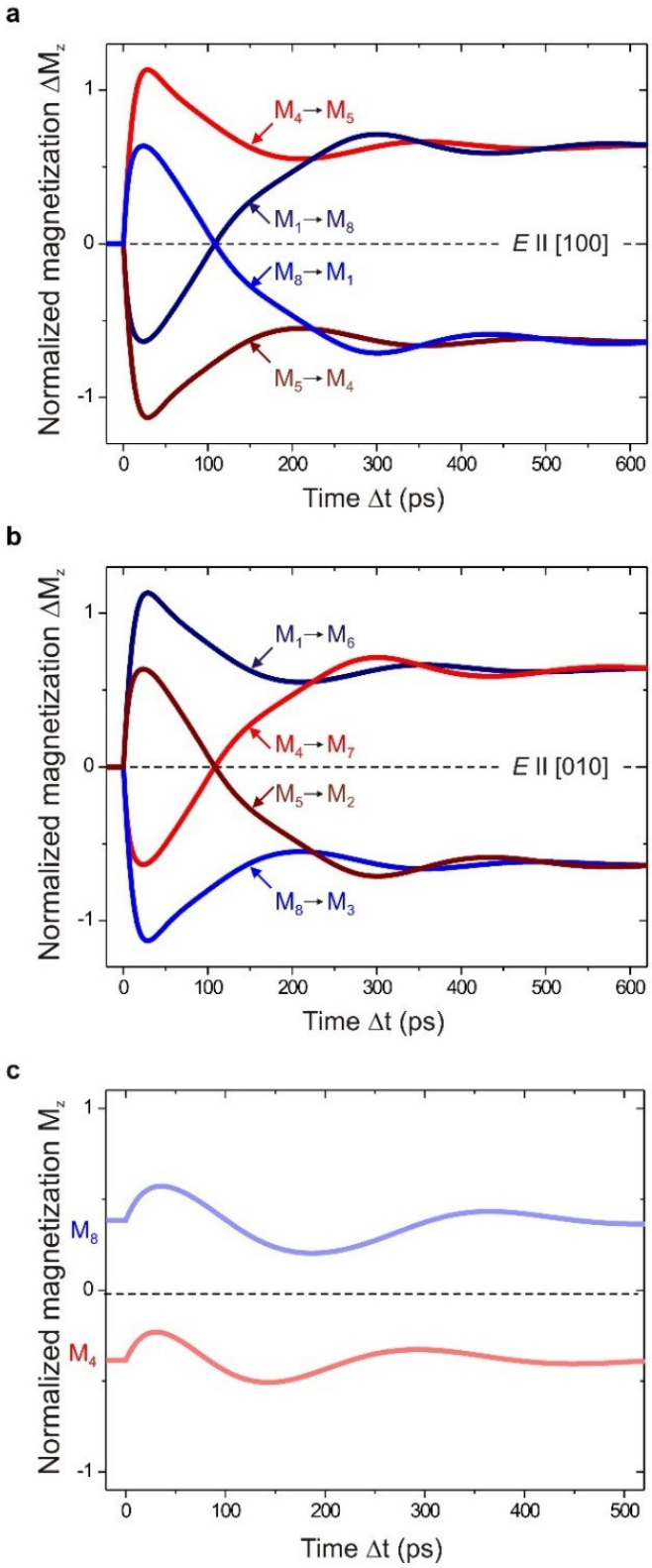

Figure 5.6: Simulation for all states (as in Figure 5.3) for a) $E\|[100]$ and b) $E\|[010]$ pump polarization with an intensity $F = 60$. c) The simulation of magnetization precession for an intensity $F = 10$.

pump pulse, magnetization selects the fast or slow trajectory towards its destination, in agreement with the experimentally found non-reciprocity (Figure 5.4a). Similarly, the simulated odd component in Figure 5.7c exhibits an oscillating character, again correlating well with the experimental observations and reinforcing our understanding of its origin in the sign of the initially produced photo-magnetic torque.

The apparent non-reciprocity of the photo-magnetic switching routes is enabled by two main factors. Firstly, it is only possible when the switching is precessional in nature, as opposed to the thermal mechanisms accompanied by the magnetization quenching. Secondly, it requires an intricate interplay of the excitation tensor symmetry and magnetic energy landscape. In particular, in a uniaxial magnetic system, the observed asymmetry is impossible, which makes it difficult to imagine the discussed non-reciprocity in amorphous alloys where the dominant uniaxial contribution of magnetic anisotropy is often governed by the growth direction. Cubic magnetic crystals thus represent an attractive class of materials for exploring the richness of the nonthermal excitation of non-reciprocal magnetization dynamics. They constitute a promising playground for engineering magnetic energy landscapes in order to achieve faster and more efficient unidirectional switching. In particular, the change in cubic and uniaxial growth-induced anisotropy enables encoding materials with a spatial distribution of states with different energy thresholds, which can dramatically reduce the switching energy.

The approach developed in our work can be extended towards more sophisticated systems featuring additional external stimuli and physically rich interaction mechanisms. In particular, thermal demagnetization can be accounted for on equal footing by introducing Landau-Lifshitz-Bloch formalism. Moreover, there is tremendous potential in utilizing strain (either dc or phonon-induced) or auxiliary magnetic and electric fields to control the effective field of the anisotropy. Taking advantage of the extremely large phase space with these fields as control parameters, the switching between multiple domain states holds promise for the advancement of multi-level magnetic memories. In particular, the inequality of the switching trajectories indicates the possibility of simultaneously steering a set of magnetizations from one combination of states to another with a single stimulus, realizing a multi-dimensional magnetization switching. By encoding information not only in binary but in a set of magnetization states (e.g. logical combinations of 00, 01, 10, 11, etc.), a greater number of distinct levels can be achieved, allowing for higher data storage density.

The presented results significantly expand modern understanding of the coherent, nonthermal magnetization switching and open a plethora of possibilities for designing energy-efficient switching routes at arbitrary energy landscapes.

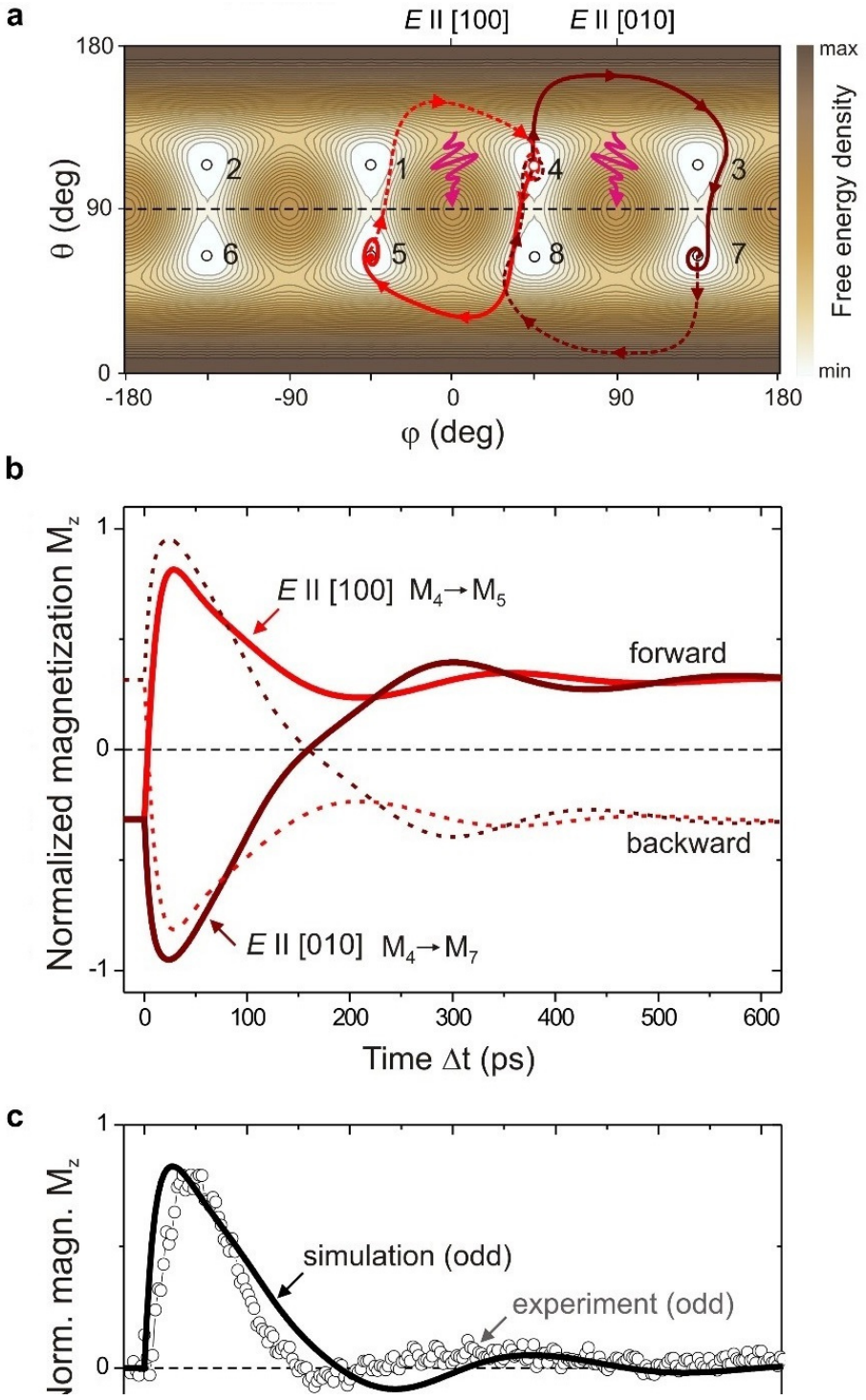

Figure 5.7: a) The full simulated energy map showing different magnetization trajectories induced by the $E\|[100]$ or $E\|[010]$ light pulses. b) Non-reciprocity of the all-optical switching caused by the change in the light pulse polarization plane (forward and backward switching). c) Differential (odd) contribution to $E\|[100]$ and $E\|[010]$ trajectories responsible for the no-reciprocity compared with the experimental data.

6

NONTHERMAL ULTRAFAST ALL-OPTICAL TOGGLE SWITCHING OF MAGNETIZATION

In accordance with Curie's principle, it is intuitive to expect that the symmetry of the cause should be reflected in the symmetry of the effect [148]. However, femtosecond laser excitation has the potential to violate this principle. Traditionally, it was believed that heating alone, lacking the symmetry of a magnetic field, could not result in a deterministic reversal of magnetization. However, it was demonstrated that ultrafast heating induced by a femtosecond laser pulse could toggle the magnetization between stable bit states without any external magnetic field [7, 27, 29]. Given this, it raises the question of whether a toggle regime can be achieved through photo-magnetic switching without involving heating.

To explore this idea, we investigated YIG:Co samples without a miscut angle, which possess pure cubic symmetry, making all magnetization states equivalent. In this desired scenario, a single pulse of ultrafast laser excitation with linearly polarized light alters the magnetic anisotropy, causing the switching, and another pulse switches the magnetization back to the initial state, toggling the magnetization between two stable bit states.

In this Chapter, we will present and discuss a new toggle regime of cold photo-magnetic switching. Using YIG:Co samples without the miscut and with pure symmetry, we examine the precession dynamics and switching possibilities. We then investigate the toggle switching regime in a double-pump experiment, defining the possible coherent magnetization reversal based on pump pulse polarization control. Subsequently, we study the impact of the effective anisotropy field on the switching properties, determining its dynamics. By modifying the magnetocrystalline component of the effective field of anisotropy through temperature changes, we investigate its impact on the efficiency of photo-magnetic switching within the temperature range from 200 K to 450 K. Using the theoretical model which was described in Chapter 5, we compare our findings with simulation results. Finally, we will present a balance between the speed and the energy threshold of toggle photo-magnetic switching.

The results discussed in this chapter have been submitted as preprints:

T. Zalewski, A. Maziewski, A.V. Kimel, A. Stupakiewicz, "Ultrafast all-optical toggle writing of magnetic bits without relying on heat", *arXiv:*2311.10173 (2023).

T. Zalewski, L. Nowak, A. Stupakiewicz, "Coherent control of nonthermal backswitching of magnetization in garnets", *arXiv:2311* (2023).

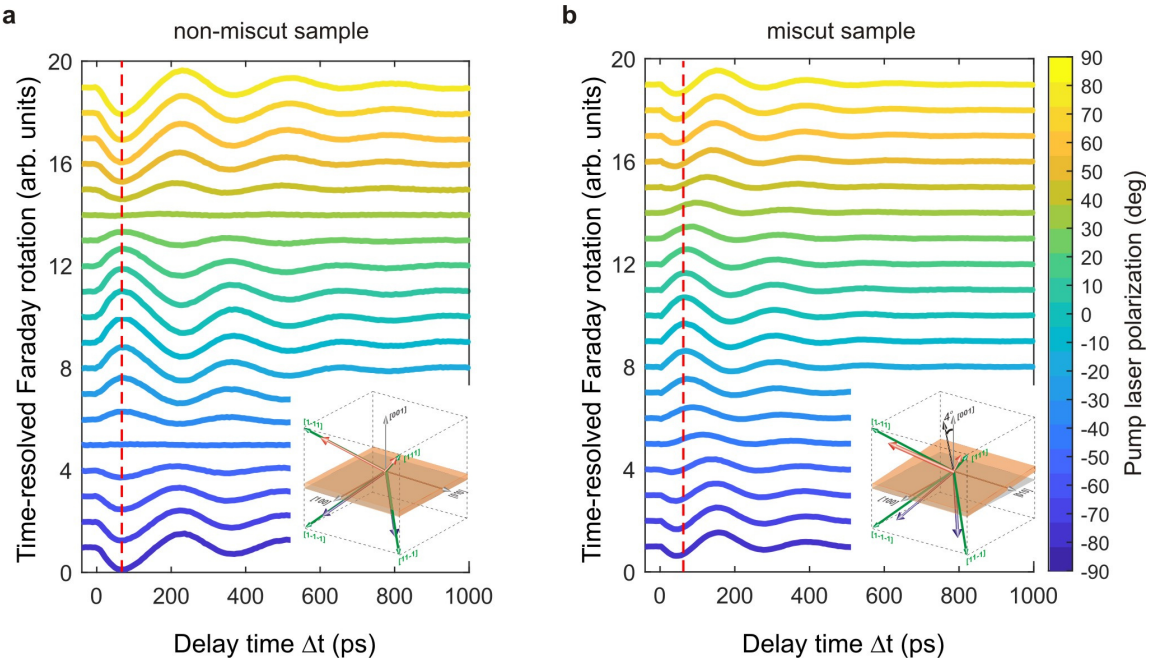

Figure 6.1: The pump polarization dependence of the magnetization precession for non-miscut a) and miscut samples b) respectively. Angle of pump polarization 0 deg denominates alignment with [100] crystallographic axis in YIG:Co films.

6.1 PHOTO-MAGNETIC TOGGLE SWITCHING IN GARNET WITHOUT MISCUT

The discovery of ultrafast all-optical toggle switching of magnetization in the metallic ferrimagnetic alloy GdFeCo [7] is probably one of the most significant breakthroughs in the field. It inspired the investigation of current-induced toggle switching in GdFeCo [149] and led to studies of the switching mechanisms in other classes of metallic ferrimagnets [27, 29]. In all of these cases, one key requirement for achieving this mechanism was ultrafast heating of the ferrimagnetic material on a timescale much faster than the characteristic timescale of interaction between the spins of the two magnetic sublattices [17, 19, 26, 150, 151]. Ultrafast heating was shown to drive the ferrimagnets into a highly non-equilibrium state, making it favorable for subsequent relaxation to involve magnetization reversal. The toggle switching without relying on heat would significantly reduce energy dissipation during the writing of magnetic bits, but such a mechanism has not been demonstrated until now.

In our pursuit to find a medium for cold toggle switching, it is worth noting that this kind of switching, in principle, goes against thermodynamic Curie's principle [148], which states that the symmetry of the cause should be reflected in the symmetry of the effect [152]. Essentially, since each excitation event is identical and the symmetry of the cause does not change, toggling implies that the symmetry of the effect alters from pulse to pulse. This kind of toggle switching becomes possible, for example, in the case of ultrafast precessional switching, where a pulse of a magnetic field is applied perpendicular to the magnetization precisely during half of the precession period. In this scenario, thermodynamic Curie's principle is violated because the field is applied on a timescale much shorter than the time required for the magnetization to reach thermodynamic equilibrium, meaning to align parallel with the applied magnetic field. Therefore, to demonstrate cold all-optical toggle switching, we need to figure out a way

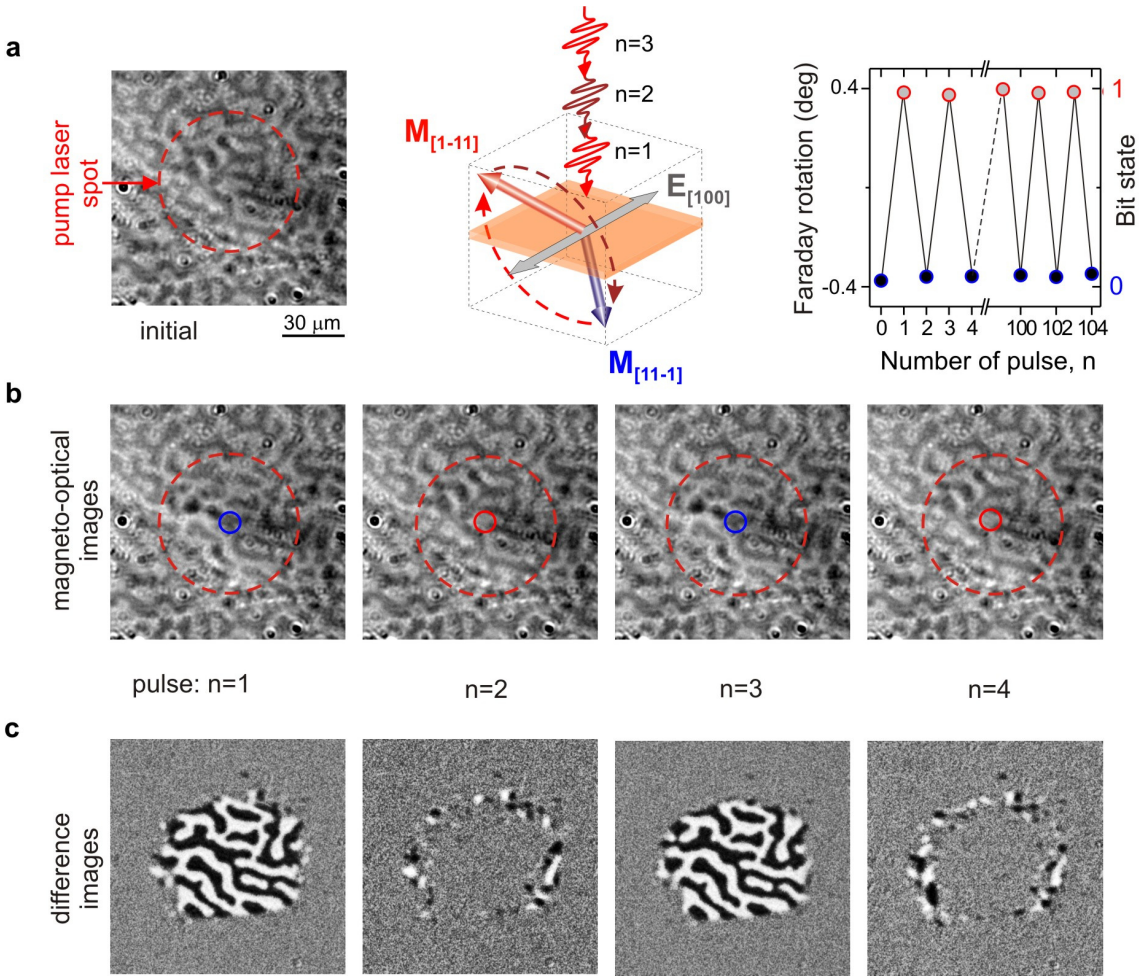

Figure 6.2: a) Image of magnetic domains with initial magnetization states [11-1] (indicated by black domain) and [1-11] (indicated by white domain). The observed switching corresponds to transitions from [11-1] to [1-11] states. Every other pulse does not alter the domain shape, resulting in non-deterministic switching of magnetization in domains without an external magnetic field. b) Magneto-optical images of the YIG:Co structure after the illumination of a series of single 50 fs pump pulses at a wavelength of 1300 nm using polarized light along the [100] crystallographic axis in garnet films. Dashed circles indicate the area exposed to the laser excitation. Small solid circles indicate the region, where the measurements of the magneto-optical Faraday effect shown in panel (a) were done. c) Differential images revealing the toggle character of switching. d) Changes of the Faraday rotation in the black domain upon excitation by a sequence of laser pulses. Every single pulse changes the magneto-optical effect suggesting that the magnetization is toggled between two stable bit-states.

to generate an effective magnetic field acting on the magnetization within half of the magnetization precession period.

To generate such effective fields and demonstrate 'cold' all-optical toggle switching, we utilize photo-induced magnetic anisotropy in YIG:Co with pure cubic symmetry. Previous studies had suggested that the observed polarization-dependent switching in iron garnets could only be explained if the point group of the iron garnet films had relatively low symmetry 4 [152]. However, to facilitate toggle switching, a substrate without miscut was utilized, increasing the point group symmetry to $4mm$. To test this hypothesis, we used sample YIG:Co no. 10, which had no miscut with a precision of 0.1°.

To confirm the presence of pure cubic symmetry and to compare the magnetization dynamics properties with samples having a miscut, we conducted time-resolved precession measurements using the setup described in Chapter 3.4.4 with the pump polarization plane dependence, as depicted in Figure 6.1. A notable distinction between both samples is the absence of a miscut, which, in contrast to the miscut sample, results in the complete suppression of the precession signal for an orthogonal arrangement of a linearly polarized pulse ($E\|$[110] / [1-10]). In this case, the orientation of the pump polarization state is set at ϕ = 45° / -45° relative to the crystallographic axis. This observation serves as a confirmation of the pure cubic symmetry in the non-miscut sample.

Next, we attempted to achieve magnetization switching using single femtosecond laser pulses by adjusting the polarization plane to maximize precession amplitude (<100>-type direction) and increasing the laser fluence from 10 mJ/cm² to 50 mJ/cm². The results are presented in Figure 6.2 as a series of consecutive magneto-optical images of the YIG:Co taken before and after illumination with the pulses. In these images is possible to see that each pulse reverses the out-of-plane component of the magnetization M_z while maintaining the positions of the domain walls. The observed magnetization switching is an coherent reversal process based on the precessional movement of magnetization. However, due to the labyrinth-like domain structure of the garnet, the changes are not clearly visible. Therefore, we use differential images (Figure 6.2c) relative to the initial state before laser pump excitation to demonstrate the switching.

These differential images reveal that, in contrast to earlier studies on garnets with miscuts [9], each pulse effectively toggles the magnetization state. Consequently, magnetic domains are written and erased with the same pump polarization. The final state of magnetization is determined by its initial state and the number of pulses applied. An odd number of pulses induces switching, while an even number of pulses effectively does not alter the magnetization. Furthermore, changing the light polarization plane to an orthogonal direction, using pulse polarization either in the [100] or [010] direction, results in effectively in qualitatively same magnetization switching. To the best of our knowledge, this is the first demonstration of all-optical toggle switching through a mechanism that does not rely on heat.

6.2 COHERENT CONTROL OF TOGGLE SWITCHING USING DOUBLE-PUMP EXCITATION

Observing the toggle-switching regime naturally raises several new questions. Firstly, if one pulse can switch magnetization and a subsequent pulse can reverse it, what will happen if both of these pulses appear together? Will the magnetization motion be frozen, or enhanced, and how can it be controlled via polarization? Since the switching can be observed in the statics regime, in which the exposure time enabling obtaining MO

images can be arbitrarily long and last several hundred milliseconds, in a relatively simple experiment using double pump excitation, we can try to answer the questions asked.

On the other hand, from an application perspective, the lack of a necessity to control the light polarization state for writing and erasing magnetic 'bits' can significantly simplify the setup, eliminating the need for changing the pulse polarization at high frequencies to match the recording speed. Previously, with a 60 ps minimum separation time between erasing and writing pulses with orthogonal polarization to each other in garnet with miscut angle, it was demonstrated that photo-magnetic switching can operate at frequencies up to 20 GHz [53]. In the case where pulses with the same polarization can be utilized, the question arises: what will be the time of erasing and writing of domains in toggle regime?

To analyze this kind of pump pulse pair interference, we utilized the double pump scheme discussed in Chapter 3.4.6. In this case, by providing an additional pump beam and adjusting the mutual delay between the first pump A and the second pump B set as Δt_{AB} time, one can precisely investigate their mutual impact.

First, we precisely adjusted the optical parameters of pump A and B to match each other. The pump fluence (50 mJ/cm²), polarization plane (along to [100]), and the localization on the sample were unified to provide the exact switching area using either A or B a single laser pulse, whose size is marked in the first image in Figure 6.3a. Next, the sample was excited by both pulses A and B being in spatio-temporal overlap. By delaying the pulse B and increasing Δt_{AB}, a full set of double pump images was captured. Here, after a pump excitation, only the final static domain structure was observed using MO microscopy in a static regime.

To quantitatively analyze the impact of the second pump pulse on switching, we expressed the efficiency of switching as a normalized switching area. Because determining the normalized switching area in the case of a labyrinth-like structure may not be obvious, we used the same repeatable procedure for every analyzed image. Firstly, the analyzed image was prepared in differential form. Next, to remove any remaining background non-uniformities, the image was once again differentiated with a copy blurred in a Gaussian filter and subjected to bandpass filtration. Such an image was separated into two parts with a low threshold and a high threshold, selecting a particular part (with white or black contrast) of the domain structure. Next, the images were added together once again and binarized. Finally, after a set of binary operations, including filling holes and closing the structure, the switching size was determined and could also be translated into switching efficiency. The whole procedure was exemplarily presented in Figure 6.3b.

During the double-pump excitation, the magnetization switching occurs up to Δt_{AB} = 320 ps, after which the toggle regime works comprehensively, efficiently switching and then back-switching the magnetization. For smaller Δt_{AB} times, the dependence of the switching area is depicted in Figure 6.3c. The area was normalized to the area switched by a single pump, signifying a value of one. The obtained time-dependent profile is characterized by two characteristic steps. To understand this shape, additional analysis involving double-pump time-resolved measurements is required.

In order to conduct this analysis, we used a double pump and probe setup capable of time-resolved tracking of magnetization dynamics using pump fluence 10 mJ/cm² (below the switching threshold), as described in Chapter 3.4.6. In this case, for every particular delay between pulses A and B Δt_{AB}, the probe beam was swept with the Δt delay, revealing both pump beam's impact on magnetization precession. Both pulses were once again equalized and matched to individually induce exactly the same precession

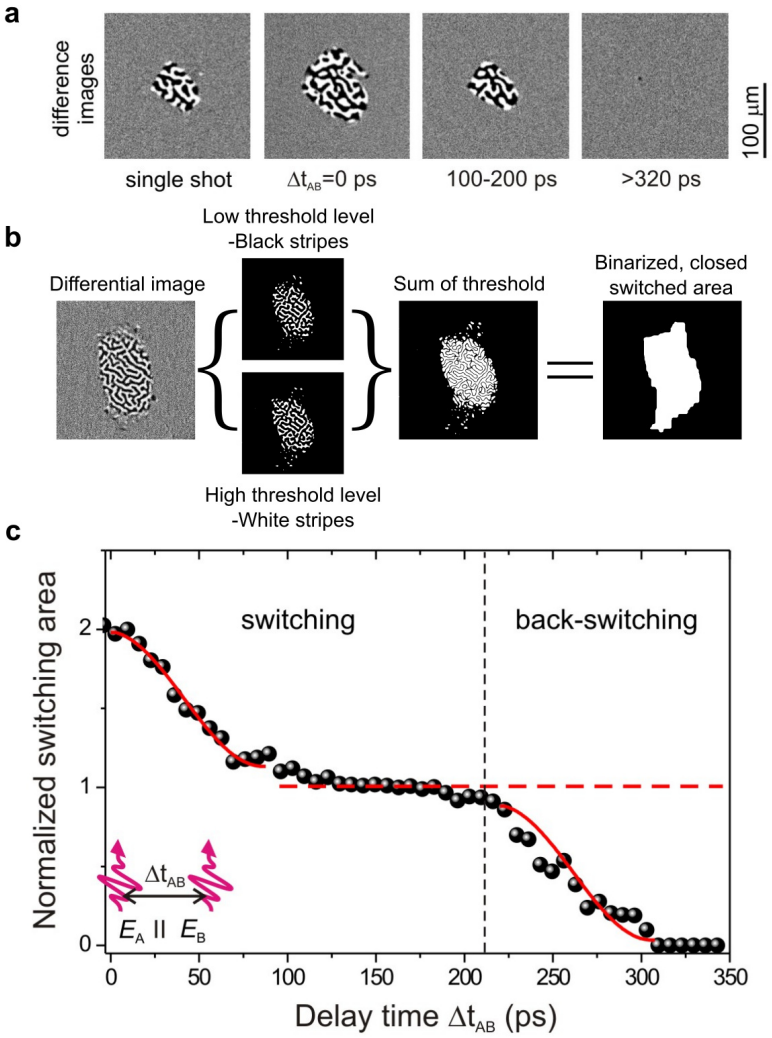

Figure 6.3: a) MO difference images presenting a double pulse writing sequence with two identical 50 fs pump pulses A and B delayed by $\Delta t_{AB}$with wavelength 1300 nm, polarized along the [100] axes ($\varphi_A = \varphi_B = 0°$). The first image shows the switching after excitation with either single A or B pulse. Subsequent images present the obtained switching pattern during double pump pulse excitation with the marked delay Δt_{AB}. b) The procedure of thresholding and binarization to determine the normalized switched area in the case of the labyrinth-like domain structure. c) The normalized switched area as a function of delay timeΔt_{AB}. The solid red line directing to the saturation regions was fitted using $\cos(2\pi\Delta t_{AB}/T)$within $T/4$ delay time, where T is the period of magnetization precession [53].

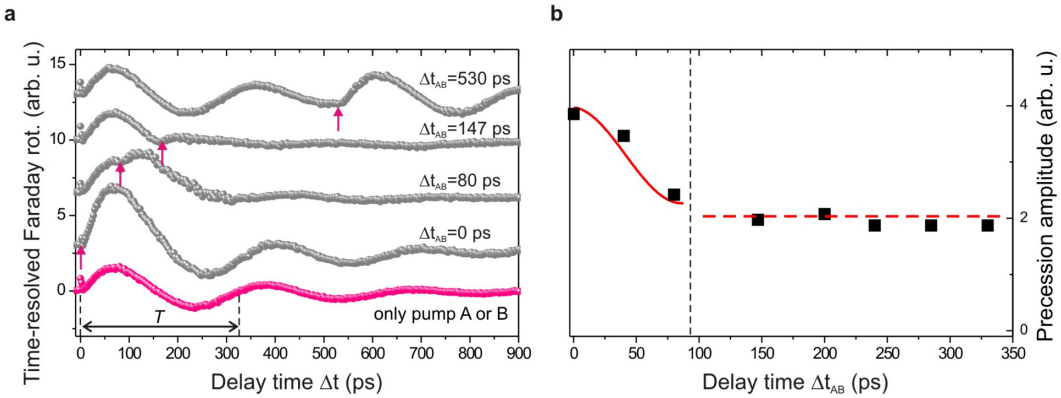

Figure 6.4: a) The time-resolved Faraday rotation signal from the double pump and probe setup. Both pump pulses were polarized along the same polarization plane along [100] direction in YIG:Co. The arrows mark the temporal position of pump pulse B, which is delayed by Δt_{AB}. b) The effective precession amplitude of both pump pulses determined as amplitude of magnetization precession.

signal. The obtained time-resolved double pump traces are presented in Figure 6.4a, with arrows marking the position of pump pulse B.

Notably, for Δt_{AB} = 0 ps, the mutual overlapping of the pulses causes constructive interference, enhancing the effective amplitude. Therefore, the overlapping of two identical pulses increased the switching area by a factor of two. Increasing Δt_{AB} affects the magnetization precession, effectively decreasing its amplitude, as expressed in Figure 6.4b. The precession amplitude was determined using Equation 3.21. The superposition of the pulses effectively increases the amplitude up to about 80 ps, which correlates with the region of increased switching efficiency. Further, the two precession signals start interfering with each other in counter-phases, resulting in the freezing of the oscillation after half the period, marked for Δt_{AB} = 147 ps. In this range, the effective amplitude is defined solely by pulse A, and the switching efficiency does not change up to about Δt_{AB} = 210 ps. Finally, for Δt_{AB} > 210 ps, the pulses are separated far enough not to be able to constructively interfere with subsequent sine-like oscillations sufficiently to overcome the switching threshold, as a single effective pulse. Therefore, while the first pulse provides switching, the second, starting from a position with already almost stopped magnetization motion, provides a separate stimulus resulting in back-switching. The complete back-switching occurs at about Δt_{AB} = 320 ps, which can be correlated with the oscillation period of frequency f.

It is worth noting that pulse fluence has a significant impact on both the switching efficiency and the dynamical measurements. For instance, for pump fluences below the switching threshold, as shown in [53], the mutual interference of pulses can provide switching in the first region with increased effective amplitude (up to 80 ps). Moreover, very high fluences could potentially allow for interference between further oscillation maxima, resulting in more "steps" in the switching area dependence in Figure 6.3c.

Equally interesting is the case with two pump pulses polarized orthogonally to each other. Using the same approach and settings, we performed analogous measurements, only changing the polarization plane of the pump pulse B. The obtained measurements are provided in the same manner, with the normalized switching area dependence utilizing double pump excitation presented in Figure 6.5 and double pump and probe time-resolved dynamics in Figure 6.6.

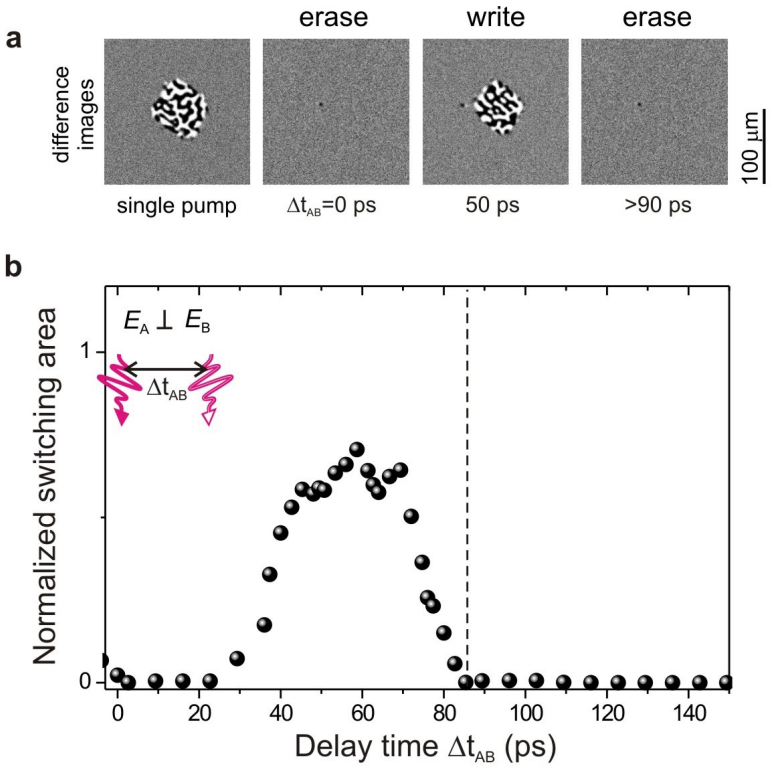

Figure 6.5: a) MO difference images presenting a double pulse writing sequence with two pulses A polarized along [100] axis ($\varphi_A = 0°$) and B polarized along [010] axis ($\varphi_B = 90°$). As previously, the first image shows the switching after excitation with either a single A or B pulse with the size used for normalization. The subsequent image represents the obtained switched pattern depending on the Δt_{AB}. b) The normalized switched area as a function of delay time Δt_{AB}.

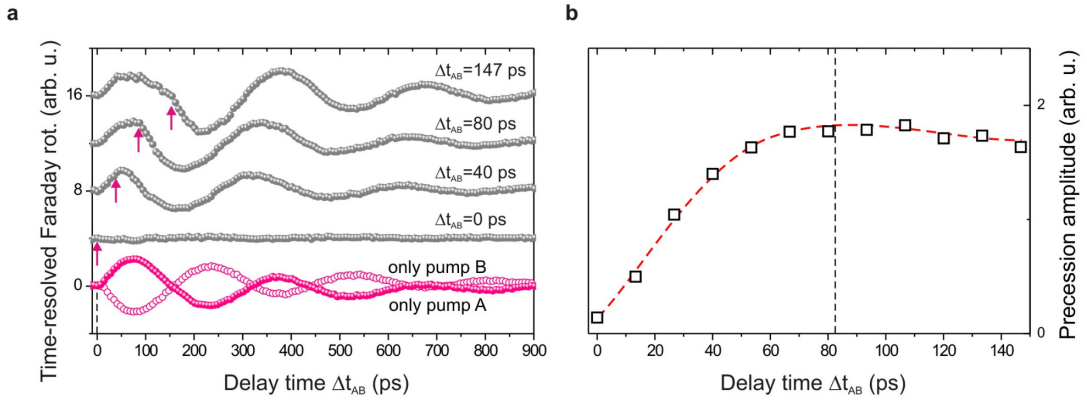

Figure 6.6: a) The time-resolved Faraday rotation signal from the double pump and probe setup with pump A polarized along [100] and pump B along [010] planes. Notably, the two pump signals, being in counter-phase, interfere completely destructively $\Delta t_{AB} = 0$ ps. for b) The effective precession amplitude of both pump pulses.

With pump A polarized along the [100] axis and pump B polarized along the [010] axis, the generated torque has opposite signs (see Chapter 5). Therefore, for Δt_{AB} = 0 ps, precessional signals being in counter phases interfere destructively, resulting in no oscillations and therefore do not provide any switching. However, by increasing Δt_{AB}, a characteristic region between Δt_{AB} = 35 - 80 ps in which switching is obtainable occurs. Once again, to understand this behavior, insight into dynamics is required. As it may be noticed, when precession traces are delayed, the interference changes its character and starts to provide precession similar to the one obtained by a single pump. Further increase of Δt_{AB} indeed increases the amplitude of precession to the saturated level, however, after about a quarter of the oscillation period $T/4$, the second pump pulse B is able to overcome switching. It results once again in switching with pulse A and magnetization reversal with pulse B.

Both of these results underline that the polarization control is not necessary to write and erase magnetic bits via cold photo-magnetic switching. Switching can be toggled for pulses with the same polarization, achieving repetition rates of 3 GHz for the Δt_{AB} = 320 ps. On the other hand, using pulses with orthogonal polarization can also provide switching however, it requires precise control of pump delays.

Both of these results underline that changing polarization is not necessary to write and erase magnetic bits via cold photo-magnetic switching. Switching can be toggled for pulses with control of the delay time between pulses, achieving a switching frequency of up to 50 GHz.

6.3 DYNAMICS OF MAGNETIZATION SWITCHING AT DIFFERENT TEMPERATURES

The double-pump experiment provides essential information about the possible writing and erasing scenarios, but it does not answer the question about switching dynamics achieved with a single pulse. To address this, we conducted time-resolved single-shot experiments using the experimental setup described in Chapter 3.4.5. In this setup, we employed a single pump pulse with sufficient fluence for inducing switching and a single defocused probe pulse to illuminate the large sample. We then captured a series of time-resolved images. An example of a captured stack of MO time-resolved images is presented in Figure 6.7a. It is apparent that the contrast observed in the final image develops within 10-60 ps, confirming the ultrafast switching character as seen in the previous non-miscut case [9]. We designate the characteristic time τ of the magneto-optical contrast (intensity at magnetic domain) development as the switching time, which is determined by fitting the data with a simple exponential decay model in the form of $1 - exp(-\Delta t/\tau)$.

In the following section, the sample was placed in a liquid-nitrogen-cooled cryostat to enable measurements across a wide temperature range. These measurements not only helped determine the temperature switching range in YIG:Co but also shed light on the potential for manipulating the effective anisotropy field H_A(dominated by field of the cubic anisotropy) through temperature changes.

Initially, we observed magnetization switching over a remarkably broad temperature range, spanning from 200 K to 450 K. Furthermore, we determined the switching time for each temperature. For an in-depth understanding of magnetization dynamics, we conducted temperature-dependent pump-probe measurements of magneto-optical Faraday rotation at lower pump fluences (<10 mJ/cm^2) to determine the nature of magnetization

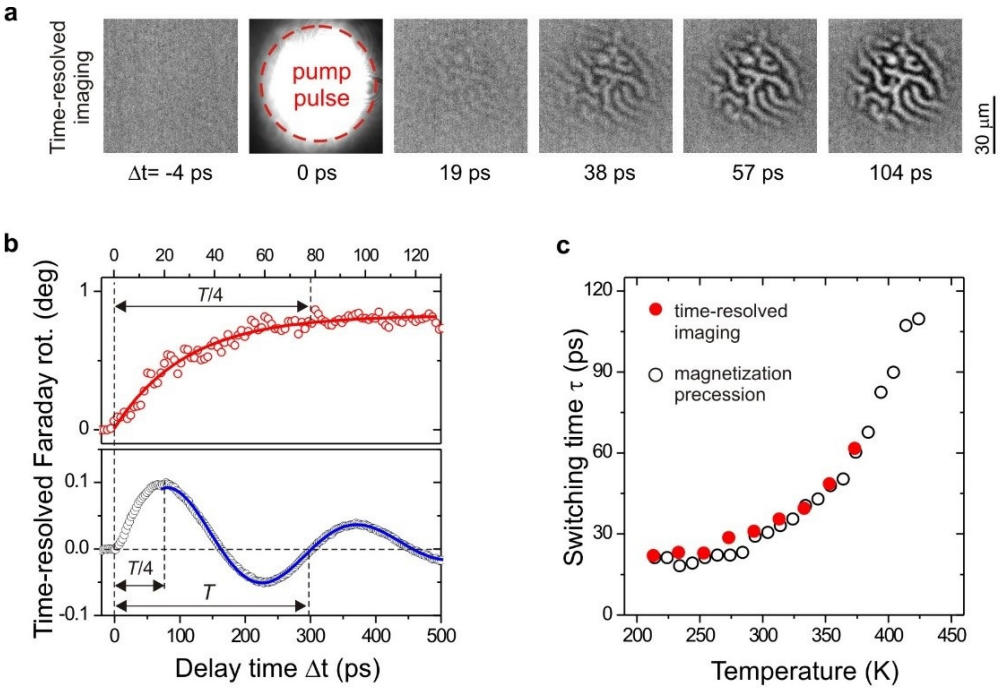

Figure 6.7: a) A stack of time-resolved differential images showing photo-magnetic switching in YIG:Co at room temperature. The sample was illuminated by the pump pulse polarized along [100] with a fluence of approximately 50 mJ/cm². b) (upper panel), Temporal evolution of the magnetic contrast in time-resolved imaging, and determination of the characteristic switching time τ by fitting using exponencial function (red solid line) to the data. (lower panel), Time-resolved Faraday effect resulting from low amplitude precession, which allows for the determination of the precession period and the frequency by fitting a damped sin function (blue solid line) to the data. c) The switching time for different temperatures which was measured with two methods.

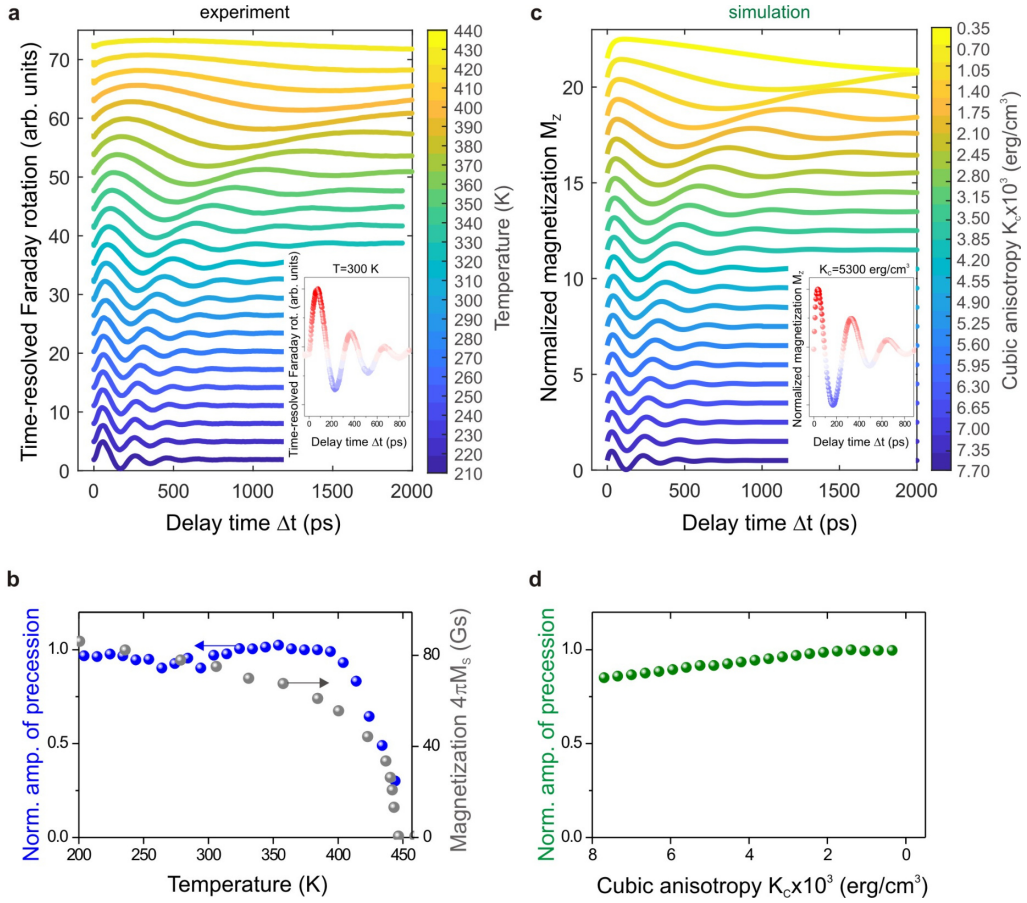

Figure 6.8: a) The experimental time-resolved magnetization precession dependence on temperature. The magnetization movement was stimulated by pulses with a fluence of 10 mJ/cm² polarized along the [100] direction. The color code for the map in Figure 6.9 is denoted in the insets. b) The temperature dependence of the normalized amplitude of the photoinduced magnetization precession, corresponding to the magnetization saturation in the non-miscut YIG:Co sample. c) Simulation of the photo-magnetic precession for different cubic anisotropy constants to match the experimental data. d) The dependence of the normalized precession amplitude obtained in simulations.

precession. At fluences above the switching threshold, we used the single-shot method to determine the spatio-temporal switching properties.

The dynamics of magnetization precession at different temperatures are depicted in Figure 6.8a, represented as a waterfall plot. These traces were normalized to match the color code in Figure 6.9, as explained in the insets. The measurements were fitted with a damped sine function, with frequencies determined according to equation 3.21. The relationship between precession amplitude and temperature is illustrated in Figure 6.8b, showing a correlation with the magnetization saturation M_s in the sample. As temperature rises, M_s decreases, especially up to the Curie temperature near 455 K. Over a broader range from 200 K to 400 K, M_s remains relatively similar.

To further refine our understanding, we used a simulation framework based on the Landau-Lifshitz Gilbert formalism, as detailed in Chapter 5. The model included the total energy of the system (equation 5.11) and short-lived, photo-induced anisotropy W_L (equation 5.15), which exponentially vanishes about 30 ps. In our modeling to align with the experimental data, we set the photo-magnetic tensor coefficients as $a = 1$ and

b = -1.2. The cubic anisotropy, initially measured at room temperature as K_c = 5.5 × 10^3 erg/cm², was adjusted in accordance with changes in the sample's temperature. A small uniaxial contribution was incorporated as the dependent parameter K_u = 0.1 K_c. At room temperature the magnetization saturation was kept constant at $4\pi M_s$ = 75 G, and the Gilbert damping was set to α = 0.19. Both damping and magnetization saturation change with temperature, especially in the range of approximately the Curie temperature. However, in the temperature range of 200-400 K in YIG:Co, the changes in these parameters can be neglected in terms of their impact on the anisotropy value.

The results of the magnetization precession are visualized in Figure 6.9a (from the experiment) and Figure 6.9b (from simulations), represented as color maps showing normalized Faraday rotation or the out-of-plane magnetization component M_z. In these maps, red color corresponds to positive signal of Faraday rotation, blue color indicates negative signal of Faraday rotation, and white represents signal close to zero. These maps demonstrate the temperature-induced alterations in magnetocrystalline anisotropy, which influence magnetization precession and lead to a more than five-fold change in frequency of magnetization precession.

Further investigation involved dynamic measurements with an applied magnetic field H. The magnetic field was applied in the in-plane direction of the sample, with its orientation following the [100] crystallographic direction. The obtained field-dependent precession traces are presented in Figure 6.10 and were fitted using equation 3.21 to determine the precession frequency f.

As the applied magnetic field increases to around H = 0.4 kOe, the domain structure is maintained. This process eventually leads to the formation of a single domain in a non-collinear state. With further increases in the field strength, the magnetization gradually rotates toward the direction of the applied field, ultimately reaching a collinear state with an in-plane magnetization orientation at approximately 2 kOe. The nonlinear dynamics in the sub-switching regime of magnetization were discussed in [49].

It is known that the precession frequency is determined by the strength of the applied magnetic field and the effective field of magnetic anisotropy [153]. For high magnetic fields >3kOe, the precession frequency, depending linearly on the field, can be understood using the classical formula $\omega = 2\pi f = \gamma \left| H_{eff} \right|$ [89]. Here, γ represents an effective gyromagnetic ratio, similar to classical FMR experiments [76] which provides information about the anisotropy in the YIG:Co films.

Using fits with a damped sine function we deduced the frequency of the ferromagnetic resonance mode from the measurements in the range from 200 K to 450 K and plotted the frequency f as a function of temperature in Figure 6.9c. It is seen that both the switching time and the frequency scale similarly with a temperature. Since the external field in measurements for toggle switching is zero and the magnetization precession in domains is coherent, the temperature dependence of the frequency must originate from the temperature dependence of the effective field of magnetic anisotropy. Using Kittel's formula for the frequency of ferromagnetic resonance mode in garnet:

$$f = \frac{\gamma}{2\pi M_s \sin\theta} \sqrt{\frac{\delta^2 W}{\delta\theta^2}\frac{\delta^2 W}{\delta\varphi^2} - \left(\frac{\delta^2 W}{\delta\theta\delta\varphi}\right)^2} \tag{6.1}$$

where θ and φ are the polar and azimuthal angles, respectively. We estimated the effective field of magnetic anisotropy for the frequency of precession Figure 6.9c. According to

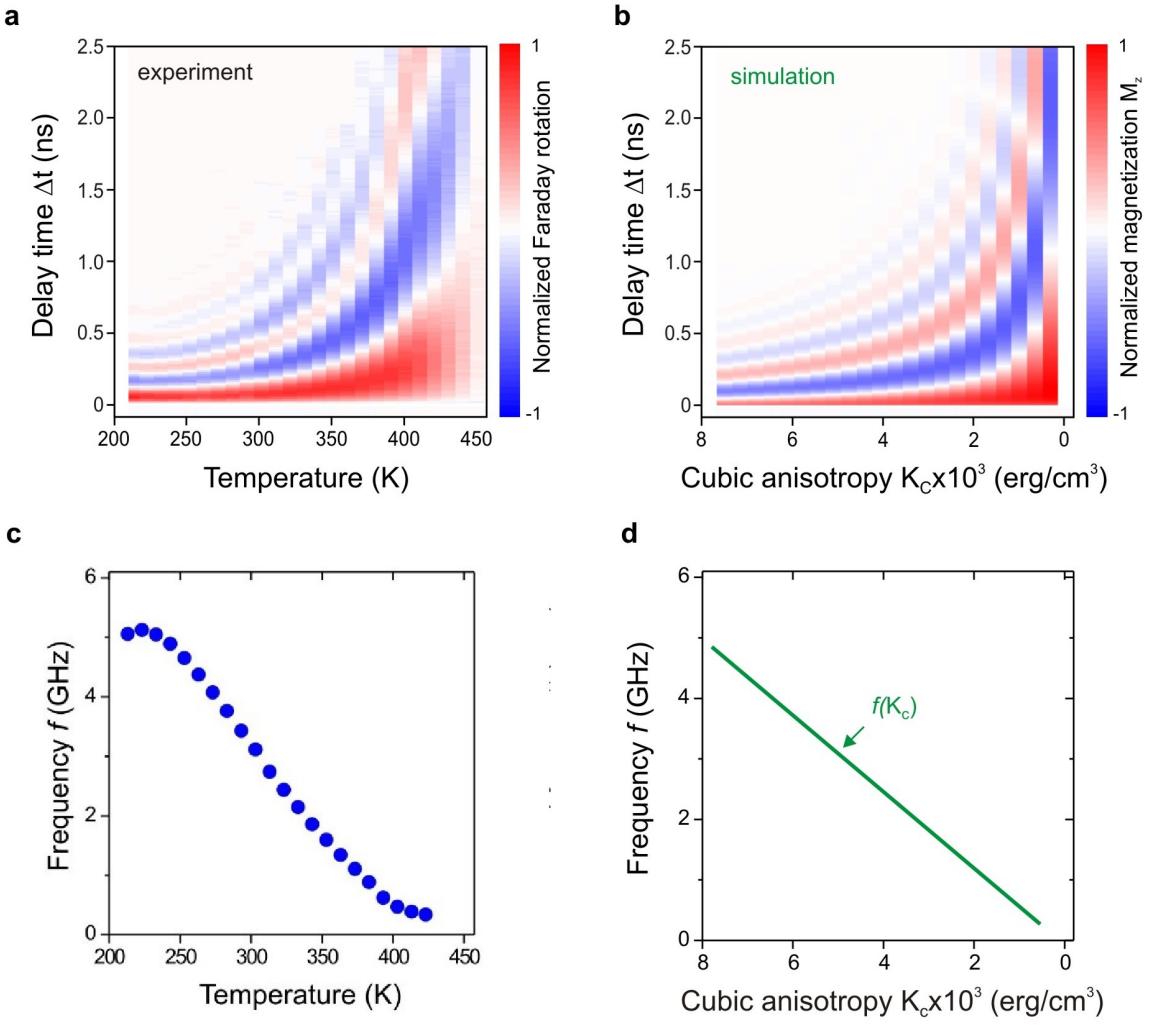

Figure 6.9: Time-resolved toggle switching at different temperatures. a) The color map illustrating the photo-induced magnetization precession dependence on temperature based on the data in Figure 6.8a, and b) a simulated dependence on changes in cubic anisotropy constant K_c according to Figure 6.8c) The precession frequency's dependence on temperature,rysunek c podmienic z publikacji and d) simulation results.

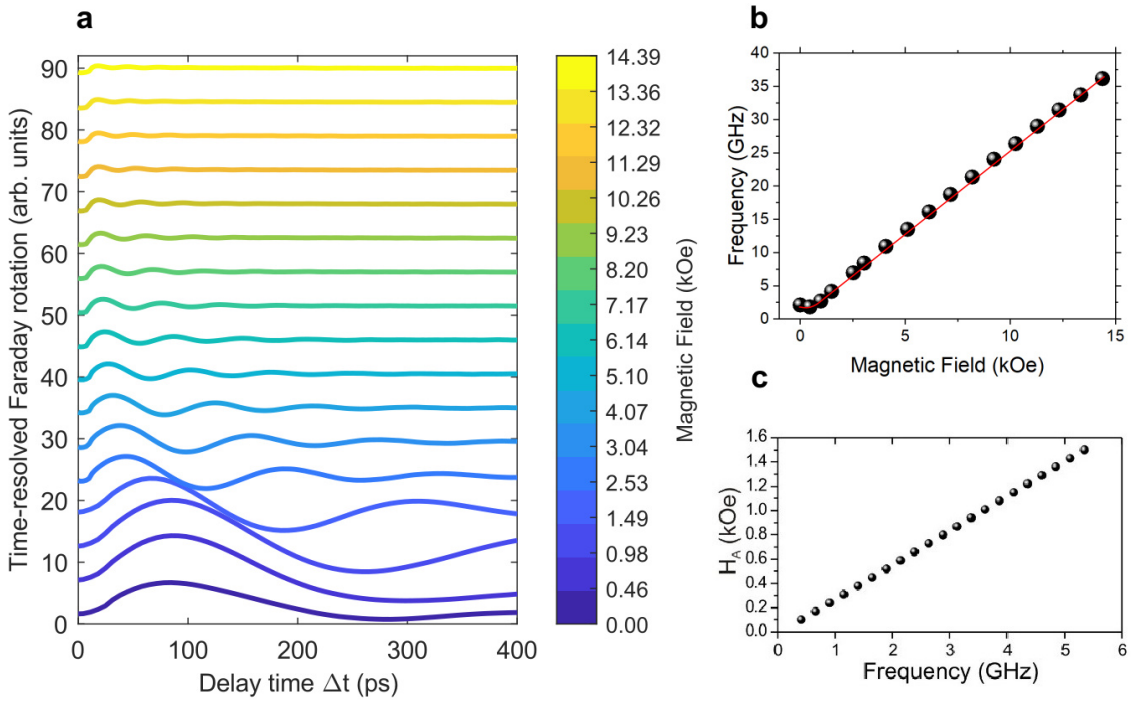

Figure 6.10: a) Magnetic field H dependence of magnetization precession for the non-miscut YIG:Co film. H was applied along the [100] direction in YIG:Co. b) Precession frequency deduced from the experimental data in (a) and c) The results of the calculation of effective anisotropy field H_A as a function of frequency f using the Kittel formula (equation 6.2) [153].

[154], assuming the considered YIG:Co case of a cubic crystal (001) with predominantly cubic anisotropy, Equation 6.1 can be simplified to the form:

$$f = \frac{\gamma}{2\pi}\sqrt{\left[H + (2H_A)\cos\phi\right]\left[H + 4\pi M_s + \frac{1}{4}(2H_A)(3 + \cos 4\phi)\right]} \tag{6.2}$$

where ϕ is the angle between the static field and the [100] crystal direction. Here, only the first-order magnetocrystalline anisotropy K_1 contributes to the energy W, and higher orders and other contributions to anisotropy are neglected and magnetic field will be zero.

The correlations in the temperature dependence of the switching time and the precession frequency show that the switching between the stable bit-states proceeds via magnetization precession. Obviously, the switching time between two magnetization states must be extracted from the precessional motion of magnetization during roughly $T/4$ which is similar τ obtained in time-resolved imaging.

The switching time is also comparable to the lifetime of the photo-induced magnetic anisotropy in the Co-substituted iron garnet, as shown in previous studies [48, 50]. The simulation results depict magnetization dynamics for pure cubic anisotropy K_C changes that correspond to the experimental temperature variations. Initially, simulation parameters were set to room temperature values, and although the anisotropy remained constant, the range of anisotropy data points was determined by aligning the precession frequencies with those observed in the experiment.

6.4 ENERGY OF HEAT DISSIPATION FOR MAGNETIZATION SWITCHING

Time-resolved experiments, while valuable for capturing dynamic behaviors and providing insights into temporal properties, do not inherently provide information on switching efficiency and energy of heat load during toggle switching in YIG:Co films. To determine switching efficiency, we conducted a comprehensive experiment that involved measuring the switched area in relation to the pump pulse fluence and the temperature of the YIG:Co sample. At each temperature point, we illuminated the sample with a series of single pump pulses, maintaining consistent focusing and fluence within the range of $1 - 90$ mJ/cm^2. The switched area was defined as an envelope covering the pattern of both labyrinth-like switched domain states, as explained in the procedure discussed in Figure 6.3b.

The obtained data are illustrated in Figure 6.11. We observe a decrease in the normalized switched area as the fluence is reduced. By extrapolating the experimental data to the x-axis, we can estimate the threshold fluence I_C required for switching, as shown in Figure 6.11a. Figure 6.11c provides a summary of the measurements in the form of a 3D plot. The horizontal axis represents the temperature-dependent effective field of magnetocrystalline anisotropy, while the vertical axis corresponds to the pump fluence. The color code indicates the normalized switched area, with dark colors denoting no switching, regions where only magnetization precession occurs, and light colors signifying the highest switching efficiency.

Figure 6.12 demonstrates a correlation between switching time and the dissipated energy during toggle switching in the volume of the garnet as $a_\lambda I_c/d$ (sample thickness is $d = 8$ µm). We estimate the volume density of heat dissipated during magnetization

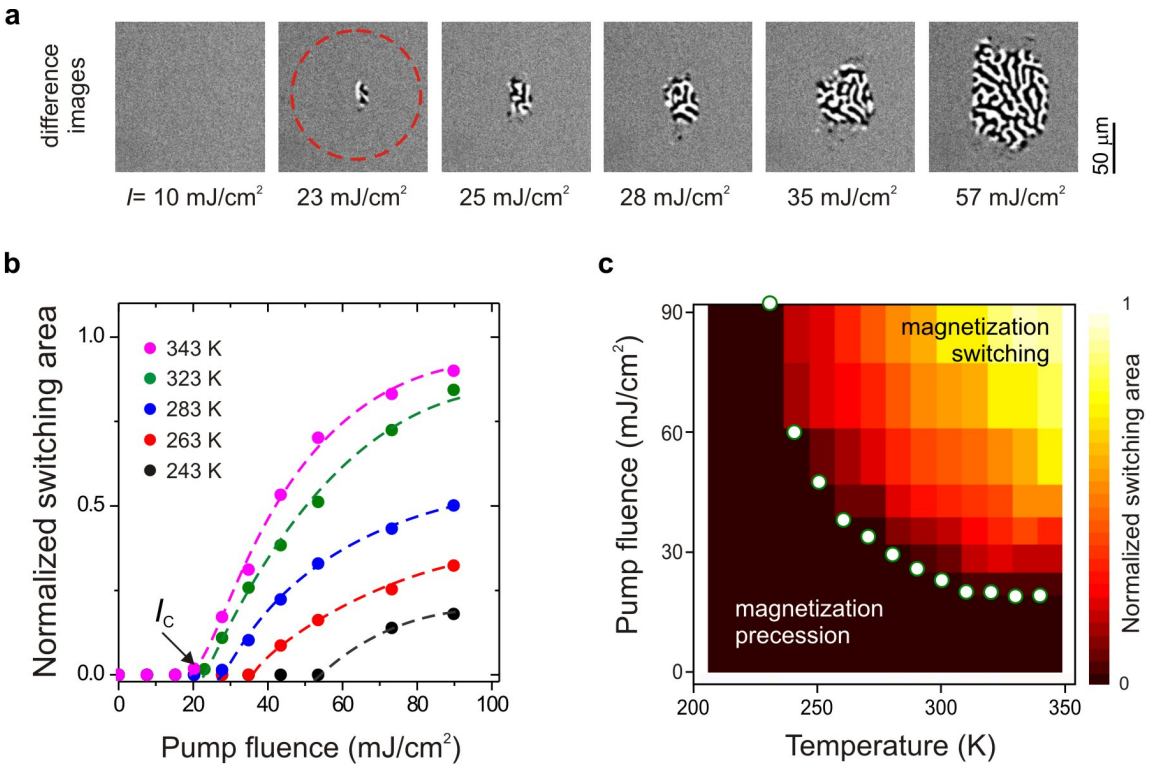

Figure 6.11: a) The exemplar switching spot size dependence over the pump fluence for room temperature. Dashed circle indicates the area exposed to the laser excitation. b) Normalized to the switching area pump fluence dependence over a broad range temperate representing switching efficiency. c) Energy diagram representing the switching efficiency of cold photo-magnetic recording. The color code indicates the normalized switched area, with dark colors indicating no switching, magnetization precession only region, and light colors indicating the highest switching efficiency. The white points highlight the switching of fluence thresholds I_C.

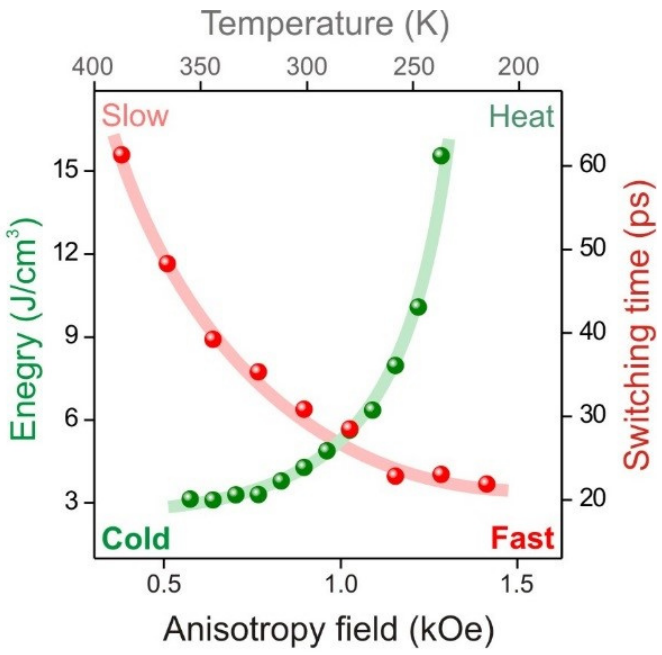

Figure 6.12: Green dots show the minimum heat load that accompanies the switching as a function of temperature and magnetic anisotropy field H_A. Red dots show the corresponding switching time as a function of temperature. Solid lines are guides for the eye.

toggle switching in YIG:Co as a fraction of the threshold fluence absorbed by the sample $a_\lambda I_c/d$ (sample thickness is $d = 8$ µm). The results clearly show that reducing the effective anisotropy field leads to a more than sixfold decrease in the energy threshold required for switching. However, this dependence on switching underscores a trade-off between speed and switching efficiency. While increasing the effective field of anisotropy can result in faster switching times, this advantage comes at the cost of a higher energy threshold.

By selecting the sample temperature, we can either expedite the switching process at the expense of higher dissipations or reduce the dissipation while sacrificing some of the speed. It is worth noting that the heat load during toggle switching, ranges from 15 J/cm^3 to 3 J/cm^3. This is significantly smaller compared to the heat load in heat-induced toggle switching (e.g., in 20 nm-thick GdFeCo metals, the fluence threshold switching was about 3 mJ/cm^3, which gives the heat load of about 1500 J/cm^3)[7].

The new mechanism of all-optical 'cold' toggle switching in YIG:Co, which does not rely on heat, offers a more efficient way to write magnetic bits with significantly lower heat loads compared to heat-induced toggle switching in metallic ferrimagnets. This mechanism can be realized over a broad temperature range, not limited to specific points like the compensation temperature in Rare Earth Transition Metal (RE-TM) ferrimagnetic alloys. Engineering the composition and symmetry of photo-magnetic garnets with strong spin-orbital coupling and temperature-induced phase-transitions opens up opportunities for designing all-optical toggle switching between various magnetic states. Specifically, the competition between cubic and uniaxial growth-induced anisotropy allows for creating materials with a spatial distribution of states featuring different energy thresholds, which can significantly reduce the switching energy. Keep in mind that in this mechanism, the switching time can be controlled by adjusting the intensity of the laser pulse, although it competes with the heat load as a crucial parameter.

7

CONCLUSION

Finding novel mechanisms and methods for coherent control of spin dynamics in the materials at ultrashort timescale, with minimal heat dissipation and the fastest possible speeds, presents a new challenge in the field of ultrafast magnetism. Thus the field has the potential to significantly impact future magnetic data storage technology. Beyond the primarily thermal mechanisms of all-optical magnetization switching in metals, there is a particular interest in nonthermal photo-magnetic excitation, driven by spin-orbit interactions that modify the spin energy landscape through optical radiation absorption. This thesis has taken a significant step towards a comprehensive understanding of the mechanisms and scenarios of ultrafast coherent photo-magnetic switching without relying on heat in Co-doped iron garnet films with different magnetic anisotropy and domain structures.

Firstly, substantial effort was invested in the development of experimental time-resolved three-color magneto-optical tools. A crucial achievement of this thesis is the design and construction of a system that allows for the simultaneous investigation of the temporal and spatial properties of ultrafast magnetization dynamics. This system was the first necessary step in deepening our understanding of all-optical magnetization switching mechanisms. For this purpose, a flexible measurement system based on a femtosecond laser was prepared at the Laboratory of Femtosecond Spectroscopy in the Faculty of Physics University of Bialystok, enabling the implementation of many research scenarios. The use of a unique single-shot pump and probe method allowed for increasing the magneto-optical Faraday rotation sensitivity up to 4 mdeg/µm with a temporal (<8 fs) and spatial (<400 nm) resolution, revealing previously unobserved behavior of laser-induced spin dynamics and switching.

Using this measurement system, previously unknown characteristics of monodomain and multi-domain photo-magnetic switching in YIG:Co thin films with a miscut angle were revealed. In the context of applied research, it was found that by adjusting laser fluence and beam focusing, it is possible to switch only a single bubble domain with a diameter of approximately 5 µm. This was made possible by recognizing that different domain types have varying energy thresholds for switching. The attempt to explain this observation became a driving factor for further research and led to a new hypothesis concerning the non-reciprocity of multi-state photo-magnetic switching in garnet films.

Consequently, an in-depth analysis of individual trajectories for all multi-state switching, both through experiments and LLG formalism-based modeling was done. It was demonstrated that magnetization switching with a single femtosecond laser pulse can occur along two different trajectory types, one faster and the other slower. The apparent non-reciprocity of the photo-magnetic switching routes is enabled by two main factors. Firstly, it is only possible when the switching is nonthermal precessional in nature, as op-

posed to the thermal accompanied by the magnetization quenching. Secondly, it requires an interplay of the photo-magnetic susceptibility tensor and magnetic energy landscape. In particular, changing the laser polarization orientation allows the selection of one of these types, opening the door to the potential of writing binary information within more than two states (e.g. logical combinations of 00, 01, 10, 11).

The most crucial result presented in this thesis is the revealing of a new 'cold' toggle photo-magnetic switching. For the first time, we have shown that it is possible to non-deterministically switch magnetization in miscut-free YIG:Co films without the need for polarization state control for writing and erasing in magnetic domains. Each successive laser pulse switches the magnetization, making the final state dependent only on the initial state and the number of laser pulses applied. Until now, ultrafast all-optical switching was demonstrated only in metals as a thermal-based effect. We would like to emphasize that such a toggle switching, in principle, contradicts thermodynamic Curie's principle, according to which symmetries of the causes are to be found in the symmetry of the effect. In our case, every excitation event is identical and thus the symmetry of the cause does not change. Nevertheless, we demonstrate that the symmetry of the toggle-switching effect alters from pulse to pulse.

As photo-magnetic switching is driven by the effective field of magnetic anisotropy, understanding the individual contributions is essential for understanding the effectiveness and scalability of the switching. We investigated the efficiency dependence on the fluence of laser-induced switching. Moreover, significant attention was given to exploring the switching possibilities at various temperatures, demonstrating a wide range from 200 K to 450 K where switching is feasible. This extensive scalability exceeds the capabilities of metallic ferromagnets with a local compensation point, which relies on temperature changes for switching. Moreover, the temperature range is impressive, even for electronic devices.

Additionally, we revealed experimentally and through simulations that temperature, which strongly influences magnetocrystalline anisotropy in garnets, affects the speed and efficiency of switching. Therefore, by changing the temperature, it is possible to reduce the switching energy threshold up to sixfold. We anticipate that using a train of identical laser pulses and employing the discovered switching mechanism with a characteristic time of about 20 ps one can toggle the magnetization of garnets at the frequency reaching 50 GHz. Such a high amplitude magnetization changes at so high frequency with the minimum heat load, leading to a remarkably small temperature increase of only about 0.6 K. However, there is a characteristic mutual balance that combines the threshold energy with the switching speed. Increasing the switching speed comes at the cost of reduced switching efficiency while reducing the switching speed opens up possibilities for even lower switching thresholds and dissipations.

Outlook

Scientific research often follows a pattern where new results lead to new questions, issues, and ideas. Therefore, the next steps include continued exploration of ideas and possibilities for scaling and controlling anisotropy in garnets. This can be achieved by producing new samples with altered compositions, with particular attention to the concentration of cobalt ions, a key factor in increasing light-induced magnetic anisotropy. In particular, the ability to adjust the competition between cubic and uniaxial growth-induced anisotropy

in photo-magnetic materials allows for changing the angle between magnetization states, which can also reduce the switching energy threshold.

Additionally, using an electric bias field as a factor to locally influence the material, supporting switching is an intriguing idea. Control of the intrinsic magnetic anisotropy and laser-induced and electrically induced anisotropies in a such way that the toggle photo-magnetic switching is only possible under simultaneous pulses of the electric field and light could be a unique solution for cold magnetic random access memory.

Furthermore, for verification of the fundamental Landauer limit (0.2 aJ/bit, assuming the bit size of 20x20x10 nm^3), reducing the size of bit recording and film thickness to nanometer sizes is essential. In such a case, utilizing magneto-plasmonic design to localization of the light field below the diffraction limit is one approach to achieve this goal.

BIBLIOGRAPHY

[1] H. J. Richter, A. Lyberatos, U. Nowak, R. F.L. Evans, and R. W. Chantrell. "The thermodynamic limits of magnetic recording." In: *Journal of Applied Physics* 111.3 (Feb. 2012), p. 033909. DOI: 10.1063/1.3681297 (cit. on p. 1).

[2] D. C. Ralph and M. D. Stiles. "Spin transfer torques." In: *Journal of Magnetism and Magnetic Materials* 320.7 (2008), pp. 1190–1216. DOI: 10.1016/j.jmmm.2007.12.019 (cit. on p. 1).

[3] Shuai Ning, Haoliang Liu, Jingxiong Wu, and Feng Luo. "Challenges and opportunities for spintronics based on spin orbit torque." In: *Fundamental Research* 2.4 (July 2022), pp. 535–538. DOI: 10.1016/j.fmre.2022.05.013 (cit. on p. 1).

[4] Yasuhiro Shirahata, Ryota Shiina, Diego López González, Kévin J.A. Franke, Eiji Wada, Mitsuru Itoh, Nikolay A. Pertsev, Sebastiaan Van Dijken, and Tomoyasu Taniyama. "Electric-field switching of perpendicularly magnetized multilayers." In: *NPG Asia Materials* 7.7 (2015), e198. DOI: 10.1038/am.2015.72 (cit. on p. 1).

[5] Jun Okabayashi, Yoshio Miura, and Tomoyasu Taniyama. "Strain-induced reversible manipulation of orbital magnetic moments in Ni/Cu multilayers on ferroelectric BaTiO 3." In: *npj Quantum Materials* 4.21 (2019). DOI: 10.1038/s41535-019-0159-y (cit. on p. 1).

[6] C. D. Stanciu, F. Hansteen, A. V. Kimel, A. Kirilyuk, A. Tsukamoto, A. Itoh, and Th Rasing. "All-optical magnetic recording with circularly polarized light." In: *Physical Review Letters* 99 (4 2007), p. 047601. DOI: 10.1103/PhysRevLett.99.047601 (cit. on pp. 2, 5, 10).

[7] T.A. Ostler et al. "Ultrafast heating as a sufficient stimulus for magnetization reversal in a ferrimagnet." In: *Nature Communications* 3.1 (Feb. 2012), p. 666. DOI: 10.1038/ncomms1666 (cit. on pp. 2, 5, 7, 10, 85, 86, 101).

[8] S. Mangin et al. "Engineered materials for all-optical helicity-dependent magnetic switching." In: *Nature Materials* 13.3 (2014), pp. 286–292. DOI: 10.1038/nmat3864 (cit. on pp. 2, 8).

[9] A. Stupakiewicz, K. Szerenos, D. Afanasiev, A. Kirilyuk, and A. V. Kimel. "Ultrafast nonthermal photo-magnetic recording in a transparent medium." In: *Nature* 542.7639 (2017), pp. 71–74. DOI: 10.1038/nature20807 (cit. on pp. 2, 8, 9, 19, 57, 58, 61, 65, 70–72, 75, 88, 93).

[10] Alexey V. Kimel and Mo Li. "Writing magnetic memory with ultrashort light pulses." In: *Nature Reviews Materials* 4.3 (Feb. 2019), pp. 189–200. DOI: 10.1038/s41578-019-0086-3 (cit. on p. 2).

[11] Andrei Kirilyuk, Alexey V. Kimel, and Theo Rasing. "Ultrafast optical manipulation of magnetic order." In: *Reviews of Modern Physics* 82.3 (Sept. 2010), pp. 2731–2784. DOI: 10.1103/RevModPhys.82.2731 (cit. on pp. 2, 33, 40).

[12] E. Beaurepaire, J. C. Merle, A. Daunois, and J. Y. Bigot. "Ultrafast spin dynamics in ferromagnetic nickel." In: *Physical Review Letters* 76.22 (1996), pp. 4250–4253. DOI: 10.1103/PhysRevLett.76.4250 (cit. on pp. 2, 5).

[13] Jean-Yves Bigot, Mircea Vomir, and Eric Beaurepaire. "Coherent ultrafast magnetism induced by femtosecond laser pulses." In: *Nature Physics* 5.7 (July 2009), pp. 515–520. DOI: 10.1038/nphys1285 (cit. on p. 3).

[14] B. Koopmans, G. Malinowski, F. Dalla Longa, D. Steiauf, M. Fähnle, T. Roth, M. Cinchetti, and M. Aeschlimann. "Explaining the paradoxical diversity of ultrafast laser-induced demagnetization." In: *Nature Materials* 9.3 (2010), pp. 259–265. DOI: 10.1038/nmat2593 (cit. on p. 3).

[15] Oksana Chubykalo-Fesenko and Pablo Nieves. "Landau-Lifshitz-Bloch Approach for Magnetization Dynamics Close to Phase Transition." In: *Handbook of Materials Modeling* (2020), pp. 867–893. DOI: 10.1007/978-3-319-44677-6_72 (cit. on p. 4).

[16] M. van Kampen, C. Jozsa, J. T. Kohlhepp, P. LeClair, L. Lagae, W. J. M. de Jonge, and B. Koopmans. "All-Optical Probe of Coherent Spin Waves." In: *Physical Review Letters* 88.22 (May 2002), p. 227201. DOI: 10.1103/PhysRevLett.88.227201 (cit. on p. 5).

[17] K. Vahaplar, A. M. Kalashnikova, A. V. Kimel, D. Hinzke, U. Nowak, R. Chantrell, A. Tsukamoto, A. Itoh, A. Kirilyuk, and Th Rasing. "Ultrafast Path for Optical Magnetization Reversal via a Strongly Nonequilibrium State." In: *Physical Review Letters* 103.11 (2009), pp. 66–69. DOI: 10.1103/PhysRevLett.103.117201 (cit. on pp. 5, 6, 86).

[18] K. Vahaplar et al. "All-optical magnetization reversal by circularly polarized laser pulses: Experiment and multiscale modeling." In: *Physical Review B - Condensed Matter and Materials Physics* 85.10 (Mar. 2012), p. 104402. DOI: 10.1103/PhysRevB.85.104402 (cit. on p. 5).

[19] I. Radu et al. "Transient ferromagnetic-like state mediating ultrafast reversal of antiferromagnetically coupled spins." In: *Nature* 472.7342 (2011), pp. 205–209. DOI: 10.1038/nature09901 (cit. on pp. 5, 7, 86).

[20] A. R. Khorsand, M. Savoini, A. Kirilyuk, A. V. Kimel, A. Tsukamoto, A. Itoh, and Th Rasing. "Role of magnetic circular dichroism in all-optical magnetic recording." In: *Physical Review Letters* 108.12 (2012), pp. 1–5. DOI: 10.1103/PhysRevLett.108.127205 (cit. on p. 5).

[21] C. S. Davies, J. H. Mentink, A. V. Kimel, Th Rasing, and A. Kirilyuk. "Helicity-independent all-optical switching of magnetization in ferrimagnetic alloys." In: *Journal of Magnetism and Magnetic Materials* 563.August 2022 (2022), p. 169851. DOI: 10.1016/j.jmmm.2022.169851 (cit. on p. 5).

[22] Na Wu, Shengjie Zhang, Yaxian Wang, and Sheng Meng. "Ultrafast all-optical quantum control of magnetization dynamics." In: *Progress in Surface Science* xxxx (2023), p. 100709. DOI: 10.1016/j.progsurf.2023.100709 (cit. on p. 5).

[23] Yong Xu and Stéphane Mangin. "Magnetization manipulation using ultra-short light pulses." In: *Journal of Magnetism and Magnetic Materials* 564.August (2022), p. 170169. DOI: 10.1016/j.jmmm.2022.170169 (cit. on p. 5).

[24] Amal El-Ghazaly, Brandon Tran, Alejandro Ceballos, Charles Henri Lambert, Akshay Pattabi, Sayeef Salahuddin, Frances Hellman, and Jeffrey Bokor. "Ultrafast magnetization switching in nanoscale magnetic dots." In: *Applied Physics Letters* 114.23 (2019), p. 232407. DOI: 10.1063/1.5098453 (cit. on p. 5).

[25] Alejandro Ceballos et al. "Role of element-specific damping in ultrafast, helicity-independent, all-optical switching dynamics in amorphous (Gd,Tb)Co thin films." In: *Physical Review B* 103.2 (2021), p. 24438. DOI: 10.1103/PhysRevB.103.024438 (cit. on p. 5).

[26] C. S. Davies, G. Bonfiglio, K. Rode, J. Besbas, C. Banerjee, P. Stamenov, J. M.D. Coey, A. V. Kimel, and A. Kirilyuk. "Exchange-driven all-optical magnetic switching in compensated 3d ferrimagnets." In: *Physical Review Research* 2.3 (Aug. 2020), p. 032044. DOI: 10.1103/PhysRevResearch.2.032044 (cit. on pp. 8, 86).

[27] C. Banerjee, N. Teichert, K. E. Siewierska, Z. Gercsi, G. Y. P. Atcheson, P. Stamenov, K. Rode, J. M. D. Coey, and J. Besbas. "Single pulse all-optical toggle switching of magnetization without gadolinium in the ferrimagnet Mn2RuxGa." In: *Nature Communications* 11.1 (Sept. 2020), p. 4444. DOI: 10.1038/s41467-020-18340-9 (cit. on pp. 8, 85, 86).

[28] M. L.M. Lalieu, M. J.G. Peeters, S. R.R. Haenen, R. Lavrijsen, and B. Koopmans. "Deterministic all-optical switching of synthetic ferrimagnets using single femtosecond laser pulses." In: *Physical Review B* 96.22 (2017), pp. 1–5. DOI: 10.1103/PhysRevB.96.220411 (cit. on p. 8).

[29] L. Avilés-Félix et al. "Single-shot all-optical switching of magnetization in Tb/Co multilayer-based electrodes." In: *Scientific Reports* 10.1 (Mar. 2020), p. 5211. DOI: 10.1038/s41598-020-62104-w (cit. on pp. 8, 85, 86).

[30] L. Avilés-Félix et al. "All-optical spin switching probability in [Tb/Co] multilayers." In: *Scientific Reports* 11.1 (Mar. 2021), p. 6576. DOI: 10.1038/s41598-021-86065-w (cit. on p. 8).

[31] K. Mishra et al. "Dynamics of all-optical single-shot switching of magnetization in Tb/Co multilayers." In: *Physical Review Research* 5.2 (June 2023), p. 023163. DOI: 10.1103/PhysRevResearch.5.023163 (cit. on p. 8).

[32] Sicong Wang et al. "Dual-shot dynamics and ultimate frequency of all-optical magnetic recording on GdFeCo." In: *Light: Science and Applications* 10.1 (2021), pp. 2047–7538. DOI: 10.1038/s41377-020-00451-z (cit. on pp. 8, 47).

[33] Felix Steinbach, Nele Stetzuhn, Dieter Engel, Unai Atxitia, Clemens Von Korff Schmising, and Stefan Eisebitt. "Accelerating double pulse all-optical write/erase cycles in metallic ferrimagnets." In: *Applied Physics Letters* 120.11 (2022), p. 112406. DOI: 10.1063/5.0080351 (cit. on p. 8).

[34] C-H. Lambert et al. "All-optical control of ferromagnetic thin films and nanostructures." In: *Science* 345.6202 (Sept. 2014), pp. 1337–1340. DOI: 10.1126/science.1253493 (cit. on p. 8).

[35] R. Medapalli, D. Afanasiev, D. K. Kim, Y. Quessab, S. Manna, S. A. Montoya, A. Kirilyuk, Th Rasing, A. V. Kimel, and E. E. Fullerton. "Multiscale dynamics of helicity-dependent all-optical magnetization reversal in ferromagnetic Co/Pt multilayers." In: *Physical Review B* 96 (22 2017), p. 224421. DOI: 10.1103/PhysRevB.96.224421 (cit. on p. 8).

[36] G. Kichin, M. Hehn, J. Gorchon, G. Malinowski, J. Hohlfeld, and S. Mangin. "From Multiple- to Single-Pulse All-Optical Helicity-Dependent Switching in Ferromagnetic Co/Pt Multilayers." In: *Physical Review Applied* 12 (2 2019), p. 024019. DOI: 10.1103/PhysRevApplied.12.024019 (cit. on p. 8).

[37] Jung-Wei Liao et al. "Controlling All-Optical Helicity-Dependent Switching in Engineered Rare-Earth Free Synthetic Ferrimagnets." In: *Advanced Science* 6.24 (Dec. 2019), p. 1901876. DOI: 10.1002/advs.201901876 (cit. on p. 8).

[38] Agne Ciuciulkaite et al. "Magnetic and all-optical switching properties of amorphous TbxCo100-x alloys." In: *Physical Review Materials* 4.10 (Oct. 2020), p. 104418. DOI: 10.1103/PhysRevMaterials.4.104418 (cit. on p. 8).

[39] M. S. El Hadri, P. Pirro, C. H. Lambert, S. Petit-Watelot, Y. Quessab, M. Hehn, F. Montaigne, G. Malinowski, and S. Mangin. "Two types of all-optical magnetization switching mechanisms using femtosecond laser pulses." In: *Physical Review B* 94 (6 2016), p. 064412. DOI: 10.1103/PhysRevB.94.064412 (cit. on p. 8).

[40] Feng Cheng et al. "All-Optical Helicity-Dependent Switching in Hybrid Metal–Ferromagnet Thin Films." In: *Advanced Optical Materials* 8.13 (2020), p. 2000379. DOI: 10.1002/adom.202000379 (cit. on p. 8).

[41] U. Parlak, R. Adam, D. E. Bürgler, S. Gang, and C. M. Schneider. "Optically induced magnetization reversal in [Co/Pt]N multilayers: Role of domain wall dynamics." In: *Physical Review B* 98 (21 2018), p. 214443. DOI: 10.1103/PhysRevB.98.214443 (cit. on p. 8).

[42] R. John et al. "Magnetisation switching of FePt nanoparticle recording medium by femtosecond laser pulses." In: *Scientific Reports* 7 (2017), p. 4114. DOI: 10.1038/s41598-017-04167-w (cit. on p. 8).

[43] Y. K. Takahashi, R. Medapalli, S. Kasai, J. Wang, K. Ishioka, S. H. Wee, O. Hellwig, K. Hono, and E. E. Fullerton. "Accumulative Magnetic Switching of Ultrahigh-Density Recording Media by Circularly Polarized Light." In: *Physical Review Applied* 6 (5 2016), p. 054004. DOI: 10.1103/PhysRevApplied.6.054004 (cit. on p. 8).

[44] Kihiro T. Yamada, Alexey V. Kimel, Kiran Horabail Prabhakara, Sergiu Ruta, Tian Li, Fuyuki Ando, Sergey Semin, Teruo Ono, Andrei Kirilyuk, and Theo Rasing. "Efficient All-Optical Helicity Dependent Switching of Spins in a Pt/Co/Pt Film by a Dual-Pulse Excitation." In: *Frontiers in Nanotechnology* 4.February (Feb. 2022). DOI: 10.3389/fnano.2022.765848 (cit. on p. 8).

[45] C. S. Davies, K. H. Prabhakara, M. D. Davydova, K. A. Zvezdin, T. B. Shapaeva, S. Wang, A. K. Zvezdin, A. Kirilyuk, Th Rasing, and A. V. Kimel. "Anomalously Damped Heat-Assisted Route for Precessional Magnetization Reversal in an Iron Garnet." In: *Physical Review Letters* 122.2 (Jan. 2019), p. 027202. DOI: 10.1103/PhysRevLett.122.027202 (cit. on p. 8).

[46] A. Stupakiewicz, A. Maziewski, I. Davidenko, and V. Zablotskii. "Light-induced magnetic anisotropy in Co-doped garnet films." In: *Physical Review B - Condensed Matter and Materials Physics* 64 (6 2001), p. 064405. DOI: 10.1103/PhysRevB.64.064405 (cit. on pp. 8, 16, 19).

[47] Andrei Kirilyuk, Alexey Kimel, Fredrik Hansteen, Theo Rasing, and Roman V. Pisarev. "Ultrafast all-optical control of the magnetization in magnetic dielectrics." In: *Low Temperature Physics* 32.8 (2006), pp. 748–767. DOI: 10.1063/1.2219497 (cit. on p. 8).

[48] F. Atoneche, A. M. Kalashnikova, A. V. Kimel, A. Stupakiewicz, A. Maziewski, A. Kirilyuk, and Th Rasing. "Large ultrafast photoinduced magnetic anisotropy in a cobalt-substituted yttrium iron garnet." In: *Physical Review B* 81.21 (June 2010), p. 214440. DOI: 10.1103/PhysRevB.81.214440 (cit. on pp. 8, 16, 19, 99).

[49] A. Frej, I. Razdolski, A. Maziewski, and A. Stupakiewicz. "Nonlinear subswitching regime of magnetization dynamics in photomagnetic garnets." In: *Physical Review B* 107.13 (Apr. 2023), p. 134405. DOI: 10.1103/PhysRevB.107.134405 (cit. on pp. 8, 18, 19, 21, 47, 58, 78, 96).

[50] A. Stupakiewicz, K. Szerenos, M. D. Davydova, K. A. Zvezdin, A. K. Zvezdin, A. Kirilyuk, and A. V. Kimel. "Selection rules for all-optical magnetic recording in iron garnet." In: *Nature Communications* 10.1 (Feb. 2019), p. 612. DOI: 10.1038/s41467-019-08458-w (cit. on pp. 9, 10, 15, 19, 62, 75, 78, 81, 99).

[51] Antoni Frej, Andrzej Maziewski, and Andrzej Stupakiewicz. "All-optical magnetic recording in garnets using a single laser pulse at L-band telecom wavelengths." In: *Applied Physics Letters* 118.26 (2021), p. 262401. DOI: 10.1063/5.0056522 (cit. on pp. 9, 19).

[52] A. Stupakiewicz, C. S. Davies, K. Szerenos, D. Afanasiev, K. S. Rabinovich, A. V. Boris, A. Caviglia, A. V. Kimel, and A. Kirilyuk. "Ultrafast phononic switching of magnetization." In: *Nature Physics* 17.4 (2021), pp. 489–492. DOI: 10.1038/s41567-020-01124-9 (cit. on pp. 9, 70).

[53] K. Szerenos, A. V. Kimel, A. Maziewski, A. Kirilyuk, and A. Stupakiewicz. "Fundamental Limits on the Repetition Rate of Photomagnetic Recording." In: *Physical Review Applied* 12 (4 2019), p. 044057. DOI: 10.1103/PhysRevApplied.12.044057 (cit. on pp. 10, 19, 47, 89–91).

[54] Félix Bertaut and Francis Forrat. "Sur les déformations dans les pérovskites à base de terres rares et d'éléments de transition trivalents." In: *Journal de Physique et le Radium* 17.2 (1956), pp. 129–131. DOI: 10.1051/jphysrad:01956001702012900 (cit. on p. 14).

[55] S. Geller and M. A. Gilleo. "Structure and ferrimagnetism of yttrium and rare-earth–iron garnets." In: *Acta Crystallographica* 10.3 (1957), pp. 239–239. DOI: 10.1107/s0365110x57000729 (cit. on p. 14).

[56] R. W. Damon and H. Van De Vaart. "Propagation of magnetostatic spin waves at microwave frequencies in a normally-magnetized disk." In: *Journal of Applied Physics* 36.11 (1965), pp. 3453–3459. DOI: 10.1063/1.1703018 (cit. on p. 14).

[57] S. L. Blank and J. W. Nielsen. "The growth of magnetic garnets by liquid phase epitaxy." In: *Journal of Crystal Growth* 17.C (1972), pp. 302–311. DOI: 10.1016/0022-0248(72)90261-8 (cit. on p. 14).

[58] P. C. Dorsey, S. E. Bushnell, R. G. Seed, and C. Vittoria. "Epitaxial yttrium iron garnet films grown by pulsed laser deposition." In: *Journal of Applied Physics* 74.2 (1993), pp. 1242–1246. DOI: 10.1063/1.354927 (cit. on p. 14).

[59] Christoph Hauser, Tim Richter, Nico Homonnay, Christian Eisenschmidt, Mohammad Qaid, Hakan Deniz, Dietrich Hesse, MacIej Sawicki, Stefan G. Ebbinghaus, and Georg Schmidt. "Yttrium Iron Garnet Thin Films with Very Low Damping Obtained by Recrystallization of Amorphous Material." In: *Scientific Reports* 6.December 2015 (2016), p. 20827. DOI: 10.1038/srep20827 (cit. on p. 14).

[60] M. C. Onbasli, A. Kehlberger, D. H. Kim, G. Jakob, M. Kläui, A. V. Chumak, B. Hillebrands, and C. A. Ross. "Pulsed laser deposition of epitaxial yttrium iron garnet films with low Gilbert damping and bulk-like magnetization." In: *APL Materials* 2 (Oct. 2014), p. 106102. DOI: 10.1063/1.4896936 (cit. on p. 14).

[61] Christian Holzmann and Manfred Albrecht. "Iron Garnet Thin Films for Applications in Magnonics and Spintronics." In: *Encyclopedia of Materials: Electronics*. Elsevier, 2023, pp. 777–795. DOI: 10.1016/B978-0-12-819728-8.00085-1 (cit. on pp. 14, 15).

[62] Konstantin P Belov and M A Zaitseva. "NEW MAGNETIC MATERIALS — GARNET FERRITES." In: *Soviet Physics Uspekhi* 1.1 (Jan. 1958), pp. 62–64. DOI: 10.1070/PU1958v001n01ABEH003082 (cit. on p. 14).

[63] S. Geller and M. A. Gilleo. "The crystal structure and ferrimagnetism of yttrium-iron garnet, Y3Fe2(FeO4)3." In: *Journal of Physics and Chemistry of Solids* 3.1-2 (1957), pp. 30–36. DOI: 10.1016/0022-3697(57)90044-6 (cit. on p. 14).

[64] James W. Nielsen. "Bubble Domain Memory Materials." In: *IEEE Transactions on Magnetics* 12.4 (1976), pp. 327–345. DOI: 10.1109/TMAG.1976.1059044 (cit. on pp. 14, 65).

[65] A. H. Bobeck, E. G. Spencer, L. G. Van Uitert, S. C. Abrahams, R. L. Barns, W. H. Grodkiewicz, R. C. Sherwood, P. H. Schmidt, D. H. Smith, and E. M. Walters. "Uniaxial magnetic garnets for domain wall "bubble" devices." In: *Applied Physics Letters* 17.3 (1970), pp. 131–134. DOI: 10.1063/1.1653335 (cit. on p. 14).

[66] Herbert Callen. "On growth-induced anisotropy in garnet crystals." In: *Materials Research Bulletin* 6.10 (Oct. 1971), pp. 931–938. DOI: 10.1016/0025-5408(71)90071-7 (cit. on p. 14).

[67] Stuart S. P. Parkin, Masamitsu Hayashi, and Luc Thomas. "Magnetic Domain-Wall Racetrack Memory." In: *Science* 320.5873 (Apr. 2008), pp. 190–194. DOI: 10.1126/science.1145799 (cit. on p. 14).

[68] Landolt-bornstein New Series, Magnetic Garnets, Thin Solid, Films Vol, and Fm-l Oe. *Part A: Garnets and Perovskites*. Ed. by K.-H. Hellwege and A. M. Hellwege. Vol. 12a. Landolt-Börnstein - Group III Condensed Matter. Berlin/Heidelberg: Springer-Verlag, 1978. DOI: 10.1007/b19986 (cit. on pp. 15, 17).

[69] Krzysztof Szerenos. "Ultrafast nonthermal photo-magnetic recording in dielectrics." PhD thesis. University of Bialystok, 2017 (cit. on pp. 16, 17, 19, 43).

[70] A. Maziewski, L. Pust, and P. Görnert. "Magnetometrical study of cobalt doped YIG garnet films." In: *Journal of Magnetism and Magnetic Materials* 83.1-3 (Jan. 1990), pp. 87–88. DOI: 10.1016/0304-8853(90)90441-R (cit. on pp. 16, 17).

[71] M. Tekielak. "Magnetyczna anizotropia i przejscia fazowe zwiazane z reorientacja namagnesowania w warstwach granatow domieszkowanych kobaltem." PhD thesis. University of Bialystok, 1997 (cit. on pp. 16, 17).

[72] M. D. Sturge, E. M. Gyorgy, R. C. Lecraw, and J. P. Remeika. "Magnetic behavior of cobalt in garnets. II. Magnetocrystalline anisotropy and ferrimagnetic resonance of cobalt-doped yttrium iron garnet." In: *Physical Review* 180.2 (1969), pp. 413–423. DOI: 10.1103/PhysRev.180.413 (cit. on pp. 16, 17).

[73] A. Stupakiewicz, M. Pashkevich, A. Maziewski, A. Stognij, and N. Novitskii. "Spin precession modulation in a magnetic bilayer." In: *Applied Physics Letters* 101.26 (Dec. 2012), p. 262406. DOI: 10.1063/1.4773508 (cit. on pp. 16, 21).

[74] J. Šimšová, I. Tomáš, P. Görnert, M. Nevřiva, and M. Maryško. "Preparation and properties of Co-substituted (001) YIG films with rectangular bubble domains." In: *Physica Status Solidi (a)* 53.1 (1979), pp. 297–301. DOI: 10.1002/pssa.2210530134 (cit. on p. 16).

[75] J. C. Slonczewski. "Origin of magnetic anisotropy in cobalt-substituted magnetite." In: *Physical Review* 110.6 (1958), pp. 1341–1348. DOI: 10.1103/PhysRev.110.1341 (cit. on p. 17).

[76] R. Jabłoński, A. Maziewski, M. Tekielak, and J. M. Desvignes. "FMR study of Co-substituted yttrium iron garnet films." In: *Journal of Magnetism and Magnetic Materials* 160.9 (July 1996), pp. 367–369. DOI: 10.1016/0304-8853(96)00229-6 (cit. on pp. 17, 96).

[77] Andrzej Maziewski. "Unexpected magnetization processes in YIG + Co films." In: *Journal of Magnetism and Magnetic Materials* 88.3 (Aug. 1990), pp. 325–342. DOI: 10.1016/0304-8853(90)90656-B (cit. on pp. 18, 21, 56, 70).

[78] M. Tekielak, A. Stupakiewicz, A. Maziewski, and J. M. Desvignes. "Temperature-induced phase transitions in Co-doped YIG films." In: *Journal of Magnetism and Magnetic Materials* 254-255 (2003), pp. 562–564. DOI: 10.1016/S0304-8853(02)00881-8 (cit. on pp. 18, 19).

[79] B. Antonini, M. Marinelli, E. Milani, A. Paoletti, P. Paroli, J. Daval, and B. Ferrand. "Site occupancy and valence state of optically active cobalt ions in yttrium iron garnet." In: *Physical Review B* 39.18 (June 1989), pp. 13442–13450. DOI: 10.1103/PhysRevB.39.13442 (cit. on p. 18).

[80] D. L. Wood and J. P. Remeika. "Optical absorption of tetrahedral Co3+ and Co2+ in garnets." In: *The Journal of Chemical Physics* 46.9 (May 1967), pp. 3595–3602. DOI: 10.1063/1.1841263 (cit. on p. 18).

[81] A. Chizhik, I. Davidenko, A. Maziewski, and A. Stupakiewicz. "High-temperature photomagnetism in Co-doped yttrium iron garnet films." In: *Physical Review B - Condensed Matter and Materials Physics* 57.22 (1998), pp. 14366–14369. DOI: 10.1103/PhysRevB.57.14366 (cit. on pp. 19, 57).

[82] Z. Simsa. "Optical and magnetooptical properties of Co-doped YIG films." In: *Czechoslovak Journal of Physics* 34.1 (Jan. 1984), pp. 78–87. DOI: 10.1007/BF01590483 (cit. on p. 20).

[83] Fredrik Hansteen, Alexey Kimel, Andrei Kirilyuk, and Theo Rasing. "Femtosecond photomagnetic switching of spins in ferrimagnetic garnet films." In: *Physical Review Letters* 95 (4 2005), p. 047402. DOI: 10.1103/PhysRevLett.95.047402 (cit. on p. 19).

[84] Fredrik Hansteen, Alexey Kimel, Andrei Kirilyuk, and Theo Rasing. "Nonthermal ultrafast optical control of the magnetization in garnet films." In: *Physical Review B - Condensed Matter and Materials Physics* 73 (1 2006), p. 014421. DOI: 10.1103/PhysRevB.73.014421 (cit. on p. 19).

[85] S. B. Roy. "Experimental Techniques in Magnetism." In: *Experimental Techniques in Magnetism and Magnetic Materials*. Cambridge University Press, Nov. 2022, pp. 89–92. DOI: 10.1017/9781108784948.009 (cit. on p. 26).

[86] Shingo Yamamoto and Iwao Matsuda. "Measurement of the Resonant Magneto-Optical Kerr Effect Using a Free Electron Laser." In: *Applied Sciences* 7.7 (June 2017), p. 662. DOI: 10.3390/app7070662 (cit. on p. 26).

[87] Michael Faraday. "I. Experimental researches in electricity.—Nineteenth series." In: *Philosophical Transactions of the Royal Society of London* 136 (1846), pp. 1–20. DOI: 10.1098/rstl.1846.0001 (cit. on p. 27).

[88] Masud Mansuripur. "The Faraday Effect." In: *Optics and Photonics News* 10.11 (Nov. 1999), p. 32. DOI: 10.1364/OPN.10.11.000032 (cit. on p. 27).

[89] Joachim Stohr and Hans Christoph Siegmann. *Magnetism*. 1st ed. Berlin, Heidelberg: Springer Berlin Heidelberg, 2006 (cit. on pp. 27, 96).

[90] A K Zvezdin and V A Kotov. "Modern Magnetooptics and Magnetooptical Materials." In: *Modern Magnetooptics and Magnetooptical Materials* (1997). DOI: 10.1887/075030362x (cit. on p. 29).

[91] T. Ishibashi, Z Kuang, Y Konishi, K Akahane, X.R. Zhao, T. Hasegawa, and K. Sato. "Novel Magneto-optical Microscope Using Optical Modulation Technique." In: *Transactions of the Magnetics Society of Japan* 4.4-2 (2004), pp. 278–281. DOI: 10.3379/tmjpn2001.4.278 (cit. on p. 31).

[92] F. Steinbach, D. Schick, C. von Korff Schmising, K. Yao, M. Borchert, W. D. Engel, and S. Eisebitt. "Wide-field magneto-optical microscope to access quantitative magnetization dynamics with femtosecond temporal and sub-micrometer spatial resolution." In: *Journal of Applied Physics* 130.8 (2021), p. 083905. DOI: 10.1063/5.0060091 (cit. on pp. 31, 32).

[93] Y. Hashimoto et al. "Ultrafast time-resolved magneto-optical imaging of all-optical switching in GdFeCo with femtosecond time-resolution and a μm spatial-resolution." In: *Review of Scientific Instruments* 85.6 (2014), p. 063702. DOI: 10.1063/1.4880015 (cit. on pp. 32, 48).

[94] NobelPrize.org. *The Nobel Prize in Chemistry 1999*. 1999. (Visited on 01/25/2023) (cit. on p. 33).

[95] NobelPrize.org. *The Nobel Prize in Physics 2018*. 2018. (Visited on 01/25/2023) (cit. on p. 33).

[96] T. H. Maiman. "Stimulated optical radiation in Ruby." In: *Nature* 187.4736 (Aug. 1960), pp. 493–494. DOI: 10.1038/187493a0 (cit. on p. 33).

[97] Franz X. Kärtner, Erich P. Ippen, and Steven T. Cundiff. "Femtosecond Laser Development." In: *Femtosecond Optical Frequency Comb: Principle, Operation, and Applications*. May 2014. Boston: Kluwer Academic Publishers, 2006, pp. 54–77. DOI: 10.1007/0-387-23791-7_2 (cit. on p. 33).

[98] Frank Träger, ed. *Springer Handbook of Lasers and Optics*. Springer Handbooks. Berlin, Heidelberg: Springer Berlin Heidelberg, 2012. DOI: 10.1007/978-3-642-19409-2 (cit. on pp. 34, 40).

[99] Jean Claude Diels and Wolfgang Rudolph. *Ultrashort Laser Pulse Phenomena: Fundamentals, Techniques, and Applications on a Femtosecond Time Scale, Second Edition*. Elsevier, 2006, pp. 1–652. DOI: 10.1016/B978-0-12-215493-5.X5000-9 (cit. on p. 36).

[100] Giulio Cerullo and Sandro De Silvestri. "Ultrafast optical parametric amplifiers." In: *Review of Scientific Instruments* 74.1 I (2003), pp. 1–18. DOI: 10.1063/1.1523642 (cit. on p. 38).

[101] Mark Csele. *Fundamentals of Light Sources and Lasers*. Wiley, July 2004, pp. 97–129. DOI: 10.1002/0471675210 (cit. on p. 38).

[102] Giulio Cerullo, Sandro De Silvestri, and Cristian Manzoni. "Optical parametric amplifiers." In: *Encyclopedia of Modern Optics* 1-5 (2018), pp. 290–301. DOI: 10.1016/B978-0-12-803581-8.09632-6 (cit. on p. 39).

[103] Claude Rullière, ed. *Femtosecond Laser Pulses*. Vol. 58. Advanced Texts in Physics. New York, NY: Springer New York, Nov. 2005, pp. 7250–7257. DOI: 10.1007/b137908 (cit. on p. 39).

[104] Ian A. Walmsley and Christophe Dorrer. "Characterization of ultrashort electromagnetic pulses." In: *Advances in Optics and Photonics* 1.2 (2009), p. 308. DOI: 10.1364/aop.1.000308 (cit. on p. 40).

[105] Jinyang Liang and Lihong V. Wang. "Single-shot ultrafast optical imaging." In: *Optica* 5.9 (2018), p. 1113. DOI: 10.1364/optica.5.001113 (cit. on pp. 41, 48).

[106] A. A. Berezhno. "Electro-optical modulators and shutters." In: *Journal of Optical Technology* 66.7 (1999), p. 583. DOI: 10.1364/jot.66.000583 (cit. on p. 41).

[107] W. J. Schwenger and J. M. Higbie. "High-speed acousto-optic shutter with no optical frequency shift." In: *Review of Scientific Instruments* 83.8 (Aug. 2012), p. 083110. DOI: 10.1063/1.4746292 (cit. on p. 41).

[108] Grace H. Zhang, Boris Braverman, Akio Kawasaki, and Vladan Vuletić. "Note: Fast compact laser shutter using a direct current motor and three-dimensional printing." In: *Review of Scientific Instruments* 86.12 (Dec. 2015), p. 126105. DOI: 10.1063/1.4937614 (cit. on p. 42).

[109] Dmytro Afanasiev. "Large-amplitude spin dynamics induced by femtosecond laser pulses in iron oxides." PhD thesis. Radboud University, 2015 (cit. on p. 43).

[110] F. Mertens, M. Terschanski, D. Mönkebüscher, S. Ponzoni, D. Bossini, and M. Cinchetti. "Wide spectral range ultrafast pump-probe magneto-optical spectrometer at low temperature, high-magnetic and electric fields." In: *Review of Scientific Instruments* 91.11 (2020), pp. 32–36. DOI: 10.1063/5.0024449 (cit. on p. 43).

[111] Y. Au, M. Dvornik, T. Davison, E. Ahmad, P. S. Keatley, A. Vansteenkiste, B. Van Waeyenberge, and V. V. Kruglyak. "Direct excitation of propagating spin waves by focused ultrashort optical pulses." In: *Physical Review Letters* 110 (9 2013), p. 097201. DOI: 10.1103/PhysRevLett.110.097201 (cit. on p. 48).

[112] Hironaru Murakami and Masayoshi Tonouchi. "High-sensitive scanning laser magneto-optical imaging system." In: *Review of Scientific Instruments* 81.1 (2010), p. 013701. DOI: 10.1063/1.3276710 (cit. on p. 48).

[113] Takuya Satoh, Yuki Terui, Rai Moriya, Boris A. Ivanov, Kazuya Ando, Eiji Saitoh, Tsutomu Shimura, and Kazuo Kuroda. "Directional control of spin-wave emission by spatially shaped light." In: *Nature Photonics* 6.10 (2012), pp. 662–666. DOI: 10.1038/nphoton.2012.218 (cit. on p. 48).

[114] M. C. Downer, R. L. Fork, and C. V. Shank. "Femtosecond imaging of melting and evaporation at a photoexcited silicon surface." In: *Journal of the Optical Society of America B* 2.4 (1985), p. 595. DOI: 10.1364/josab.2.000595 (cit. on p. 48).

[115] Dar'ya Davydova, Alejandro de la Cadena, Denis Akimov, and Benjamin Dietzek. "Transient absorption microscopy: Advances in chemical imaging of photoinduced dynamics." In: *Laser and Photonics Reviews* 10.1 (2016), pp. 62–81. DOI: 10.1002/lpor.201500181 (cit. on p. 48).

[116] Martin C. Fischer, Jesse W. Wilson, Francisco E. Robles, and Warren S. Warren. "Invited Review Article: Pump-probe microscopy." In: *Review of Scientific Instruments* 87.3 (2016), p. 031101. DOI: 10.1063/1.4943211 (cit. on p. 48).

[117] Tomosato Hioki, Yusuke Hashimoto, Tom H. Johansen, and Eiji Saitoh. "Time-Resolved Imaging of Magnetoelastic Waves by the Cotton-Mouton Effect." In: *Physical Review Applied* 11.6 (2019), p. 061007. DOI: 10.1103/PhysRevApplied.11.061007 (cit. on p. 48).

[118] Peter M. Celliers, Kent G. Estabrook, Russell J. Wallace, James E. Murray, Luiz B. Da Silva, Brian J. MacGowan, Bruno M. Van Wonterghem, and Kenneth R. Manes. "Spatial filter pinhole for high-energy pulsed lasers." In: *Applied Optics* 37.12 (1998), p. 2371. DOI: 10.1364/ao.37.002371 (cit. on p. 51).

[119] Martin Čapek, Jiří Janáček, and Lucie Kubínová. "Methods for compensation of the light attenuation with depth of images captured by a confocal microscope." In: *Microscopy Research and Technique* 69.8 (2006), pp. 624–635. DOI: 10.1002/jemt.20330 (cit. on p. 53).

[120] M. Kisielewski, A. Maziewski, and P. Gornert. "Magnetic after-effect influence on domain-wall dynamics in Co-containing garnet films." In: *Journal of Physics D: Applied Physics* 20.2 (1987), pp. 222–225. DOI: 10.1088/0022-3727/20/2/012 (cit. on p. 62).

[121] M. Kisielewski, A. Maziewski, and J. M. Desvignes. "Domain structure shape memory in a magnet with magnetization induced anisotropy." In: *Journal of Magnetism and Magnetic Materials* 140-144.PART 3 (1995), pp. 1923–1924. DOI: 10.1016/0304-8853(94)01376-4 (cit. on p. 62).

[122] A. H. Bobeck. "Properties and Device Applications of Magnetic Domains in Orthoferrites." In: *Bell System Technical Journal* 46.8 (Oct. 1967), pp. 1901–1925. DOI: 10.1002/j.1538-7305.1967.tb03177.x (cit. on p. 65).

[123] Edward A. Giess. "Magnetic bubble materials." In: *Science* 208.4446 (1980), pp. 938–943. DOI: 10.1126/science.208.4446.938 (cit. on p. 65).

[124] A. P. Malozemoff and J. C. Slonczewski. *Magnetic Domain Walls in Bubble Materials*. Academic Press, New York, 1979. DOI: 10.1016/c2013-0-06998-8 (cit. on p. 65).

[125] A. Ashkin and J. M. Dziedzic. "Interaction of laser light with magnetic domains." In: *Applied Physics Letters* 21.6 (1972), pp. 253–255. DOI: 10.1063/1.1654366 (cit. on p. 65).

[126] Xichao Zhang, Yan Zhou, Kyung Mee Song, Tae-Eon Park, Jing Xia, Motohiko Ezawa, Xiaoxi Liu, Weisheng Zhao, Guoping Zhao, and Seonghoon Woo. "Skyrmion-electronics: writing, deleting, reading and processing magnetic skyrmions toward spintronic applications." In: *Journal of Physics: Condensed Matter* 32.14 (Apr. 2020), p. 143001. DOI: 10.1088/1361-648X/ab5488 (cit. on p. 65).

[127] Nina Novakovic-Marinkovic, Mohamad Assaad Mawass, Oleksii Volkov, Pavlo Makushko, W. Dieter Engel, Denys Makarov, and Florian Kronast. "From stripes to bubbles: Deterministic transformation of magnetic domain patterns in Co/Pt multilayers induced by laser helicity." In: *Physical Review B* 102.17 (2020), p. 174412. DOI: 10.1103/PhysRevB.102.174412 (cit. on p. 65).

[128] Naoki Ogawa, Wataru Koshibae, Aron Jonathan Beekman, Naoto Nagaosa, Masashi Kubota, Masashi Kawasaki, and Yoshinori Tokura. "Photodrive of magnetic bubbles via magnetoelastic waves." In: *Proceedings of the National Academy of Sciences of the United States of America* 112.29 (2015), pp. 8977–8981. DOI: 10.1073/pnas.1504064112 (cit. on p. 65).

[129] Qi Zhang, Lin Xie, Guangqing Liu, Sergei Prokhorenko, Yousra Nahas, Xiaoqing Pan, Laurent Bellaiche, Alexei Gruverman, and Nagarajan Valanoor. "Nanoscale Bubble Domains and Topological Transitions in Ultrathin Ferroelectric Films." In: *Advanced Materials* 29 (2017), p. 1702375. DOI: 10.1002/adma.201702375 (cit. on p. 65).

[130] Jie Yin et al. "Nanoscale bubble domains with polar topologies in bulk ferroelectrics." In: *Nature Communications* 12 (2021), p. 3632. DOI: 10.1038/s41467-021-23863-w (cit. on p. 65).

[131] Wanjun Jiang et al. "Blowing magnetic skyrmion bubbles." In: *Science* 349.6245 (2015), pp. 283–286. DOI: 10.1126/science.aaa1442 (cit. on p. 65).

[132] Kyoung Woong Moon, Seungmo Yang, Tae Seong Ju, Changsoo Kim, Byoung Sun Chun, Sungkyun Park, and Chanyong Hwang. "Universal method for magnetic skyrmion bubble generation by controlling the stripe domain instability." In: *NPG Asia Materials* 13.20 (2021). DOI: 10.1038/s41427-021-00290-3 (cit. on p. 65).

[133] K. S. Antipin, T. T. Gareev, N. V. Myasnikov, E. P. Nikolaeva, and A. P. Pyatakov. "Bipolar electric field-induced nucleation of magnetic domains with 90° domain walls." In: *Journal of Applied Physics* 129.2 (Jan. 2021), p. 024103. DOI: 10.1063/5.0029652 (cit. on p. 65).

[134] Arne Brataas, Andrew D. Kent, and Hideo Ohno. "Current-induced torques in magnetic materials." In: *Nature Materials* 11.5 (2012), pp. 372–381. DOI: 10.1038/nmat3311 (cit. on p. 70).

[135] Sasikanth Manipatruni, Dmitri E. Nikonov, Chia Ching Lin, Tanay A. Gosavi, Huichu Liu, Bhagwati Prasad, Yen Lin Huang, Everton Bonturim, Ramamoorthy Ramesh, and Ian A. Young. "Scalable energy-efficient magnetoelectric spin–orbit logic." In: *Nature* 565.7737 (2019), pp. 35–42. DOI: 10.1038/s41586-018-0770-2 (cit. on p. 70).

[136] Xuepeng Qiu, William Legrand, Pan He, Yang Wu, Jiawei Yu, Rajagopalan Ramaswamy, Aurelien Manchon, and Hyunsoo Yang. "Enhanced Spin-Orbit Torque via Modulation of Spin Current Absorption." In: *Physical Review Letters* 117.21 (Nov. 2016), p. 217206. DOI: 10.1103/PhysRevLett.117.217206 (cit. on p. 70).

[137] Cheng Song, Ruiqi Zhang, Liyang Liao, Yongjian Zhou, Xiaofeng Zhou, Ruyi Chen, Yunfeng You, Xianzhe Chen, and Feng Pan. "Spin-orbit torques: Materials, mechanisms, performances, and potential applications." In: *Progress in Materials Science* 118.October 2020 (May 2021), p. 100761. DOI: 10.1016/j.pmatsci.2020.100761 (cit. on p. 70).

[138] Ji Wan Kim, Mircea Vomir, and Jean Yves Bigot. "Controlling the spins angular momentum in ferromagnets with sequences of picosecond acoustic pulses." In: *Scientific Reports* 5 (2014), p. 8511. DOI: 10.1038/srep08511 (cit. on p. 70).

[139] Oleksandr Kovalenko, Thomas Pezeril, and Vasily V. Temnov. "New concept for magnetization switching by ultrafast acoustic pulses." In: *Physical Review Letters* 110 (26 2013), p. 266602. DOI: 10.1103/PhysRevLett.110.266602 (cit. on p. 70).

[140] A. V. Scherbakov, A. S. Salasyuk, A. V. Akimov, X. Liu, M. Bombeck, C. Brüggemann, D. R. Yakovlev, V. F. Sapega, J. K. Furdyna, and M. Bayer. "Coherent magnetization precession in ferromagnetic (Ga,Mn)As induced by picosecond acoustic pulses." In: *Physical Review Letters* 105 (11 2010), p. 117204. DOI: 10.1103/PhysRevLett.105.117204 (cit. on p. 70).

[141] Vladimir S. Vlasov, Alexey M. Lomonosov, Anton V. Golov, Leonid N. Kotov, Valentin Besse, Alexandr Alekhin, Dmitry A. Kuzmin, Igor V. Bychkov, and Vasily V. Temnov. "Magnetization switching in bistable nanomagnets by picosecond pulses of surface acoustic waves." In: *Physical Review B* 101.2 (2020), p. 24425. DOI: 10.1103/PhysRevB.101.024425 (cit. on p. 70).

[142] Wei Gang Yang and Holger Schmidt. "Acoustic control of magnetism toward energy-efficient applications." In: *Applied Physics Reviews* 8.2 (2021), p. 021304. DOI: 10.1063/5.0042138 (cit. on p. 70).

[143] D. Afanasiev, I. Razdolski, K. M. Skibinsky, D. Bolotin, S. V. Yagupov, M. B. Strugatsky, A. Kirilyuk, Th Rasing, and A. V. Kimel. "Laser excitation of lattice-driven anharmonic magnetization dynamics in dielectric FeBO3." In: *Physical Review Letters* 112 (14 2014), p. 147403. DOI: 10.1103/PhysRevLett.112.147403 (cit. on p. 70).

[144] D. Afanasiev, J. R. Hortensius, B. A. Ivanov, A. Sasani, E. Bousquet, Y. M. Blanter, R. V. Mikhaylovskiy, A. V. Kimel, and A. D. Caviglia. "Ultrafast control of magnetic interactions via light-driven phonons." In: *Nature Materials* 20.5 (2021), pp. 607–611. DOI: 10.1038/s41563-021-00922-7 (cit. on p. 70).

[145] Uwe Bovensiepen. "Coherent and incoherent excitations of the Gd(0001) surface on ultrafast timescales." In: *Journal of Physics Condensed Matter* 19.8 (2007), p. 083201. DOI: 10.1088/0953-8984/19/8/083201 (cit. on p. 70).

[146] Ankit S. Disa, Michael Fechner, Tobia F. Nova, Biaolong Liu, Michael Först, Dharmalingam Prabhakaran, Paolo G. Radaelli, and Andrea Cavalleri. "Polarizing an antiferromagnet by optical engineering of the crystal field." In: *Nature Physics* 16.9 (2020), pp. 937–941. DOI: 10.1038/s41567-020-0936-3 (cit. on p. 70).

[147] Sebastian F. Maehrlein et al. "Dissecting spin-phonon equilibration in ferrimagnetic insulators by ultrafast lattice excitation." In: *Science Advances* 4.7 (July 2018), eaar5164. DOI: 10.1126/sciadv.aar5164 (cit. on p. 70).

[148] P. Curie. "Sur la symetrie dans les phenomenes physiques. Symetrie d'un champ electrique et d'un champ magnetique." In: *Journal de Physique* 3 (1894), pp. 393–415 (cit. on pp. 85, 86).

[149] Giacomo Sala et al. "Asynchronous current-induced switching of rare-earth and transition-metal sublattices in ferrimagnetic alloys." In: *Nature Materials* 21.6 (June 2022), pp. 640–646. DOI: 10.1038/s41563-022-01248-8 (cit. on p. 86).

[150] J. Becker, A. Tsukamoto, A. Kirilyuk, J. C. Maan, Th Rasing, P. C. M. Christianen, and A. V. Kimel. "Ultrafast Magnetism of a Ferrimagnet across the Spin-Flop Transition in High Magnetic Fields." In: *Physical Review Letters* 118.11 (Mar. 2017), p. 117203. DOI: 10.1103/PhysRevLett.118.117203 (cit. on p. 86).

[151] A. J. Schellekens and B. Koopmans. "Microscopic model for ultrafast magnetization dynamics of multisublattice magnets." In: *Physical Review B* 87.2 (Jan. 2013), p. 020407. DOI: 10.1103/PhysRevB.87.020407 (cit. on p. 86).

[152] R. R. Birss. *Symmetry and Magnetism*. New York: John Wiley and Sons, Inc., 1966 (cit. on pp. 86, 88).

[153] Charles Kittel. "On the Theory of Ferromagnetic Resonance Absorption." In: *Physical Review* 73.2 (Jan. 1948), pp. 155–161. DOI: 10.1103/PhysRev.73.155 (cit. on pp. 96, 98).

[154] Osamu Kohmoto. "Effective demagnetizing factors in ferromagnetic resonance equations." In: *Journal of Magnetism and Magnetic Materials* 262.2 (June 2003), pp. 280–288. DOI: 10.1016/S0304-8853(02)01504-4 (cit. on p. 99).

LIST OF PUBLICATIONS

PUBLICATIONS

1. T. Zalewski, A. Maziewski, A. Stupakiewicz, "Time-resolved photo-magnetic switching of bubble domains in ferrimagnetic garnets", *Appl. Phys. Lett.* 123, 032402 (2023). *Editor's pick.*

2. T. Zalewski and A. Stupakiewicz, "Single-shot imaging of ultrafast all-optical magnetization dynamics with a spatiotemporal resolution", *Rev Sci Instrum* 92, 103004 (2021).

3. T. Zalewski, V. Ozerov, A. Maziewski, I. Razdolski, A. Stupakiewicz, "Non-reciprocal coherent all-optical switching between magnetic multi-states", *arXiv:*2308.12771 (2023), under review in *Phys. Rev. Lett.*

4. T. Zalewski, L. Nowak, A. Stupakiewicz, "Coherent control of photo-magnetic back-switching by double-pump laser pulses, *arXiv:*2311 (2023), under review in *Phys. Rev. Appl.*

5. T. Zalewski, A. Maziewski, A.V. Kimel, A. Stupakiewicz, "Ultrafast all-optical toggle writing of magnetic bits without relying on heat", *arXiv:*2311.10173 (2023) submitted in *Nature Comm*.

CONFERENCE PRESENTATIONS

1. T. Zalewski, A. Frej, A. Stupakiewicz, "Single-shot ultrafast imaging of photo-magnetic switching in YIG:Co film", 4th Ultrafast Magnetism Conference 2019, York (UK), 14-17.10.2019.

2. A. Frej, T. Zalewski, and A. Stupakiewicz, "All-optical magnetic recording in YIG:Co using a single laser pulse at telecom wavelengths", Ultrafast Magnetism Conference 2019, York.

3. T. Zalewski, A. Stupakiewicz, "Ultrafast photo-magnetic back-switching in garnet films", Joint European Magnetic Symposia (JEMS) 2020, Lisbon (Portugal), 7-11.12.2020, (online) oral.

4. A. Frej, T. Zalewski, A. Stupakiewicz, "Photo-magnetic recording with L-band ultrashort laser pulses in dielectric medium", 11th International Conference on Metamaterials, Photonic Crystals and Plasmonics (META) 2021, Warsaw, (Poland), 20-23.07 2021.

5. T. Zalewski, A. Stupakiewicz, “Single-shot time-resolved imaging of all-optical ultrafast photo-magnetic switching”, 11th International Conference on Metamaterials, Photonic Crystals and Plasmonics (META) 2021, Warsaw, (Poland), 20-23.07 2021, (online) oral.

6. T. Zalewski, A. Stupakiewicz, “Single-shot time-resolved imaging of all-optical ultrafast photo-magnetic switching”, Sympozjum Młodych Naukowców 2021 pod patronatem Wydziału Fizyki Uniwersytetu Warszawskiego, Warsaw, (Poland), 30.08-03.09 2021, (online) oral.

7. T. Zalewski, A. Frej, A. Stupakiewicz, “Temporal, spatial, and spectral character of all- optical photo-magnetic switching in YIG:Co film”, 3rd Summer School “Ultrafast magneto-electrics”, Samobor (Croatia), 30.08-03.09 2021, (online) oral.

8. T. Zalewski, A. Stupakiewicz, “Development of the automatized setup for the single-shot time-resolved imaging of all-optical ultrafast photo-magnetic switching”, 2022 Joint MMM-INTERMAG, New Orlean, (USA), 10-14.01 2022, oral.

9. T. Zalewski, A. Frej, A. Stupakiewicz, “Nonthermal ultrafast photo-induced dynamics of non-collinear multi-states switching of magnetization in garnets”, 4th International Advanced School on Magnonics MAGNETOFON”, Porto (Portugal), 18-22.07.2023.

10. T. Zalewski, A. Stupakiewicz, “Control of switching time and Energy dissipation for ultrafast photo-magnetic recording in dielectrics”, Joint European Magnetic Symposia (JEMS) 2022, Warsaw, (Poland), 24-29.07 2022, oral.

11. T. Zalewski, A. Stupakiewicz, “All-optical switching of magnetization in dielectrics”, Workshop COST Action CA17123 MAGNETOFON, Istambul (Turkey), 6-7.10, 2022, oral.

12. T. Zalewski, A. Stupakiewicz, “Multi-domain states switching dynamics in YIG:Co films”, Workshop COST Action CA17123 MAGNETOFON, Egmond aan Zee (The Netherlands), 6-9.03.2023, oral.

13. L. Nowak, T. Zalewski, A. Stupakiewicz, “Coherent Control of Photo-Magnetic Precession and Switching by Double-Shot Laser Pulses”, Joint European Magnetic Symposia (JEMS) 2023, Madrid (Spain), 27.08-01.09.23.

14. T. Zalewski, A. Frej, A. Stupakiewicz, “Ultrafast photo-induced dynamics of multi states switching of magnetization in garnet” Joint European Magnetic Symposia (JEMS) 2023, Madrid (Spain), 27.08-01.09.23, oral.